NON-PERTURBATIVE FIELD THEORIES

David Stephenson

Submitted for the degree of
Doctor of Philosophy

Department of Physics
University of Edinburgh
August 1988

Abstract

Some non-perturbative aspects of field theories are studied by applying lattice gauge theory techniques.

The low-lying hadronic mass spectrum is calculated numerically using quenched lattice quantum chromodynamics. The results of large numerical simulations performed on a distributed array processor are presented and analysed. Particular emphasis is stressed upon the understanding of systematic and statistical errors in the calculation. In addition, the pion decay constant and the chiral condensate are evaluated. An attempt is made to relate the numerical findings to the experimentally measured quantities.

A pioneering attempt to understand Yukawa couplings is discussed. A toy Fermion-Higgs system is studied numerically on a transputer array. Dynamical fermions are included in the investigation of the behaviour of the system over a wide range of Yukawa couplings. A phase diagram is found for the model which shows evidence of spontaneous chiral symmetry breaking transitions. Extensions of the model are discussed together with some speculations concerning the behaviour of Yukawa couplings in general.

The possibility of using the lattice as a model for space-time is investigated by studying the propagation of particles on a fractal lattice. In addition, the use of truncated fractals as novel regulators is studied numerically in the hope that the problem of fermion doubling will be alleviated.

Acknowledgements

Above all, I am indebted to my parents for their loving support and encouragement. I would also like to offer my gratitude to the many good friends who have made my stay in Edinburgh so enjoyable. Although so many are now so far away, I wish such close companions all the very best for their futures. Finally I would like to say that this work would not have been possible without the support of the many kind people who work in the James Clerk Maxwell building. In particular, I am grateful to Richard Kenway for his useful comments on this thesis and to Tien Kieu for helping me with LaTeX. To all these people, I dedicate this thesis.

"On an Etruscan vase in the Louvre figures of children are seen blowing bubbles. These children probably enjoyed their occupation just as modern children do. Our admiration of the beautiful and delicate forms, growing and developing themselves, the feeling that it is our breath which is turning dirty soap-suds into spheres of spleandour, the fear least by ireverent touch we may cause the gorgeous vision to vanish with a sputter of soapy water in our eyes, our wistful gaze as we watch the perfect bubble when it sails away from the pipe's mouth to join, somewhere in the sky, all the other beautiful things that have vanished before it, assures us that, whatever our nominal age may be we are of the same family as those Etruscan children ..."

James Clerk Maxwell (1874)

Contents

1 Threads in a Tapestry **6**

1.1 History of Unification 7

1.2 The Standard Model 9

1.2.1 Particle Content 9

1.2.2 Pure Gauge Sector 10

1.2.3 Matter fields 10

1.2.4 Mass generation 10

1.2.5 Questions 11

1.3 Lattice Gauge Theory 12

1.3.1 Introduction 12

1.3.2 The Method 12

1.3.3 Gauge fields 15

1.3.4 Monte-Carlo Simulations 16

1.3.5 Fermions 17

1.4 Thesis Morphology 18

2 Lattice QCD **19**

2.1 Introduction 20

2.1.1 Action 20

2.1.2 Global Continuous Symmetries 22

2.1.3 Scaling and FSE 23

2.2 Methodology 25

2.2.1 Overview 25

2.2.2 Gauge Configurations 27

2.2.3 Quark Propagators 27

2.2.4 Hadron Propagators 30

2.3 Results 34

2.3.1 Summary 34

2.3.2 Pion 35

2.3.3 Rho meson 37

2.3.4 Nucleon 37

2.3.5 Mass Ratios 41

2.3.6 Pion Decay Constant 43

2.4 Physical Limit 45

2.4.1 Flavour Symmetry Restoration 45

2.4.2 Asymptotic Scaling 48

2.4.3 Avoiding FSE 49

2.5 Conclusions 50

3 Yukawa Interactions. 53

3.1 Motivation 55

3.1.1 Effective Potential 55

3.1.2 Triviality 56

3.1.3 Fermion Doubling 58

3.2 Toy Model 60

3.2.1 Action 60

3.2.2 Symmetries 61

3.2.3 Observables 62

3.3 Method 62

3.3.1 Algorithm 63

3.3.2 Implementation 64

3.3.3 Checks 65

3.4 Results 66

3.5 Conclusions 72

3.6 Speculations 76

3.6.1 Complex Determinant 76

3.6.2 Singular fermions 77

3.6.3 A New Mexican Hat 78

4 Finer Threads. **81**

4.1 Discrete Language. 83

4.1.1 Cell-complex 83

4.1.2 Incidence functions 84

4.1.3 Cochains 85

4.1.4 Transcription 85

4.2 Scalar Propagation 87

4.2.1 Klein-Gordon equation 87

4.2.2 Decimation 89

4.2.3 Exact RG 90

4.2.4 Propagator 91

4.2.5 Conclusions 94

4.3 Fermion Propagation 94

4.3.1 DK fermions 95

4.3.2 Motivation 96

4.3.3 Weaving Carpets 97

4.3.4 Propagators 103

4.3.5 Doubling 105

4.3.6 Conclusions 106

A Notation. **110**

A.1 Indices 110

A.2 Lattice Derivatives 110

A.3 Gamma Matrices 110

A.4 Miscellaneous 111

B Array Processors. **112**

B.1 Distributed Array Processor. 112

B.2 Transputer Array. 113

C Fermion Determinant. **115**

C.1 Definitions. 115

C.2 Large Y 116

C.3 Small Y 116

Chapter 1

Threads in a Tapestry

The theory we now have is an integral work of art:
the patchwork quilt has become a tapestry.
S.L. Glashow 1979

The tapestry is the *Standard model* of strong, weak and electromagnetic interactions. It sucessfully decribes particle interactions down to distances as small as 10^{-18} metres and represents a remarkable synthesis of ideas over many years. Although it is not the ultimate unified theory, it provides a basis for further development. Many aspects of the Standard model are not well understood beyond perturbation expansions in powers of small couplings. The work in chapters 2 and 3 of this thesis, use the non-perturbative techniques of lattice gauge theory to look at some of these aspects. The work in chapter 4 goes beyond the Standard model in search of finer threads in the tapestry.

In this introduction, I will first present a condensed history of the ideas that have led to the Standard model. I will then describe the minimal Standard model and mention some of the questions that it raises. Following this, there will be a description of the techniques used in lattice gauge theory. And finally, the structure of the thesis will be outlined.

1.1 History of Unification

The Standard model was woven over many years by many theorists and was completed in 1973. In this section, I will attempt to present a historical review of the major concepts that led to the Standard model. For explicit references to the mentioned work refer to [1,2,3].

In 1864, James Clerk Maxwell unified the first threads in the tapestry [4]. In writing down the classical field equations describing electric and magnetic fields, he succeeded in unifying the two forces and produced the first gauge field theory. Next, there came the development of relativity and quantum mechanics. The idea of local symmetry in Einstein's 1916 formulation of general relativity gave birth to the idea of *gauge symmetries* studied by Weyl in 1919. Quantum field theory was born in the 1930s from the work of Dirac, Heisenberg and Pauli but suffered from the disadvantage of having short-range divergences. A way of making sense of these divergences appeared with the development of the renormalization program of Feynman, Schwinger, Tomonaga and Dyson in the late 1940s. This in turn led to the development of *quantum electrodynamics* (QED); the quantum extension of Maxwell's field equations. QED is extremely successful in describing the interaction of electrons with light; its $O(e^6)$ prediction of the electron magnetic moment agrees with experiment up to at least 10 significant figures ! Amazingly, QED can be completely written down by requesting that the theory has U_1 gauge symmetry and that it is renormalisable. The requirements of gauge symmetry and of renormalisability put strong constraints on the types of possible theory and it is these constraints that have led to the Standard model. The gauge concept was generalised to non-Abelian groups by Yang, Mills and Shaw in 1954 and laid the way to finding a theory of the strong force and to unifying the electromagnetic and weak forces.

In 1960, Sakurai suggested that the strong interactions should be the result of a gauge principle; this idea was not applied until the quark model had been accepted. Approximate SU_3 flavour symmetry in the hadron mass spectrum, led Gell-Mann to postulate the existence of quarks in 1964. Attempts to gauge flavour symmetry failed and it was only after the introduction of an extra quan-

tum number, called colour, by Greenberg, Han and Nambu in 1964-66, that a gauge theory of the strong forces could be written down. The action for quantum chromodynamics (QCD) was written down in 1973 by Fritsch, Gell-Mann, Gross, Leutwyler, Weinberg and Wilczek. The problems still remained of why one never observes free quarks and why the quarks inside hadrons appear to be free at high energies. These were answered by the discovery of asymptotic freedom in 1973 by Gross, Wilczek and Politzer and led to QCD being adopted as the theory of the strong force.

In parallel with the development of QCD, the unification of the weak and the electromagnetic forces was being pursued. In 1958, Feynman, Gell-Mann, Marshak and Sudarshan postulated that the weak interaction was of the form V-A; the weak force was a chiral theory. Attempts were made to gauge a unified weak and electromagnetic theory using such groups as SU_2, $SU_2 \otimes SU_2$ and $SU_2 \otimes U_1$ by Georgi, Glashow, Salam and Ward. The idea behind unification was that it might lead to a theory of weak forces that would be renormalisable. For the weak forces to be weak in such unified models, it was necessary to have massive gauge bosons mediating the weak force. Putting in explicit mass terms led to non-renormalisable theories and so it was only after the work on spontaneous symmetry breaking, performed by Anderson, Brout, Englert, Goldstone, Guralnik, Hagen, Higgs, Jona-Lasinio, Nambu and Kibble, that it became possible to write down a unified electroweak model. This was done by Weinberg in 1967 and Salam in 1968 and they conjectured that the unified $SU_2 \otimes U_1$ electroweak theory with spontaneously broken gauge symmetry was renormalisable. The proof of this was supplied by 't Hooft in 1971. The discovery of neutral currents in 1973 led to the Glashow-Salam-Weinberg model being accepted as a model of the electroweak interactions.

Therefore, by the mid 1970s there existed two models which proposed to explain three of nature's four forces. Putting these together into a model with $SU_3 \otimes SU_2 \otimes U_1$ gauge symmetry gives what is known as the *Standard model.* So far, the Standard model has not been contradicted by any experimental data. The future lies in understanding how the Standard model behaves and in understanding the origin of the Standard model.

1.2 The Standard Model

In this section, I will describe the main features of the 3-generation minimal Standard model.

1.2.1 Particle Content

The Standard model (SM) is built on the gauge group $G = SU_3 \otimes SU_2 \otimes U_1$. The gauge bosons transform as the adjoint representations of G. There are eight gluons G^a_μ where $a = 1, \ldots, 8$ transforming as $(8,1)_0$ and they mediate the strong colour force. The $(n,m)_y$ denotes the representation of G which is n-dimensional for SU_3, m-dimensional for SU_2 and has a hypercharge equal to y for the U_1 group. The weak force is mediated by the gauge bosons W^a_μ where $a = 1,2,3$ and they transform as $(1,3)_0$. The hypercharge force is mediated by B_μ and it transforms as $(1,1)_1$. The observed Z and γ vector bosons are made from linear combinations of W^3 and B and the hypercharge Y is assigned by the relation $Y = Q - T_3$ where Q is the electric charge.

The leptons consist of the the right-handed singlets e^-_{iR} transforming as $(1,1)_{-1}$ and the left-handed doublets $L_i = (\nu, e^-)_{iL}$ transforming as $(1,2)_{-1/2}$. The i can be 1, 2 or 3 and it labels the generations.

The quarks consist of the right-handed singlets u_{iR} transforming as $(3,1)_{2/3}$, the right-handed singlets d_{iR} transforming as $(3,1)_{-1/3}$ and the left-handed doublet $Q_i = (u,d)_{iL}$ transforming as $(3,2)_{1/6}$.

The minimal SM also contains a spin-0 complex Higgs doublet ϕ transforming as $(1,2)_{1/2}$ and its conjugate $\phi' = i\tau_2\phi^*$ transforming as $(1,2)_{-1/2}$.

1.2.2 Pure Gauge Sector

The pure gauge part of the action for gauge bosons A^a_μ is given by

$$\mathcal{S} = \int d^4x \frac{1}{2g^2} Tr\left(F_{\mu\nu}F^{\mu\nu}\right)$$

The Tr denotes a trace over the adjoint representation matrices appearing in the energy-momentum tensor $F_{\mu\nu}$ which is defined as $F_{\mu\nu} = [D^a_\mu, D^a_\nu]$ where D_μ is the covariant derivative $\partial_\mu + igA^a_\mu T^a$ with the T in the adjoint representation.

In the SM, the sum of the above action with $A^a_\mu = G^a_\mu$, $A^a_\mu = W^a_\mu$ and $A^a_\mu = B^a_\mu$ is taken. Three different values of bare coupling are taken for the g appearing in the covariant derivative.

1.2.3 Matter fields

The action for the massless fermionic matter fields is given by

$$\mathcal{S} = \sum_{i=1}^{3} \int d^4x \left(\overline{e}_i \not{D} e_i + \overline{L}_i \not{D} L_i + \overline{Q}_i \not{D} Q_i + \overline{u}_i \not{D} u_i + \overline{d}_i \not{D} d_i\right)$$

The D in this expression is the covariant derivative

$$D = \partial + igB^a T^a_B + ig'W^a T^a_W + ig''G^a T^a_G$$

The representation matrices T are in the representation of the fields they act upon. This action succinctly contains all the matter-gauge interactions in the SM and extends the old approach of *minimal coupling.*

1.2.4 Mass generation

Both the weak vector bosons and all the fermions apart from the neutrinos, are observed to have mass. The process of giving these particles mass in the SM relies on introducing a Higgs field. The Higgs field transforms as some representation of the gauge group and gauge-invariant combinations of the Higgs field with

gauge and matter fields can be constructed. The Higgs potential is so arranged that the Higgs field acquires a non-zero Vacuum Expectation Value (VEV) and hence gauge symmetry is spontaneously broken. The non-zero VEV gives soft-mass terms to the gauge and matter fields via the gauge-invariant interaction terms. By this mechanism, masses can be given to the gauge bosons and to the fermions without sacrificing renormalisability.

In the minimal SM model the action for the Higgs field is given by

$$\mathcal{S} = \int d^4x \left((D_\mu \phi^\dagger)(D_\mu \phi) - V(\phi) \right)$$

and the *phenomenological* potential, chosen to give a non-zero VEV is taken as

$$V(\phi) = -\mu^2 \phi^\dagger \phi + \lambda (\phi^\dagger \phi)^2$$

At the classical level, this gives a VEV of $\phi^\dagger \phi = v^2/2$ with $v = \mu/\sqrt{\lambda}$. Because D is the covariant derivative, the VEV is coupled to the gauge fields and at the classical level gives the vector bosons a mass of $M_W^2 = g^2 v^2/4$.

Yukawa couplings are used to give the fermions mass. The most general gauge-invariant Yukawa couplings that can be written down are

$$\mathcal{S} = \int d^4x \left(f_{ij} \overline{e}_i \phi^\dagger L_j + g_{ij} \overline{d}_i \phi^\dagger Q_j + h_{ij} \overline{u}_i \phi'^\dagger Q_j + h.c. \right)$$

Note that these are the only terms in the SM which mix fermions from different generations. The fermionic masses can be diagonalised by applying biunitary transformations $\psi \rightarrow U_R \psi_R + U_L \psi_L$ to the fermion fields. Doing this introduces a 3×3 unitary mixing matrix into the charged-current interactions known as the Kobayashi-Maskawa mixing matrix.

1.2.5 Questions

Having described the Standard model, I now wish to mention a few questions it poses. Firstly, there is the question of where did all the gauge coupling constants, the mixing angles and the Yukawa couplings come from ? Secondly, why are there 3 repetitions of the first generation ? And thirdly, what values should be used for λ and μ in the Higgs potential ?

1.3 Lattice Gauge Theory

The SM has been mostly understood by calculating Feynman diagrams to low order in the coupling constants. The resulting perturbative results have been remarkably sucessful in fitting the experimental data. However, there are aspects of the Standard model that require a non-perturbative understanding. Lattice gauge theory is a technique that can be used to study the non-perturbative nature of quantum gauge field theories.

1.3.1 Introduction

Lattice gauge theory (LGT) was developed by Kenneth Wilson in 1974 in order to study quark confinement in QCD [5]. It allows the tools of condensed matter physics to be applied to the study of quantum field theories. The most powerful tool that is being used is direct numerical simulation by using Monte-Carlo techniques. Lattice gauge simulations of non-perturbative field theories have the advantage that, in principle, the statistical and systematic errors are controllable.

1.3.2 The Method

In this section, I will illustrate the salient features of lattice gauge theory by focussing on a field theory containing only one real scalar field.

There are two approaches to LGT. In the Hamiltonian approach only space is replaced by a discrete lattice; time remains continuous. The fields at each spatial site are evolved through time using the canonical momenta obtained from the Hamiltonian. This approach has been superceded by the Euclidean approach which I will now discuss.

All scattering amplitudes in particle physics can be obtained from time-ordered expectation values of products of fields and these in turn can be obtained from

the action of the model using the functional integral approach [6]. Consider the partition functional

$$Z[J] = \int d[\phi] \exp\left(i \int_x \mathcal{L}[\phi] + J\phi\right) \tag{1.1}$$

This contains all the inforamtion about the system with action $\mathcal{S}$. For example the connected 2-point Greens function is given by

$$< 0 \mid T\phi_x\phi_y \mid 0 >_c = \frac{\delta^2 \ln Z}{\delta J_x \delta J_y}\Bigg|_{J=0}$$

The functional integral is an ill-defined quantity mathematically; to define it one has to introduce a short-distance regulator. In lattice gauge theory, this is done by replacing the functional integral over fields at all space-time points by the product of integrals over fields living on a finite lattice; heuristically, one replaces all derivatives by finite-differences and all space-time integrals by sums over the lattice. Furthermore, one analytically continues in the time direction $t \rightarrow it$ with the caveat that one will be able to continue back again after calculating some quantity ; for some quantities it is not necessary to analytically continue the result back. The result of these two operations is to transform the partition functional into

$$Z[\phi] = \prod_x \int d\phi_x \exp\left(-\sum_x \mathcal{L}[\phi] + J\phi\right) \tag{1.2}$$

This can be rewritten as

$$Z[\phi] = \sum_{\{\phi\}} \exp(-\frac{1}{kT}(H[\phi] + \sum_x J_x\phi_x))$$

which is the partition function for a 4-dimensional statistical mechanical system. Because of this analogy, one can then use the following tools of condensed matter physics:

- **Low-T expansions** These are expansions in powers of a small coupling describing spin-wave excitations; the spin-waves are propagating particles and the technique is that of the usual Feynman diagrams.
- **High-T expansions** These are expansions in powers of inverse couplings.
- **Mean-field theory** Away from phase transitions, the fluctuations in the fields are small and one can make self-consistent saddle-point approximations.

- **Monte-Carlo simulations** Computers can be used to simulate the system directly by using Monte-Carlo techniques to generate configurations with the appropriate Boltzmann distribution.

- **Renormalization Group** Close to critical phase transitions, the machinery of the renormalization group can be used to find critical exponents and discuss irrelevant operators.

Equation (1.2) is only an analytically-continued approximation to equation (1.1). When is the approximation a good one ? To answer this question, it is convenient to talk in terms of correlation lengths associated with operators. By inserting eigenstates of the Hamiltonian and by using the relation between timeslice operators

$$O(t) \;=\; e^{Ht}O(0)e^{-Ht}$$

one can show that

$$< 0 \mid TO(t)O(0) \mid 0 > \;=\; \sum_{n=1}^{\infty} e^{-E_n t} \| < n \mid O(0) \mid 0 > \|^2$$

In the limit that $t \rightarrow \infty$ one obtains

$$< 0 \mid TO(t)O(0) \mid 0 > \approx e^{-E_1 t} \tag{1.3}$$

where E_1 is the energy of the first-excited state and is called the mass gap M. The correlation length associated with operator O is defined as $\xi = 1/M$ and defines a characteristic length in the system. If the correlation length is less than about 1, the excitations from operator O will decay rapidly in propagating across the lattice and hence will be very sensitive to the coarse-grained nature of the lattice. In this regime, the approximation is not a good one because particle propagation is strongly affected by short-distance effects which will be referred to as Ultra-Violet Finite Size Effects (UVFSE). To avoid UVFSE, one should tune the bare parameters in the action to values where the correlation length diverges. In condensed matter parlance this is known as a critical point and is a singularity that separates the system into regions of different behaviour known as phases. Two problems occur on approaching a critical transition. Firstly, at some stage the correlation length will become as large as the size of the lattice.

At this stage, the finite size of the box will cause the system to behave differently to that of the system in unbounded space-time; this is known as an Infra-Red Finite Size Effect (IRFSE). To combat IRFSE, one should increase the lattice size as one approaches the critical transition. The second problem is known as *critical slowing down.* Near a critical transition, long-range order occurs and the many degrees of freedom in the system will start to behave cooperatively. To simulate such highly-correlated systems numerically requires increasing amounts of computer time.

1.3.3 Gauge fields

The initial impetus for studying Lattice QCD (LQCD) was the search for a proof to show that QCD had confined quarks. Wilson, in 1974, invented LGT as a means of doing this and devised a clever scheme for putting gauge fields on a lattice in a gauge-invariant way. The scheme was inspired from Mandlestam's path-ordered exponential approach. A gauge field A_μ can be thought of as connection between two space-time points:

$$\phi(x) \;=\; P\exp\left(ig\int_y^x A_\mu dx^\mu\right)\phi(y)$$

where P means order the exponentiated A_μ in the order that they occur in the path $x \rightarrow y$. On the lattice, this amounts to putting matrices belonging to a gauge group on the links of the lattice and then using them to connect matter fields on the sites. The gauge links are given by

$$U_\mu(x) \;=\; \exp(igaA_\mu(x))$$

A term has to be placed in the action in order to generate the dynamics for the gauge links and also must give the continuum pure gauge action as one approaches the critical point. The Wilson term is given by

$$S_{gauge} \;=\; \frac{-2}{g^2}\sum_{x,\mu,\nu}\mathrm{Re}\,\mathrm{Tr}\,U_\mu(x)U_\nu(x+\hat{\mu})U_\mu^{-1}(x+\hat{\nu})U_\nu^{-1}(x)$$

This is the simplest term that can be used in the action that gives the correct continuum limit. The use of the invariant Haar measure for the gauge links,

allowed Wilson to perform strong-coupling expansions in powers of $1/g$. Observables known as *Wilson loops* show *area law* behaviour implying that the inter-quark potential grows linearly with quark separation. This indicates that quarks are confined in the strong-coupling regime. Unfortunately, this demonstration of confinement was not enough to show that QCD has confined quarks; confinement must hold as one decreases the coupling towards the critical transition at $g = 0$. The possibility arises of a phase transition occuring at some intermediate value of coupling beyond which, the quarks become deconfined. The study of intermediate values of coupling necessitated the use of Monte-Carlo techniques.

1.3.4 Monte-Carlo Simulations

To estimate expectation values of an observable O by using numerical simulations one performs the following procedure. A sequence of field configurations C_i with $i = 1, \ldots, N_c$ are generated with a probability distribution $\propto \exp(-\mathcal{S})$ and on each configuration the operator O is measured and is denoted by O_i. The expectation value $< 0 \mid O \mid 0 >$ is given by

$$< 0 \mid O \mid 0 > \;=\; \lim_{N_c \to \infty} \frac{1}{N_c} \sum_{i=1}^{N_c} O_i \tag{1.4}$$

$$\tag{1.5}$$

The expectation value can then be analytically continued back to Minkowski space to give physical results if necessary.

The sequence C_i is invariably generated by a one-step $C_i \to C_{i+1}$ stochastic process known as a Markov process; the probability of $C_i \to C_{i+1}$ is denoted by $p(C_i \to C_{i+1})$. Sufficient conditions for a Markov process to generate a distribution with probability $\propto \exp(-\mathcal{S})$ are:

1. **Ergodicity** The probability of obtaining any configuration is never zero.
2. **Detailed Balance** The system is reversible in the sense that $e^{-S_i} p(C_i \to C_{i+1}) = e^{-S_{i+1}} p(C_{i+1} \to C_i)$ where S_i is the action $\mathcal{S}$ for configuration C_i.

These conditions ensure that the correct fixed point distribution is reached.

1.3.5 Fermions

The study of fermions in LGT is more difficult than the study of scalar and gauge fields. This section is devoted to explaining briefly the techniques used to study fermions.

In performing the Wick rotation, the metric changes from the Minkowski metric $g_{\mu\nu}$ to the Euclidean metric $\delta_{\mu\nu}$ and this in turn causes the Clifford algebra to change. The anti-commutation relations on the Dirac gamma matrices change from $\{\gamma_\mu, \gamma_\nu\} = 2g_{\mu\nu}$ to $\{\gamma_\mu, \gamma_\nu\} = 2\delta_{\mu\nu}$. The gamma matrices become representations of a different algebra. A heuristic rule for transforming between Minkowskian and Euclidean gamma matrices is $\gamma_0 \rightarrow \gamma_4$ and $\gamma_j \rightarrow i\gamma_j$. The j are space indices taking values 1, 2 and 3 and the 0 and 4 directions are the Minkowskian and Euclidean time directions respectively. The rule has the effect that in Euclidean space-time the gamma matrices are all hermitian $\gamma_\mu = \gamma_\mu^\dagger$. Furthermore, $\gamma_5 = i\gamma_0\gamma_1\gamma_2\gamma_3$ transforms to the hermitian $\gamma_5 = \gamma_1\gamma_2\gamma_3\gamma_4$.

The next problem with fermions is caused by their anti-commuting nature. To describe fermions using the functional integral approach, one has to introduce the anti-commuting quantities known as Grassmann variables. These allow formal manipulations to be performed but have the disadvantage of having no representations as real numbers [1]. No Monte-Carlo simulations using Grassmann variables are possible. To simulate fermions, one has to *integrate* them out of the path integral

$$\int d[\overline{\psi}]d[\psi]\exp(-\overline{\psi}M\psi) \;=\; \det M$$

and this leads to having to simulate the fermionic determinant $\det M$. This quantity has the properties of being non-local, non-linear and very time-consuming to calculate. If M contains interactions with bosonic fields such as gauge fields, then the $\det M$ accounts for the effects of the fermions acting back on the bosonic fields. In terms of Feynman diagrams, this corresponds to simulating the effects of quark loops. The quenched approximation is the approximation in which the effects of quark loops are neglected; the determinant is assumed to be constant. Unquenched simulations are known as *dynamical* simulations and consume far

[1] except the trivial representation of 0!

more computer time. In a dynamical simulation one needs to know the change in $\det M$ caused by altering some of the bosonic fields and this is given by

$$\frac{\delta \det M}{\det M} = Tr(M^{-1}\delta M)$$

Hence for any change in the bosonic fields one has to calculate the inverse of the fermion matrix and this is time-consuming. The work in Chapter 3 uses one of the most recent [2] algorithms for simulating dynamical fermions.

The final and most insurmountable problem with fermions is the notorious doubling problem. In naively transcribing the Dirac operator onto the lattice, one goes from describing one species of fermion to describing many species of fermions. The lattice is, in some sense, too good a regulator and gives rise to no axial anomaly [7]; extra fermionic species appear to cancel what would be an anomaly [8,9]. For vector gauge theories there exist the Wilson and the staggered methods of reducing the doubling [10,11]. For chiral gauge theories there do not appear to be any well-proven ways of reducing the doubling and no-go theorems show that under very mild conditions there will always be doubling [12,13,14]. More will be said about doubling in the later chapters.

1.4 Thesis Morphology

The rest of this thesis is structured as follows:

- **Chapter 2: Lattice QCD** An examination of the coloured threads in the tapestry by using quenched lattice QCD in order to find the low-lying hadronic mass-spectrum.
- **Chapter 3: Yukawa Couplings** Unpicking a few of the weak threads in the tapestry and looking at them in more detail. A toy Yukawa-coupled Fermion-Higgs model is studied numerically.
- **Chapter 4: Finer Threads** Moving beyond the SM, an attempt is made to replace space-time by a discrete fabric.

[2] and apparently most efficient

Chapter 2

Lattice QCD

"It is the mark of a wise man not to demand more accuracy than the subject matter allows, for precision is not to be sought alike in all discussions"

Aristoteles

Quantum chromodynamics (QCD) was discovered in 1973 [15,17,18]. It is a renormalisable quantum gauge theory with gauge group SU_3 and has three colours of quarks transforming in the fundamental representation. The discovery of *asymptotic freedom* [15,16,19,20] led to it been proposed as a theory of the strong force. Asymptotic freedom is the property that the running coupling constant decreases with increasing momentum scale; the constituent quarks become asymptotically free at high energies.

QCD provides an elegant description of deep-inelastic lepton-nucleon scattering where at such large momentum scales perturbation theory is valid. At lower scales, the coupling constant increases and perturbation expansions are no longer valid. Such features as confinement, Spontaneous Symmetry Breaking (SSB) of the global chiral symmetry and the hadronic mass-spectrum can only be answered by non-perturbative techniques. In 1974, Kenneth Wilson proposed studying QCD by using the lattice as a gauge-invariant regulator [5]. Since 1974, Lattice Quantum chromodynamics (LQCD) has made great progress towards the understanding of the non-perturbative nature of QCD.

The earliest attempt to use LQCD to predict the low-lying hadron masses was in 1981 [21]. In the past 7 years, vast human and computer resources have been applied in the hope that LQCD will yield accurate quantitative masses which can then be compared with the experimentally measured masses. The Edinburgh work [22,23,24,25,26,27,28,29,30] has focussed on trying to decrease the statistical and systematic errors inherent in the mass estimates. This chapter is organised as follows:

1. **Introduction** - a discussion of the action, its symmetries and how to obtain estimates of physical quantities.
2. **Methodology** - the techniques that were used.
3. **Results** - results obtained for masses and f_π.
4. **Physical Limit** - how the results compare with experiment.
5. **Conclusions**

In this chapter, neither will I review the vast literature on this subject nor will I give every detail of the Edinburgh project. Instead, I intend to try and present what I consider to be the essential apsects of this work and hope to give some guidelines for future simulations.

2.1 Introduction

2.1.1 Action

The action S, that we used, is the sum of a pure-gauge part S_{gauge} and a fermion part S_{quark}. For the pure-gauge part we took the Wilson action [5]

$$S_{gauge} = \frac{-2}{g^2} \sum_{x,\mu,\nu} \mathrm{Re}\,\mathrm{Tr}\, U_\mu(x) U_\nu(x+\hat{\mu}) U_\mu^\dagger(x+\hat{\nu}) U_\nu^\dagger(x)$$

The U are SU_3 matrices living on the links of the lattice and all colour indices are suppressed. For the fermion part we chose the staggered fermion action [31]

$$\begin{aligned} S_{quark} &= \sum_{x,y} \overline{\chi}_x M_{xy} \chi_y \\ M_{xy} &= m\delta_{xy} + \frac{1}{2}\sum_{\mu=1}^{4} \eta_\mu(x)(U_\mu(x)\delta_{y,x+\hat{\mu}} - U_\mu^\dagger(x-\hat{\mu})\delta_{y,x-\hat{\mu}}) \\ \eta_\mu(x) &= \prod_{\nu<\mu}(-1)^{x_\nu} \end{aligned} \tag{2.1}$$

The action S has two bare-parameters g and m. At $g = 0$ and $m = 0$, the action has an ultra-violet renormalisation group fixed-point. In simpler terms this means that the correlation lengths on the lattice will diverge as this point is approached i.e. it is a critical point. As explained in Chapter 1, this point is the one relevent to the behaviour of the theory in the continuum. What does our action look like close to this point ?

As $g \to 0$, the $U_\mu(x)$ align to unit matrices because this configuration gives the least action. Writing $U_\mu(x) = \exp(igA_\mu(x))$ and expanding in powers of g allows us to show that

$$S_{gauge} \rightarrow \int d^4x \frac{1}{2g^2} Tr(F_{\mu\nu}(x)F_{\mu\nu}(x))$$

F is defined as $F_{\mu\nu} = [D_\mu, D_\nu]$ with the covariant derivative expressed as $D_\mu = \partial_\mu + igA_\mu$. Hence the gauge part of the action looks like that of QCD as $g \to 0$.

For the fermion part, it is convenient to define quark fields living on a doubly-spaced lattice [32,33]:

$$q^{\alpha i}(x) = \frac{1}{32}\sum_\eta \Gamma_\eta^{\alpha i} \chi(2x+\eta)$$

The η have binary components and label the sites in a binary hypercube containing 16 sites. The α is a Dirac index and the i is a *flavour* index running from 1 to 4. The Γ are products of Dirac matrices and are defined as $\Gamma_\eta = \gamma_1^{\eta_1}\gamma_2^{\eta_2}\gamma_3^{\eta_3}\gamma_4^{\eta_4}$. The fermion action can be now rewritten as

$$\begin{aligned} S_{quark} &= m\sum_y \overline{q}(y)(1\otimes 1)q(y) \\ &\quad + \sum_\mu \overline{q}(\gamma_\mu \otimes 1)D_\mu q \\ &\quad + \sum_\mu \overline{q}(\gamma_\mu \otimes t_\mu t_5)D_\mu^2 q \end{aligned} \tag{2.2}$$

Refer to Appendix A for definitions of lattice D_μ and D_μ^2. The t are *flavour* changing matrices defined as $t = \gamma^*$; note that all flavour and implicit space-time indices have been contracted. As the point $g = m = 0$ is approached, the quark fields q become smoother functions of space-time with the result that the last line in the above expression becomes irrelevent. This leaves an action that looks like a QCD quark action describing four degenerate flavours of quark.

In numerical work it is useful to define $\beta = 6/g^2$. Hence our action behaves like that of 4-quark QCD as $\beta \to \infty$ and $m \to 0$.

2.1.2 Global Continuous Symmetries

For non-zero g and m, the action has only a global U_1 symmetry which is related to the conservation of particle number:

$$\begin{aligned} \chi(x) &\rightarrow e^{i\theta}\chi(x) \\ \overline{\chi}(x) &\rightarrow \overline{\chi}(x)e^{-i\theta} \end{aligned} \tag{2.3}$$

For the special case of $m = 0$ this vector symmetry is accompanied by a chiral U_1 symmetry:

$$\begin{aligned} \chi(x) &\rightarrow e^{i\varepsilon(x)\alpha}\chi(x) \\ \overline{\chi}(x) &\rightarrow \overline{\chi}(x)e^{i\varepsilon(x)\alpha} \end{aligned} \tag{2.4}$$

The phase factor $\varepsilon(x)$ is defined as $\varepsilon(x) = (-1)^{x_1+x_2+x_3+x_4}$.

Due to the vanishing of the flavour-mixing terms in (2.2), the zero-mass $U_1 \otimes U_1$ symmetry enlarges to a $U_4 \otimes U_4$ symmetry as $\beta \to \infty$. This has a consequence for the mass-spectra of different lattice operators. The spectra of operators with the same continuum quantum numbers should become degenerate at large enough β. This effect is known as Flavour Symmetry Restoration (FSR) and is a signal that the continuum is being reached.

The transformation in (2.4) can be used to generate the two useful Ward Identities (WI):

$$\frac{\partial}{\partial m} Tr G(x,x) = -\sum_y \varepsilon^{x-y} \|G(x,y)\|^2 \tag{2.5}$$

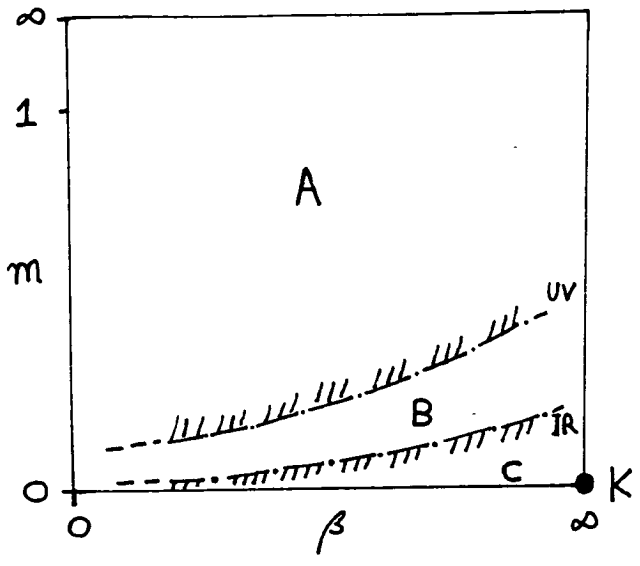

Figure 2.1: Parameter Space for LQCD

$$TrG(x,x) \;=\; m\sum_{y}\|G(x,y)\|^2 \tag{2.6}$$

These are obtained from the path-integral identity $< \delta O - O\delta S >= 0$ with the O operator taken as $\overline{\chi}\chi$ and $\varepsilon\overline{\chi}\chi$. They are valid on any configuration with quenched or dynamical fermions. Identity (2.5) was found to hold to 5 significant figures on all the Edinburgh data. Identity (2.6) is a relation between the chiral condensate $< \overline{\chi}\chi >$ and the pion propagator $\|G(x,y)\|^2$. It was verified on 8 configurations at $\beta = 6.15$ up to 5 significant figures accuracy over the whole range of masses and at $\beta = 6.30$ at $m = 0$.

From chiral perturbation theory and the PCAC hypothesis, one can derive [34]:

$$f_\pi^2 M_\pi^2 \;=\; \frac{m}{2} < \overline{\chi}\chi > + O(m^2 \log m) + O(m^2) \tag{2.7}$$

We will refer to $M_\pi^2 = Bm$ as the *PCAC relation* and $B =< \overline{\chi}\chi > /2f_\pi^2$ will be known as the *PCAC slope*. The relation will prove useful in obtaining the pion decay constant f_π and in studying IRFSE.

2.1.3 Scaling and FSE

Figure 2.1 shows the bare parameter space for LQCD. As mentioned in Chapter 1, the correlation length ξ will diverge as the critical point K is approached and hence continuum behaviour will be restored at this point. The dotted line marked UV in Figure 2.1 depicts the locus $\xi = 1$ and divides the diagram into UVFSE affected and unaffected regions. The dotted line marked IR in Figure 2.1 depicts the locus $\xi = N$, where N is the lattice size, and divides the diagram into IRFSE affected and unaffected regions. Region B is the window where IRFSE and UVFSE are negligible and is the region where useful lattice work can be performed.

Close to K, perturbation theory is possible and 2-loop calculations for quenched QCD [35] predict that the correlation lengths ξ_i should behave as

$$\xi_i = c_i \left(\frac{8\pi^2\beta}{33}\right)^{-51/121} \exp\left(\frac{4\pi^2\beta}{33}\right)\left(1 + O(g^2)\right) \tag{2.8}$$

The c_i are constants which differ for differing operators i. At large β, this expression, without the $O(g^2)$ term, should be valid and behaviour of this form is called *Asymptotic Scaling (AS)*. At smaller β, one might expect the ratios ξ_i/ξ_j to be equal to c_i/c_j and this behaviour is referred to as *scaling*. To be sure that LQCD is giving continuum results it is necessary to check that AS is occuring. In obtaining physical quantities from lattice quantities we will use Eqn. (2.8) together with values obtained by matching LQCD string tension estimates $\sqrt{\sigma} \approx 10^2 \Lambda_{lat}$ to the experimental value of $\sqrt{\sigma} = 420$ MeV. Thus we take the physical lattice spacing a to be:

$$a = \frac{1}{\Lambda_{lat}} \left(\frac{8\pi^2\beta}{33}\right)^{51/121} \exp\left(\frac{-4\pi^2\beta}{33}\right) \tag{2.9}$$

with $\Lambda_{lat} = 4.2$ MeV [36,37].

Two limits are involved in obtaining physical results from LQCD. The *continuum limit* is defined to be the limit obtained by taking m and β to point K in Figure 2.1. The correlation lengths will go to infinity with the outcome that the lattice will behave like a continuum; it will look very fine-grained. The *infinite-volume limit* is defined to be the limit obtained by taking the lattice size N to infinity. As the correlation lengths become larger, the box size should increase to accommodate them. Taking both these limits, in this way, will be referred to as taking the *physical limit.*

2.2 Methodology

In this section, I will review the techniques that were used in the Edinburgh project.

2.2.1 Overview

Quenched calculations of hadron masses require the following steps:

1. The generation of a large ensemble of statistically independent gauge configurations with a probability distribution $\propto \exp(-S_{gauge})$.
2. The inversion of the large sparse fermion matrix M_{xy} on each gauge configuration in order to find the quark propagator.
3. Quark propagator multiplications in order to obtain meson and baryon multiquark propagators.
4. Summing of hadron propagators over spatial sites so as to produce zero-momentum hadron *timeslice* propagators.
5. Summation of the timeslice propagators over the whole ensemble and subsets of the ensemble of configurations resulting in a mean propagator and a number of blocked propagators.
6. Exponential fits to the mean and blocked propagators, the parameters of which, can be used to find means and variances of hadron masses.

Table 2.1 is a summary of the configurations that were generated as part of this procedure. The numbers, at each β and m, are the number of gauge configurations used in the ensemble. The + and - denote the adoption of periodic and antiperiodic spatial boundary conditions for the fermions. The *size* is the lattice size and so, for example, $16^3 \times 24$ means 16 sites in the space directions and 24 sites in the time direction. The number of Monte Carlo sweeps between each configuration in each ensemble is shown together with the algorithm chosen to

Mass	Beta			
m	5.70	6.00	6.15	6.30
0.50	8-	32-	32+	32-
0.16	8-	32-	32+	32-
0.09	8-	32-	32+	32-
0.04	8-	32-	32+	32-
0.01	8-	32-	32+	32-
size	16^4	$16^3 \times 24$	$16^3 \times 24$	$16^3 \times 24$
#sweeps	448	224	176	224
#invert	CG	SOR	SOR	SOR

Table 2.1: Edinburgh configurations.

invert the fermion matrix. In addition to these configurations, there were also the following items:

1. 8 configurations at $\beta = 5.7$ on a $8^3 \times 16$ lattice.
2. 8 configurations at $\beta = 6.0$ on a 16^4 lattice.
3. 24 configurations at $\beta = 6.15$ on a $16^3 \times 24$ lattice with antiperiodic spatial boundaries for the fermions.
4. 4 configurations at $m = 0.005$, 0.003, 0.001 and $\beta = 6.15$.
5. 4 configurations at $m = 0.0025$, 0.0 and $\beta = 6.30$.

Items 1 and 2 were early runs on smaller lattices whilst the rest of these items were performed in order to try and understand more about IRFSE. Unless stated otherwise, the results in the remainder of this chapter derive from the configurations shown in Table 2.1.

The algorithms were implemented on the DAP (refer to Appendix B) in the language of DAPFORTRAN with the exception of the fitting routines which ran in FORTRAN on a VAX 11/750. Optimisation of the algorithms in order to

minimise execution time and minimise memory allocation, is crucial in LQCD and is a very important aspect of the work. For brevity's sake, only a sketch of this will be given in this thesis but the interested reader is advised to refer to [38] for a complete discussion.

2.2.2 Gauge Configurations

Metropolis [39], heat-bath [40,41] and more recently overrelaxation [42], are the methods used in LQCD to generate an ensemble of gauge configurations with distribution $\propto \exp(-S_{gauge})$. The Edinburgh configurations were made using the *two subgroup pseudo-heatbath algorithm* [43] with 24-bit real arithmetic. The SU_3 matrices were scaled by 32000 and stored as two rows of six 16-bit integers. The boundaries for the gauge configurations were chosen to be periodic in the space directions and Dirichlet in the time direction. Dirichlet in time meant that the gauge and fermion fields were zero on timeslices 0 and $N_t + 1$ where N_t is the lattice size in the time direction. This had the advantage of allowing gauge configurations to be extended in the time direction when necessary [26] and also the advantage of allowing timeslice propagators to be measured over a longer range of times than with periodic boundary conditions.

2.2.3 Quark Propagators

To find G(x,y) the following equation has to solved on each gauge configuration:

$$\sum_x M_{zx} G(x,y) \;=\; \delta_{zy} \tag{2.10}$$

M is the fermion matrix defined in (3.1) [1]. For a 16^4 lattice this requires the inversion of a sparse complex matrix of rank 196608. This is a time-consuming problem so the following tricks have to be applied.

Firstly, one specialises to the simpler problem of solving (2.10) not for all y but only for one particular y. This gives information on how quarks propagate from

[1] Although we are only attempting to find part of the inverse matrix, in what follows we will loosely refer to this procedure as *inversion*.

one source point to all final points. We took y to be at (1,1,1,5) with the hope that $y_4 = 5$ was far enough from the Dirichlet boundaries that finite time effects became negligible.

The second trick relies on partitioning the lattice into *even* and *odd* sites. Define the matrix $E_{xy} = \varepsilon(x)\delta_{xy}$ where $\varepsilon(x) = (-1)^{x_1+x_2+x_3+x_4}$ and create the projection matrices $P_+ = (1+E)/2$ and $P_- = (1-E)/2$. P_+ and P_- project out even and odd sites respectively. Left-multiply $(\not{D} + m)G = \delta$ by P_- to give $P_-G = -\not{D}P_+G/m$ when the source is assumed to be on an even site. Next, left-multiply $(\not{D} + m)G = \delta$ by P_+ to get $\not{D}P_-G + mP_+G = \delta$ and then use the expression for P_-G to obtain $(-\not{D}^2 + m^2)P_+G = m\delta$. This partitioning has resulted in replacing the eqn. (2.10) by the two equations:

$$\begin{aligned} (-\not{D}^2 + m^2)P_+G &= \delta \\ P_-G = -\frac{\not{D}P_+G}{m} & \end{aligned} \tag{2.11}$$

These require an inversion of a matrix of half the rank of (2.10) [2] and hence there is a considerable saving in computer time.

The third trick relies on gauge transforming the SU_3 matrices to temporal gauge i.e. all the $U_4(x) = 1$. The matrix can then be partitioned into *timeslices* i.e it becomes a block matrix with inter-timeslice blocks being unit matrices. This requires less SU_3 multiplies and also reduces the amount of data needed to be paged into DAP main memory for each inversion and hence results in a speed increase. It also has the advantage that the inversions require less main memory and hence bigger lattices can be studied.

Two iterative algorithms were used to invert the Hermitian matrix $A = -\not{D}^2 + m^2$ with the criteria for convergence that the quark propagator became stable and that the hadron propagators agreed to 3 significant figures with those on gauge configurations which had been randomly gauge-transformed. At $\beta = 5.7$ the Conjugate Gradient (CG) algorithm [44] was used:

[2] All be it, more poorly conditioned than the original matrix !

To solve $Ax = b$ when $A^\dagger = A$
initial guess x_0
$p_0 = r_0 = b - Ax_0$
loop while $(r_k, r_k) > \varepsilon$ for k=0,1,2,...
$\alpha_k = (r_k, r_k)/(p_k, Ap_k)$
$x_{k+1} = x_k + \alpha_k p_k$
$r_{k+1} = r_k - \alpha_k A p_k$
$\beta_k = (r_{k+1}, r_{k+1})/(r_k, r_k)$
$p_{k+1} = r_{k+1} + \beta_k p_k$
end loop

The algorithm converged smoothly at a rate approximately $\propto m$ taking typically a few hundred iterations for $\varepsilon = 10^{-10}$ at the lower masses. After about 500 iterations (needed only at $m = 0.01$), the algorithm had to be restarted to prevent accumulation of rounding errors from giving inaccurate r_k. Conjugate gradient performed well for the 16^4 lattice at $\beta = 5.7$ but unfortunately suffered from having a high stretch factor of ≈ 6. Stretch factor, defined as the ratio of *compute time* plus *communication time* to the *compute time*, should be close to unity in order to do fast simulations. Large stretch factors imply that the computer is spending most of its time communicating data [3] rather than performing calculations. For the larger lattices at higher β it was necessary to find an algorithm with a lower stretch factor than CG and so an iterative block Succesive Over-Relaxation (SOR) algorithm was developed:

To solve $(-D^2 + m^2)G = \delta$
initial guess $G^{(0)}$
loop while $(r_k, r_k) > \varepsilon$ for k=0,1,2,...
loop for t=0,... N_t
$H = \delta_t + \frac{1}{4}G^{k+1}_{t-2} - F_{t-1}G^{k+1}_{t-1} - F_t G^k_{t+1} + \frac{1}{4}G^k_{t+2}$
$G^{k+1}_t = (1-\omega)G^k_t + \omega(C_t - D^2_t + m^2)^{-1}H$
end loop
$r_k = \delta - (-D^2 + m^2)G$
end loop

[3] with disks in this case

The propagator G is partitioned into timeslices and so G_t^k refers to the k'th iterate of G on timeslice t. C_t is 1/2 on all timeslices apart from the end ones where it takes the value 1/4 and $F_t = (\not{D}_t - \not{D}_{t-1})E$ where $\not{D}_t$ is the gauged derivative $\not{D}$ on timeslice t and E is the even/odd matrix defined previously. The inversion of $C_t - \not{D}_t^2 + m^2$ was performed by CG but required typically only 8 iterations because of the diagonally-dominant C_t term. The optimization parameter ω was tuned for each β and m value in order to find the minimum number of SOR iterations required for convergence, which were usually about a few hundred. The stretch factor for SOR at $\beta = 6.0$ was as low as 1.02. Both the CG and SOR algorithms were implemented using 32-bit real arithmetic.

2.2.4 Hadron Propagators

The quark propagator, from source site y, can be used to construct propagators $G_{oper}(x, y)$ for local operators which are made from products of the quark field. Table 2.2 shows the six operators that were investigated along with their continuum quantum numbers J^{PC}. Adjacent to the J^{PC} values are the lowest-energy hadrons that are observed experimentally in these channels.

Operator		J^{PC}		J^{PC}	
PS	$\varepsilon\overline{\chi}\chi$	0^{-+}	$\pi(140)$	0^{+-}	absent
SC	$\overline{\chi}\chi$	0^{-+}	$\pi(140)$	0^{++}	S(975)
PV	$\sum_{i=1}^{3}\eta_i\varepsilon\overline{\chi}\chi$	1^{--}	$\rho(770)$	1^{++}	$A_1(1270)$
VT	$\sum_{i=1}^{3}\eta_i\overline{\chi}\chi$	1^{--}	$\rho(770)$	1^{+-}	$B(1235)$
ALL	$\chi\chi\chi$	$\frac{1}{2}^{++}$	$N(940)$	$\frac{1}{2}^{-+}$	N(1535)
EVEN	$(1+\varepsilon)\chi\chi\chi$	$\frac{1}{2}^{++}$	$N(940)$	$\frac{1}{2}^{-+}$	N(1535)

Table 2.2: Hadron Operators.

The ε and η are as defined previously; for explicit definitions of the operators refer to [45]. Note the degeneracies in the continuum assignments of the meson operators i.e. both PS and SC give π and both PV and VT give ρ. This is an

example of FSR which is described in more detail in the results section of this chapter. The degeneracy in the baryon sector is the result of an identity that is believed to be valid on all even-sized lattices for all values of β.

Integrating out the χ and $\overline{\chi}$ and using identities such as $\epsilon(x)G_{xy}\epsilon(y) = G^{\dagger}_{yx}$ (with $\dagger$ acting only in colour and Dirac space) gives expressions for the hadron propagators $G_{oper}(x,y) =< O(x)O(y) >$ in terms of the quark propagator $G(x,y)$. For example,

$$\begin{aligned} G_{PS}(x,y) &= \|G(x,y)\|^2 \\ G_{ALL}(x,y) &= \sum_{a,b,c=1}^{3}\sum_{A,B,C=1}^{3}\epsilon_{abc}\epsilon_{ABC}G^{aA}(x,y)G^{bB}(x,y)G^{cC}(x,y) \end{aligned}$$

The ϵ is the alternating tensor acting on the colour indices a,b,c and A,B,C. Timeslice propagators are then constructed as $C_{oper}(x_4-y_4) = \sum_{x_1,x_2,x_3} G_{oper}(x,y)$ and represent the propagation of states, with the quantum numbers of the operator, from a point source at time y_4 to zero-momentum states at time x_4. Remember that in our case, $y_4 = 5$ and $1 \leq x_4 \leq N_t$ and we will set $t = x_4 - y_4$.

As explained in Chapter 1, timeslice propagators decay exponentially and hence we can attempt to fit the timeslice propagators to the form:

$$C(t) = \sum_{i=1}^{N^+} A^{i+}\exp(-M^{i+} \mid t \mid) + \sum_{i=1}^{N^-} A^{i-}(-1)^t\exp(-M^{i-} \mid t \mid)$$

The (N^+, N^-) are the number of states in the *direct (+)* and the *oscillating (-)* channels. Masses of the states are denoted by the M^i which are larger for larger i; the ground state mass is M^1. The A^i are amplitudes for the states and are related to hadronic wavefunctions. Oscillating channels are necessary because of the use of staggered fermions; they are not present in simulations with Wilson fermions. Figure 2.2 shows the oscillating nature in the VT propagator.

In the continuum limit, the ground states in the (+) and (-) channels give the masses and amplitudes for the particles shown in the left and right columns of Table 2.2. In order to obtain accurate estimates of the ground state quantities, it is necessary to include the $i > 1$ excited states in the fit because of the following reason. The operator at the point source projects onto many states such as non-zero momentum states, radially-excited states and non-continuum states.

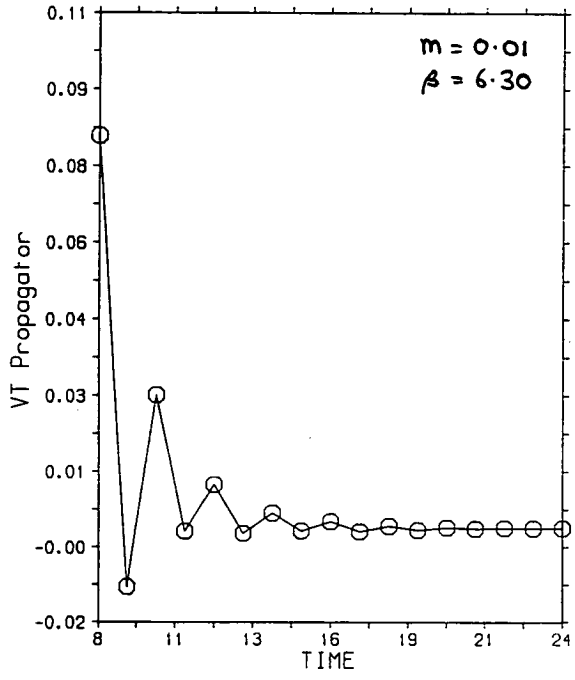

Figure 2.2: The VT timeslice propagator.

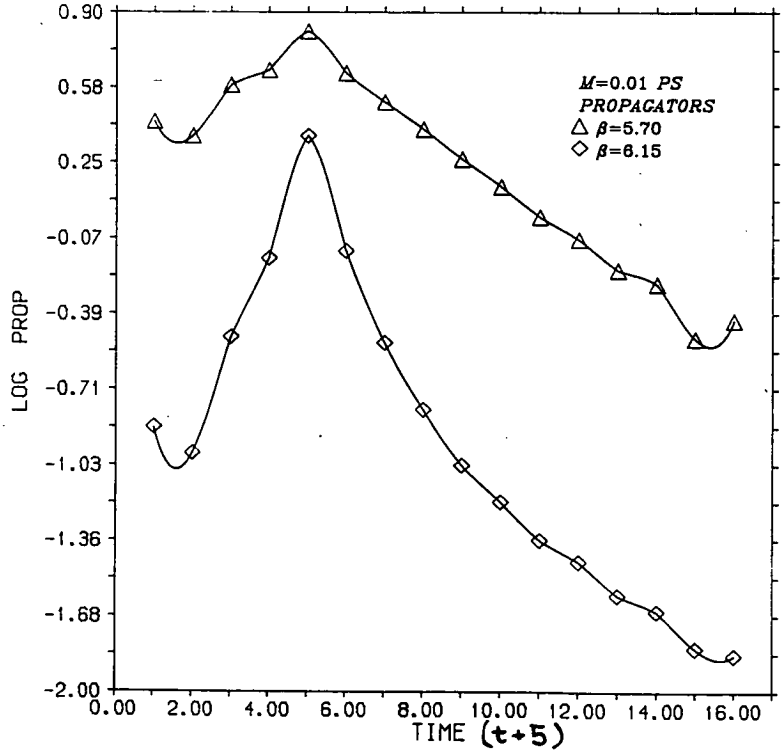

Figure 2.3: Excited states in a timeslice propagator.

At large t, these will have decayed more rapidly than the ground state resulting in a propagator containing only the required ground state. However, we can only perform fits for $0 \leq t \leq N_t - 5$ and so the limit $t \to \infty$ is not available to us. If values of t close to 0 are to be used in the fits, then excited states have to be taken into account.

Figure 2.3 shows the effect of non-continuum states on the propagator near $t = 0$ at $\beta = 6.15$ compared to the relatively uncontaminated propagator at $\beta = 5.7$. Our work has used judicious choices of (N^+, N^-) and of the ranges of timeslices $[t_{min}, t_{max}]$ included in the fits; a rule of thumb being that smaller t_{min} require larger N^+ and N^-. Fits were not performed with $t_{max} > N_t - 5$ or with $t_{min} < 0$ because of end-effects becoming large near the Dirichlet boundaries.

To find optimal fits to the parameters M and A, a program was developed to minimise χ^2 by steepest-descent. Graphical displaying of χ^2 in parameter space was required so that human intuition could be applied in directing the steepest-descent algorithm away from spurious minima. The software was written in FORTRAN and ran on a VAX 11/750. The timeslice propagators were averaged over the whole ensemble of configurations to give mean timeslice propagators which were then fitted to give values of mean M and A. Estimates of the error in M and A were obtained by fitting to blocked propagators obtained by summing over subsets of 8 configurations on the $16^3 \times 24$ lattices and over subsets of 2 configurations on the 16^4 lattice.

At $\beta = 5.7$, fits to timeslices $t \in [2 \pm 1, 8]$ were performed as follows:

- $(N^+, N^-) = (1, 0)$ and $(2, 0)$ to the PS propagator.
- $(1, 1)$ fits to SC, PV, VT, ALL and EVEN propagators

Zero N^+ or N^- signifies that no fit was made to that channel. The same types of fit were also used at the higher β except with timeslices $t \in [5 \pm 1, 14 \pm 1]$. In addition to these fits, $(2, 2)$ fits were performed for ALL and EVEN propagators and $(2, 1)$ fits were performed for SC, PV and VT propagators at $\beta = 6.0$ and 6.3.

2.3 Results

2.3.1 Summary

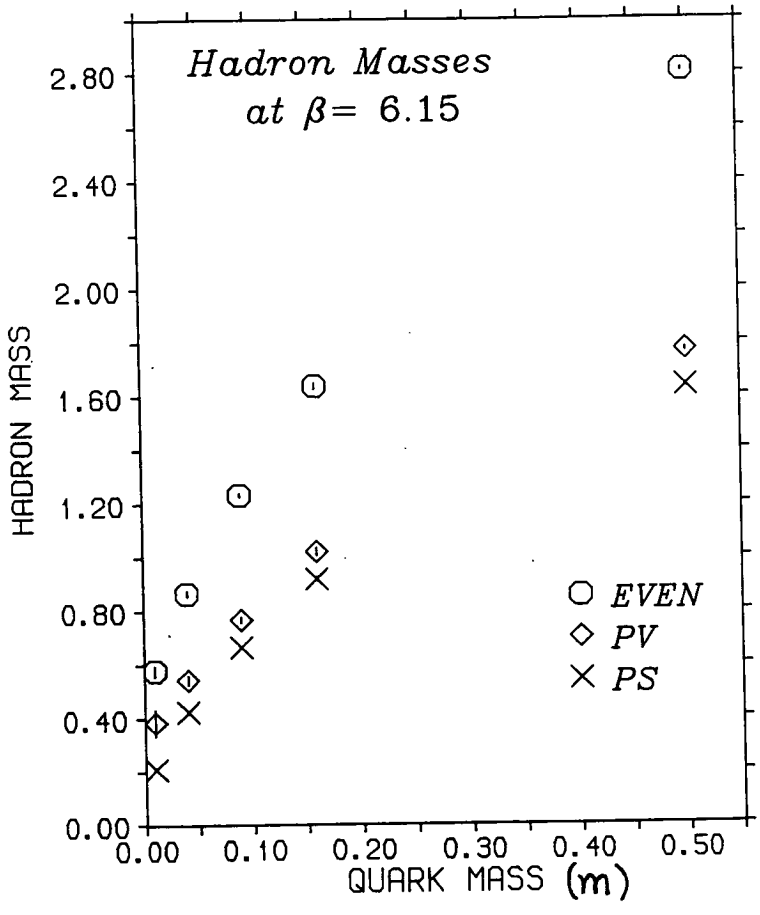

Figure 2.4: Typical results.

Figure 2.4 shows some typical results obtained at $\beta = 6.15$. For every value of β and m, the fits produced at least 3 estimates of the pion mass M_π, 2 estimates of the rho-meson mass M_ρ and at least 2 estimates of the nucleon mass M_N. Rather than present all these numbers, I will display only the ones I consider relevant to the discussion. Refer to [28,29,30] for a complete presentation of the results.

2.3.2 Pion

Mass	Beta			
m	5.70	6.00	6.15	6.30
0.50	1.661(1)	1.650(1)	1.641(1)	1.636(1)
	1.639(7)	1.658(4)	1.633(5)	1.632(3)
0.16	1.022(3)	0.972(1)	0.932(3)	0.912(1)
	0.894(260)	0.966(5)	0.916(6)	0.888(4)
0.09	0.795(5)	0.733(2)	0.682(3)	0.666(5)
	0.794(8)	0.725(6)	0.662(2)	0.642(8)
0.04	0.550(1)	0.492(2)	0.436(4)	0.437(15)
	0.549(15)	0.488(8)	0.422(4)	0.417(17)
0.01	0.273(1)	0.247(3)	0.211(5)	0.250(30)
	0.165(78)	0.245(13)	0.208(3)	0.250(26)

Table 2.3: Pion masses M_π.

Table 2.3 shows the values of M_π obtained by using the PS operator. The upper numbers are from $(1,0)$ fits and the lower ones are from $(2,0)$ fits. The SC operator gives similar results; this will be discussed later under the topic of FSR.

Figure 2.5shows the behaviour of M_π with m at $\beta = 6.15$. Note the $M_\pi^2 = Bm$ behaviour expected from Eqn. (2.7). This behaviour occurs at all β and gives B equal to 7.44, 5.81, 5.34 and 4.89 at β of 5.7, 6.0, 6.15 and 6.30 respectively; the systematic plus statistical error in these values is estimated at around 10%.

Figure 2.6shows the PCAC behaviour at $\beta = 6.30$. Note the non-zero intercept at $m = 0$. At $m = 0$, the pion is assumed to be the Goldstone boson associated with the softly-broken global chiral SU_3 colour symmetry and hence is expected to have zero mass. In a finite volume, however, degenerate vacuum states can tunnel into one another and thus true Spontaneous Symmetry Breaking (SSB) does not occur. This failure of SSB manifests itself as a non-zero Goldstone boson mass and as a vanishing of the order parameter. The non-zero intercept at $\beta = 6.3$ is, therefore, strong evidence for the IRFSE becoming important.

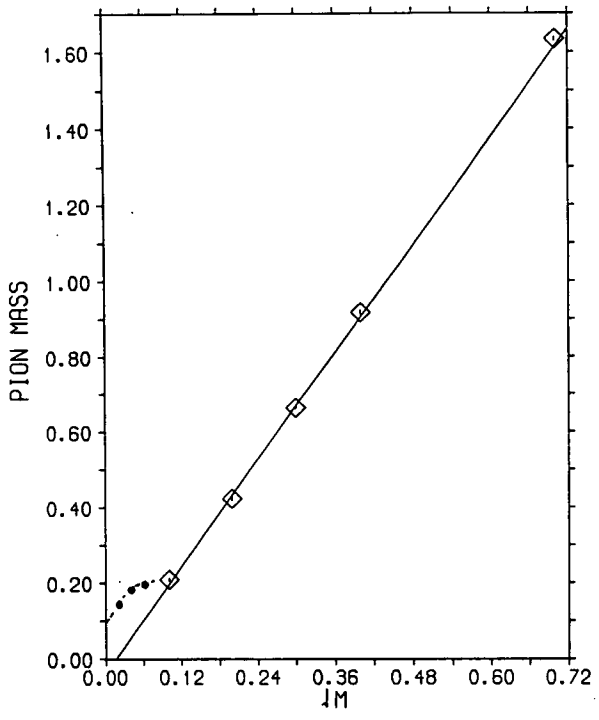

Figure 2.5: PCAC behaviour at $\beta = 6.15$.

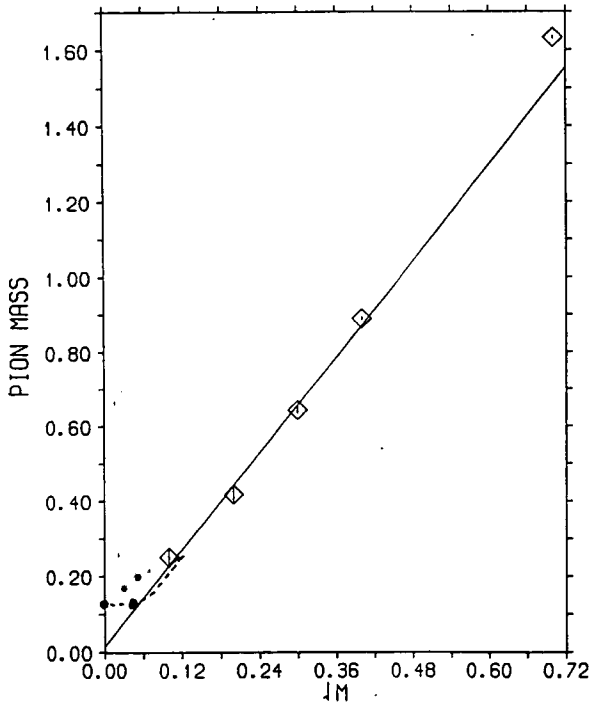

Figure 2.6: PCAC behaviour at $\beta = 6.3$.

From Table 2.3, the M_π at $m = 0.5$ can be seen to be relatively independent of β. This can be understood as a UVFSE. At $M_\pi \approx 1.6$, the pion propagator will decay so quickly on the lattice that it will hardly *feel* any gauge links and will therefore not be stongly influenced by the gauge sector. The β-independence at large m and the scaling behaviour (i.e. B decreases as β increases) at small m, cause one to expect an increase in curvature of the PCAC slope as one increases β. This can be seen by comparing Figures 2.5 and 2.6.

2.3.3 Rho meson

Mass	Beta			
m	5.70	6.00	6.15	6.30
0.50	1.930(9)	1.806(60)	1.796(11)	1.789(20)
0.16	1.558(3)	1.104(37)	0.996(22)	0.969(8)
0.09	1.471(27)	0.862(54)	0.744(13)	0.715(10)
0.04	1.242(75)	0.648(65)	0.529(7)	0.491(26)
0.01	1.055(7)	0.352(82)	0.334(119)	0.337(46)
0.00	0.999	0.363	0.307	0.294

Table 2.4: Rho-meson masses M_ρ.

Table 2.4 shows the minimum values of M_ρ obtained from the $(1,1)$ and $(2,1)$ fits to the PV and VT channels. The $m = 0.00$ row is M_ρ extrapolated to zero mass, obtained by fitting the M_ρ to the expression $\sinh M_\rho = Cm + D$; the errors are estimated at around 10%. Figure 2.7 displays these results.

2.3.4 Nucleon

Table 2.5 shows the $(1,1)$ mass-fits to the nucleon mass M_N; the upper figures are from the ALL operator and the lower figures are from the EVEN operator. As Figure 2.8 shows, the nucleon signal is noisy and it is this that leads to the

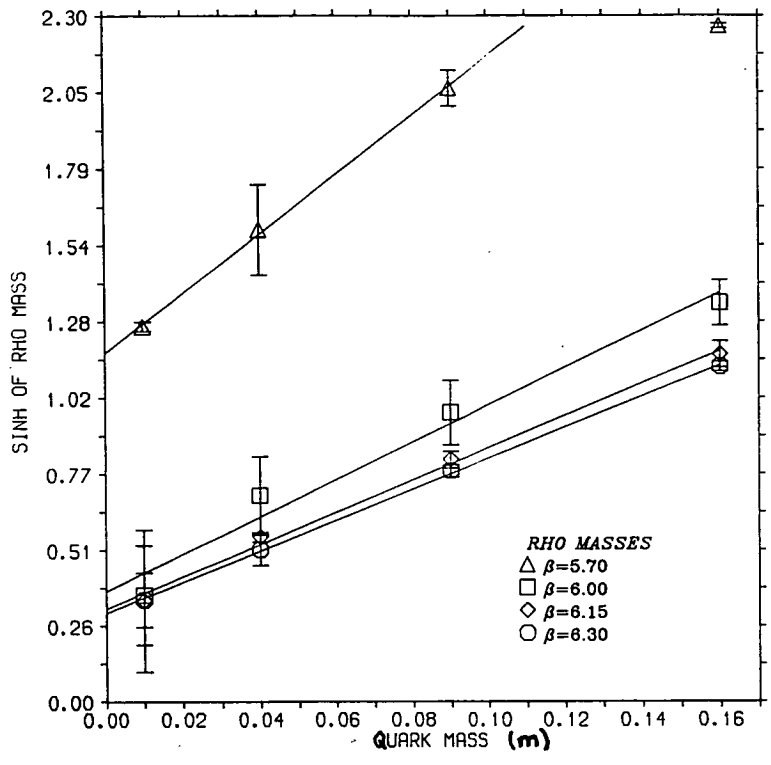

Figure 2.7: Rho-Meson Masses.

large errors on the quoted masses. In order to obtain more accurate masses, (2,1) and (2,2) fits were performed to the nucleons as described in the last section.

It appears that the ALL and EVEN local operators project a weak and noisy nucleon signal. The $\beta = 6.15$ results appear to be the least noisy and it is perhaps no coincidence that only at $\beta = 6.15$ did we use periodic spatial boundary conditions for the quarks. On lattices with antiperiodic spatial boundaries, momentum values can only be $\pi/N, 3\pi/N, \ldots, 2\pi - \pi/N$ whereas with periodic boundaries they can only be $0, 2\pi/N, \ldots, 2\pi - 2\pi/N$. This has the result that in trying to project a zero-momentum state on an antiperiodic lattice will result in projecting states with all the momenta $\pi/N, 3\pi/N, \ldots, 2\pi - \pi/N$:

$$\sum_{x=0}^{N-1} e^{ipx} = 1 - i \cot\left(\frac{p}{2}\right)$$

for antiperiodic $p = \pi/N, 3\pi/N, \ldots, 2\pi - \pi/N$. It is no wonder that we found

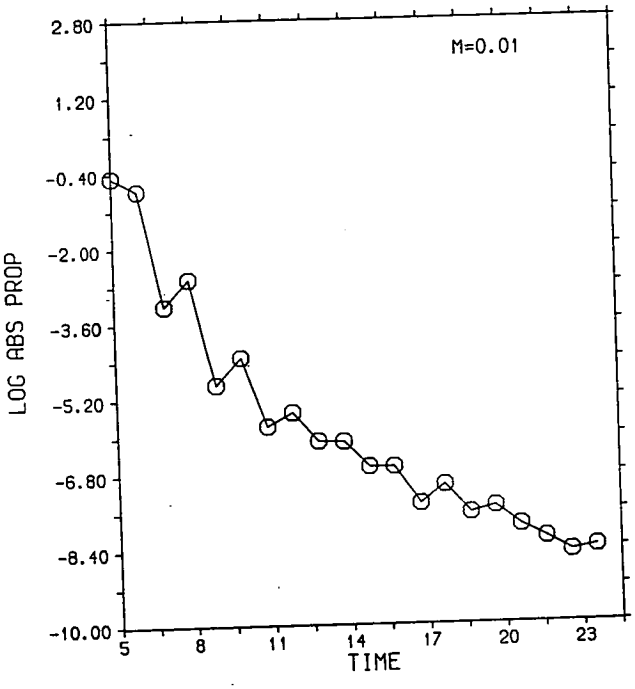

Figure 2.8: ALL propagator at $\beta = 6.30$.

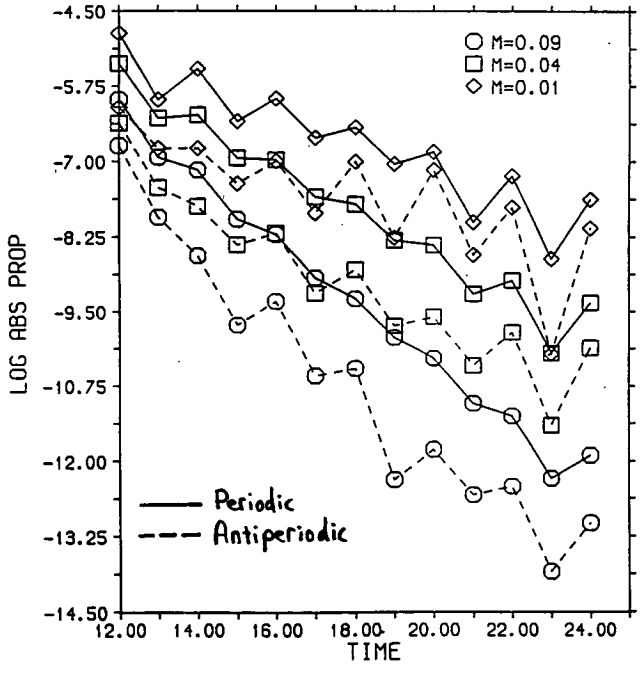

Figure 2.9: EVEN propagators at $\beta = 6.15$.

Mass	Beta			
m	5.70	6.00	6.15	6.30
0.50	3.042(44)	2.909(11)	2.797(12)	2.909(11)
	3.040(11)	2.922(6)	2.807(5)	2.894(11)
0.16	2.703(70)	2.174(143)	1.654(13)	2.072(41)
	2.550(165)	2.168(41)	1.635(11)	2.041(118)
0.09	2.627(104)	1.797(209)	1.248(9)	1.708(143)
	2.543(263)	1.727(93)	1.230(6)	1.735(193)
0.04	2.368(274)	1.055(146)	0.864(23)	1.304(99)
	2.448(4)	1.314(152)	0.863(10)	1.254(206)
0.01	no fit	1.332(255)	0.511(67)	1.099(764)
	2.359(89)	1.418(341)	0.576(19)	1.486(344)

Table 2.5: ALL and EVEN nucleon masses M_N.

noisy signals because we were attempting to measure the propagator for a crowd of nucleons with all values of momentum and this does not give a single mass eigenstate. At large enough times, then only the lowest energy state would persist (presumably the momentum π/N state), unfortunately on a finite lattice we are not allowed the luxury of having large enough times.

Evidence for this explanation can be seen in Figure 2.9 by observing how much noisier the antiperiodic signal is compared to the periodic one. Further evidence for the existence of a superposition of momentum states is provided by the fact that the periodic masses are less than the antiperiodic masses; one expects higher momentum states to be more massive. Mesons do not suffer from these problems because they consist of an even number of quark fields and hence feel only periodic boundary conditions regardless of the boundary conditions on the quark fields.

It has been suggested [4] that the local-in-time to the non-local-in-time nucleon propagator costs no more inversions yet appears to give cleaner signals than the ALL and EVEN propagators [46]. It should be adopted in future work.

[4] In conversation with Greg Kilcup.

In the limit of an infinite number of configurations and on lattices with reflection symmetry, the mean EVEN and ALL propagators should be identical [47]. Our data on a finite number of configurations does not contradict this identity within statistical errors; for example, compare the EVEN and ALL masses in Table 2.5.

2.3.5 Mass Ratios

Mass	M_π/M_ρ	M_N/M_ρ
0.50	0.925(6)	1.589(13)
0.16	0.900(21)	1.606(45)
0.09	0.866(14)	1.610(33)
0.04	0.780(10)	1.595(18)
0.01	0.545(47)	1.508(107)

Table 2.6: Mass ratios at $\beta = 6.15$.

Table 2.6 shows the ratios of hadron masses at $\beta = 6.15$ with periodic boundary conditions. The M_N, M_ρ and M_π are from EVEN (1,1), VT (1,1) and PS (2,0) fits respectively.

Fitting M_N and M_ρ to the form $\sinh M = Cm + D$ and then extrapolating to $m = 0$ gives a value of $M_N/M_\rho = 1.50(9)$.

Figure 2.10 shows a plot of the ratios. Point A is the heavy-quark limit where $M_N = 3m$ and $M_\rho = M_\pi = 2m$ and point B is from the experimental values $M_N = 940\text{MeV}$, $M_\rho = 770\text{MeV}$ and $M_\pi = 140\text{MeV}$. It can be seen that our data is between A and B and is heading towards B at lower quark masses. Even at $m = 0.01$ the M_π/M_ρ ratio is not close to that at point B; lower quark masses are needed in LQCD simulations. In addition to this problem, the ratio M_N/M_ρ has not dropped below the heavy-quark value of 1.50 even when extrapolated to $m = 0$. This problem is present in LQCD calculations performed throughout the world and indicates that we are not simulating in a light-quark regime. Recent calculations with dynamical fermions indicate that it may not be just a problem caused by the quenched approximation [48]. The large error in the ratio M_N/M_ρ

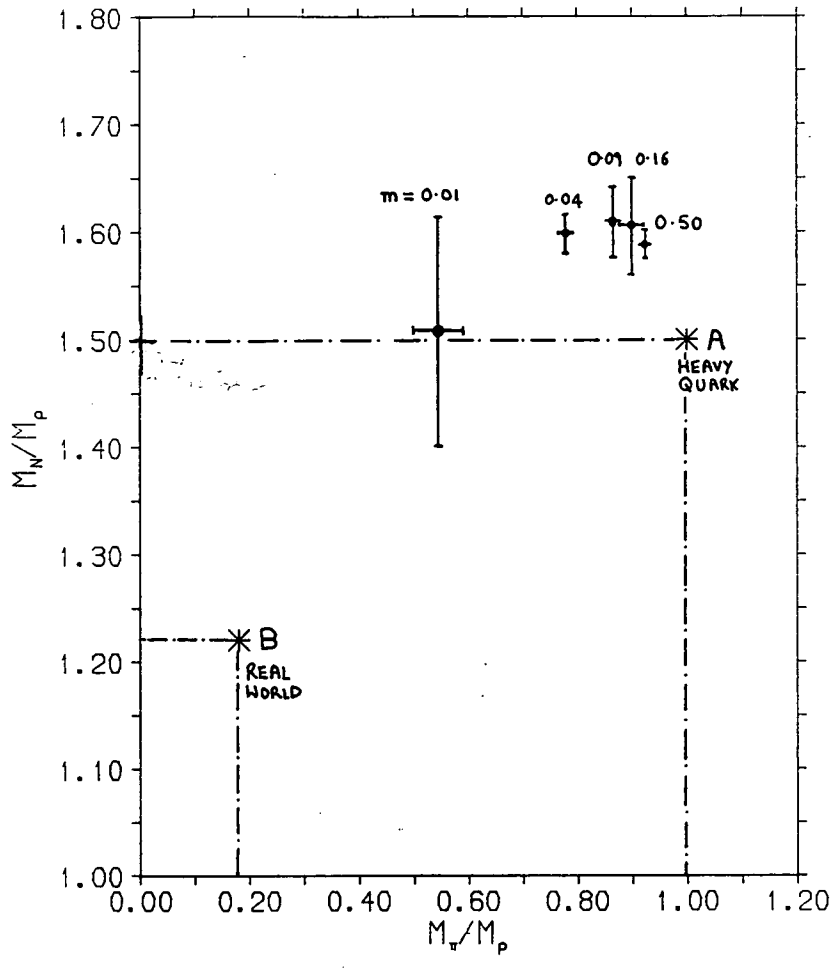

Figure 2.10: The Edinburgh Plot at $\beta = 6.15$.

comes mainly from the error in the values of M_N and hence it is of importance to find a good nucleon propagator.

I omit including ratio results at other β values on the grounds that I do not believe the estimates obtained for M_N, because of the arguments discussed previously and because of the fact that masses greater than about 1.5 are too big to be physically meaningful; the nucleons have masses approaching the scale of the ultra-violet cutoff and hence measure UVFSE rather than physics.

2.3.6 Pion Decay Constant

The pion decay constant f_π is derived from the data by using the relation (2.7) and thus requires knowledge of the chiral condensate $< \overline{\chi}\chi >$. At $m = 0$ the condensate vanishes in finite-volume systems; true SSB requires taking an infinite-volume limit. To find f_π it is necessary to know the condensate at small m and this therefore requires a careful extrapolation. Careless extrapolation would give vanishingly small values of the condensate because of the above-mentioned effect. Instead, one should measure the condensate on larger and larger lattices in order to find the infinite-volume envelope and then one should extrapolate this to the small m [49]. Having only one size of lattice at each β, we have not been able to follow this procedure and therefore our condensate extrapolations may be too small.

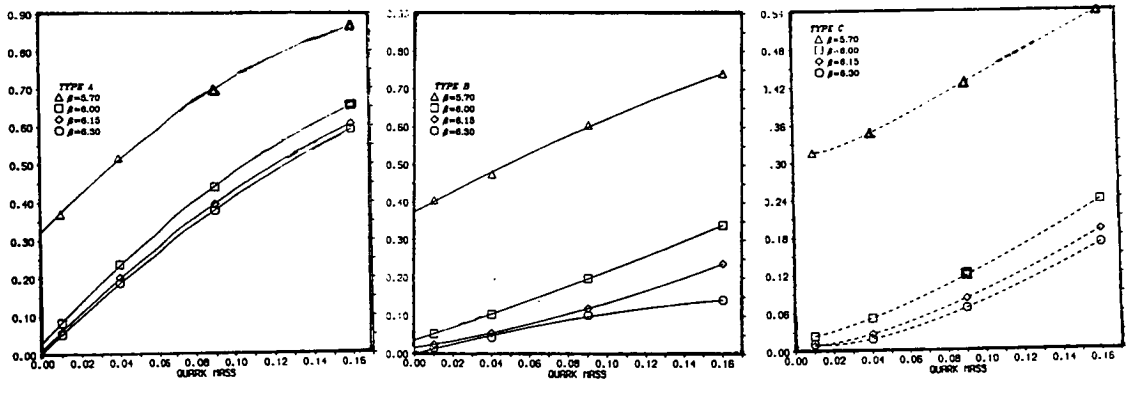

Figure 2.11: Three chiral condensates.

It is convenient to define the three types of condensate A,B and C; these give the results shown in Figure 2.11. The condensates are defined as:

$$< \overline{\chi}\chi >_A = TrG(y,y)$$
$$< \overline{\chi}\chi >_B = \frac{2A_\pi m}{M_\pi}$$

$$< \overline{\chi}\chi >_C \;=\; \left(1 - m\frac{\partial}{\partial m}\right) < \overline{\chi}\chi >$$

Type A is the direct definition obtained by integrating out the fermions in the path-integral. By using WI (2.6), it can be written as $< \overline{\chi}\chi >= \sum_t C_{PS}(t)$ and so it can be extracted from the PS timeslice data. Furthermore, if $C_{PS}(t)$ can be parameterized as $C_{PS}(t) = A_\pi \exp(-M_\pi \mid t \mid)$ then condensate A becomes equal to $2A_\pi m/M_\pi$ which is defined to be condensate B. Condensate C is defined as the extrapolated version of condensate A which, by applying the Ward identities (2.5) and (2.6), can be written as $< \overline{\chi}\chi >= m\sum_t C_{PS}(t) - C_{SC}(t)$ and hence can be easily found from the timeslice PS and SC data. Condensate C is expected to have a constant region for not too small m where its value gives the correct physical condensate. Unfortunately this does not appear to be the case and this suggests that perhaps we should look at smaller m on much bigger lattices. Condensates A and B were fitted to $A + Bm + Cm^2$ over the range $0.01 \leq m \leq 0.16$ (shown as solid lines in Figure 2.11) and gave similar $m = 0$ extrapolations. Extrapolation to $m = 0$ for type B gives the values 0.375, 0.036, 0.016 and 0.000 for β of 5.7, 6.0, 6.15, 6.30; we estimate errors to be of the order of 20%.

Mass	Beta			
m	5.70	6.00	6.15	6.30
0.50	1.616(36)	1.288(8)	1.185(27)	1.142(15)
0.16	2.366(38)	1.033(17)	0.690(13)	0.586(18)
0.09	2.672(42)	0.806(20)	0.455(11)	0.376(18)
0.04	3.264(94)	0.639(29)	0.300(11)	0.243(20)
0.01	5.543(6)	0.651(37)	0.260(13)	0.199(39)

Table 2.7: (1,0) Pion amplitudes A_π.

Taking the condensate as type B gives $f_\pi^2 = m^2 A_\pi / M_\pi^3$. Using the (1,0) data shown in Table 2.7 and the (1,0) data in Table 2.3 and by fixing the physical scale by setting the physical pion mass to 140 MeV, gives the results shown in Table 2.8. These values should be compared to the experimentallly observed value of 93 MeV.

Mass	Beta			
m	5.70	6.00	6.15	6.30
0.16	118 MeV	118 MeV	114 MeV	112 MeV
0.09	109 MeV	115 MeV	112 MeV	109 MeV
0.04	110 MeV	110 MeV	111 MeV	107 MeV
0.01	120 MeV	144 MeV	121 MeV	82 MeV

Table 2.8: f_π from (1,0) fits.

An alternative, and more recent way of finding f_π is by using the relation $f_\pi = \sqrt{<\overline{\chi}\chi>/2B}$ where B is the PCAC slope. This method avoids using A_π, which, because of the exponential nature of the fits, is prone to large error. Using the extrapolated values for condensate B and using the PCAC slopes previously quoted, gives values for f_π of 203(30) MeV, 100(15) MeV and 81(12) MeV at $\beta = 5.7, 6.0$ and 6.15 with the scale set by (2.9).

2.4 Physical Limit

Physical QCD results are only obtained in the infinite-volume continuum limit of LQCD. Are we approaching this limit ? Furthermore, do our results give physical values that agree with the experimentally measured values ? Finally, how can we overcome the UVFSE and IRFSE responsible for systematic errors in LQCD simulations ?

2.4.1 Flavour Symmetry Restoration

As mentioned previously, the $U_1 \otimes U_1$ symmetry enlarges to a $U_4 \otimes U_4$ symmetry as $g \rightarrow 0$ with the result that the spectra for some non-identical operators become degenerate. This is known as Flavour Symmetry Restoration. Figure 2.12 shows how the M^{1+} masses, obtained from fits to the PS and SC propagators, become

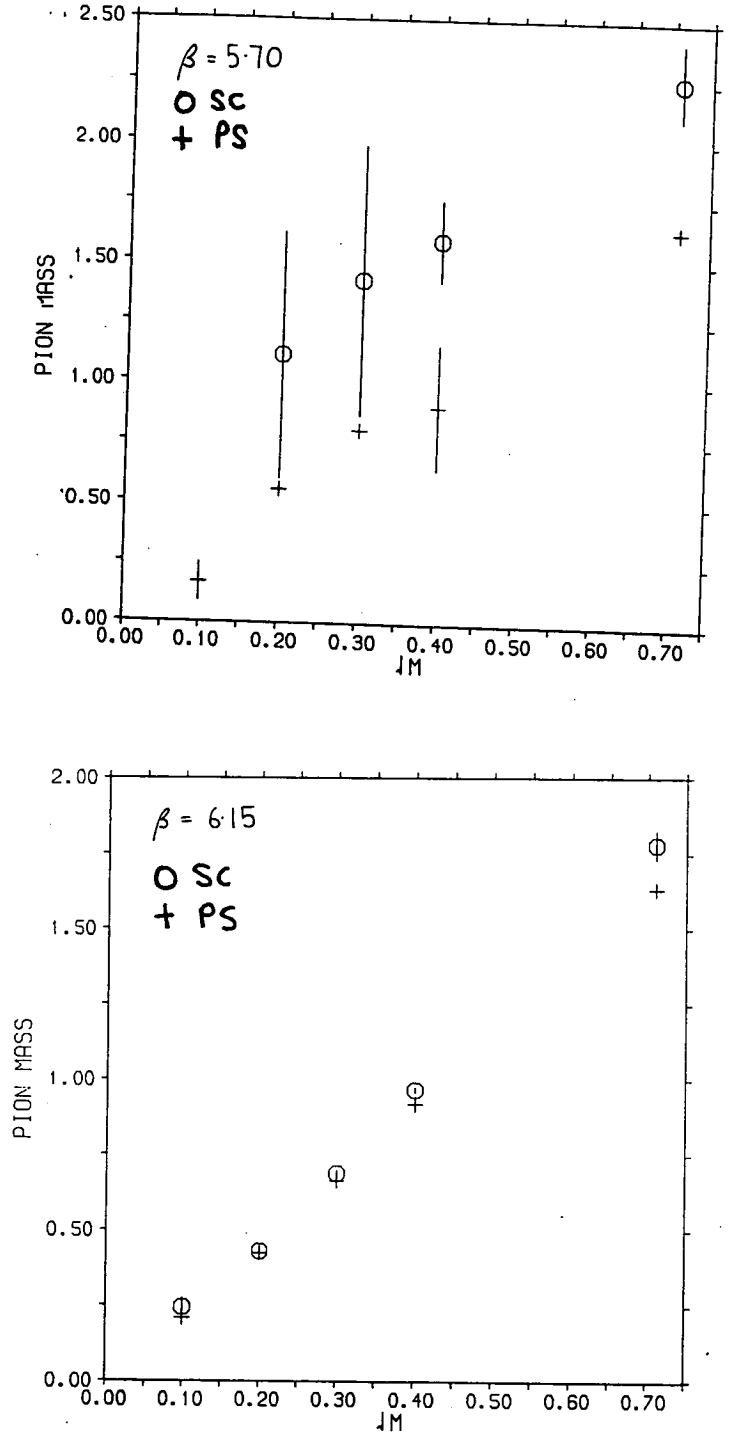

Figure 2.12: PS-SC Flavour Symmetry Restoration.

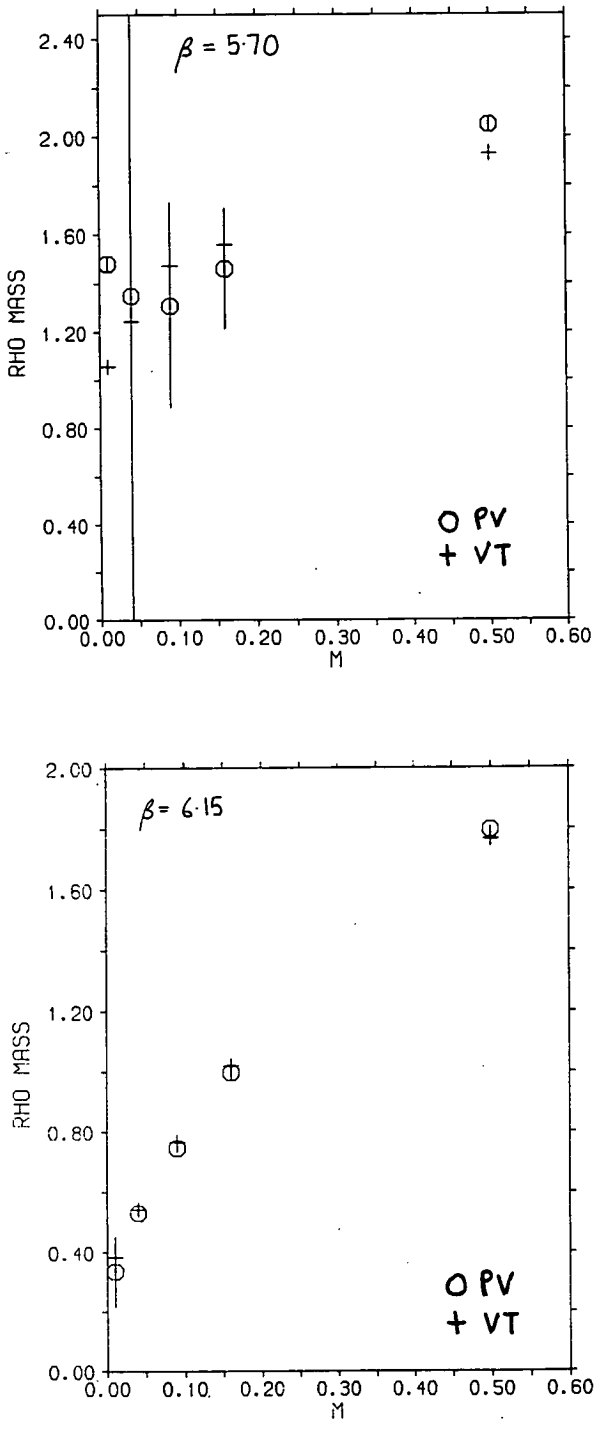

Figure 2.13: PV-VT Flavour Symmetry Restoration.

degenerate as β goes from 5.7 upto 6.15. Figure 2.13 shows the same behaviour in the PV and VT sectors. The results indicate that FSR is starting to occur at $\beta \approx 6.0$. For lower values of β the results are not showing the expected 4-flavour continuum behaviour.

2.4.2 Asymptotic Scaling

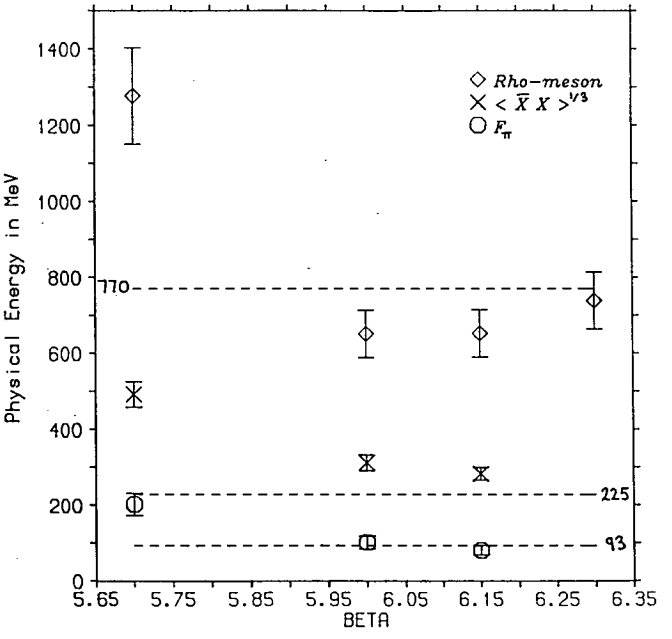

Figure 2.14: Physical Predictions.

Figure 2.14 shows the physical results obtained from the lattice data. The 2-loop lattice spacing a with $\Lambda_{lat} = 4.2$ MeV, has been used to set the physical scale. The dashed lines show the experimentally expected values for these quantities. From this diagram, one could conclude that the lattice is giving predictions that are starting to look physical. Table 2.9 shows the numerical results.

In our range of β, the 2-loop a changes by a factor of ≈ 2. The physical value

Beta	a	Rho Mass	$< \overline{\chi}\chi >^{1/3}$	f_π
5.70	0.154 fm	1280(128) MeV	491(32) MeV	203(30) MeV
6.00	0.110 fm	650(65) MeV	312(21) MeV	100(15) MeV
6.15	0.093 fm	650(65) MeV	280(19) MeV	81(12) MeV
6.30	0.078 fm	743(74) MeV	—	—
Expt.	—	770 MeV	225 MeV	93 MeV

Table 2.9: Physical results.

of the PCAC slope, obtained from B by multiplying by a and by the anomalous dimension factor $\alpha^{4/11}$ where $\alpha = 9/2\pi\beta$ [51], changes from 5.8(6) GeV to 7.2(7) GeV and hence is relatively constant by comparison.

2.4.3 Avoiding FSE

In performing a LQCD simulation at some β value, one has to choose a suitable lattice size and a suitable range of quark masses such that UVFSE and IRFSE do not dominate.

A self-consistent criterion for avoiding IRFSE has been given [50]:

$$m \gg \frac{\pi}{N_t N_s^3 < \overline{\chi}\chi >|_m}$$

This criterion works yet has the disadvantage that it gives only a rough definition of the value of m where IRFSE become important.

Rather than considering m, consider instead M_π. This is the inverse of a correlation length ξ_π rather than a bare-parameter in the action, and hence can be compared with lattice sizes to find the regions of UVFSE and IRFSE. When $\xi_\pi \leq 1$, the pion propagator will diminish by at least a factor of e^{-1} per lattice spacing and hence will be very sensitive to the discreteness of the lattice; $\xi_\pi = 1$ will be taken as the minimum value of ξ_π before UVFSE become important. When $\xi_\pi \geq N$, the pion propagator will diminish less than e^{-1} in going from

one side of the lattice to the other side and hence will know about being in a finite volume; $\xi_\pi = N$ will be taken as the maximum value of ξ_π before IRFSE become important. To convert these constraints on M_π into constraints on m we will make use of the PCAC relation $M_\pi^2 = Bm$ together with the fact that physical B is approximately 7 GeV. These give the following criteria:

$$\begin{aligned} m_- &= 0.0059\alpha^{4/11}(\Lambda_{lat}a)^{-1}N^{-2} \\ m_0 &= 0.66\alpha^{4/11}(\Lambda_{lat}a) \\ m_+ &= 0.00061\alpha^{4/11}(\Lambda_{lat}a)^{-1} \end{aligned}$$

IRFSE occur when $m \leq m_-$, UVFSE occur when $m \geq m_+$ and the optimal $m = m_0$ gives physical pion masses of 770 MeV; the IRFSE bound was checked by using the results of the very low mass runs at $\beta = 6.15$ and 6.30. Ideally, simulations should run at $m = m_0$ with lattices large enough that $m_- \leq m \leq m_+$ for QCD to be simulated with negligible finite-size effects.

For free fermion propagation at $\beta = \infty$, the pion mass can be calculated analytically to be $M_\pi = 2\sinh^{-1}m$. Applying the above FSE criteria on M_π one then obtains $m_- \approx 1/2N$ and $m_+ \approx 1/2$; these are not what one expects from the above expressions for m_- and m_+. The reason that the criteria fail at very large β comes about from the increasing curvature in the PCAC slope with increasing β. We expect the $\beta = \infty$ results to be upper bounds on m_+ and m_- and expect the above criteria to be valid until these bounds are reached.

Figure 2.15 shows the criteria for $N = 24$ and also shows crosses where we ran simulations. Requesting that $m = m_0 = m_-$ requires that $N = 56$ at $\beta = 6.3$; this is the smallest lattice that can be used at this beta if one does not wish to have to extrapolate data to small m and if one does not wish to have IRFSE.

2.5 Conclusions

The work can be concluded as follows:

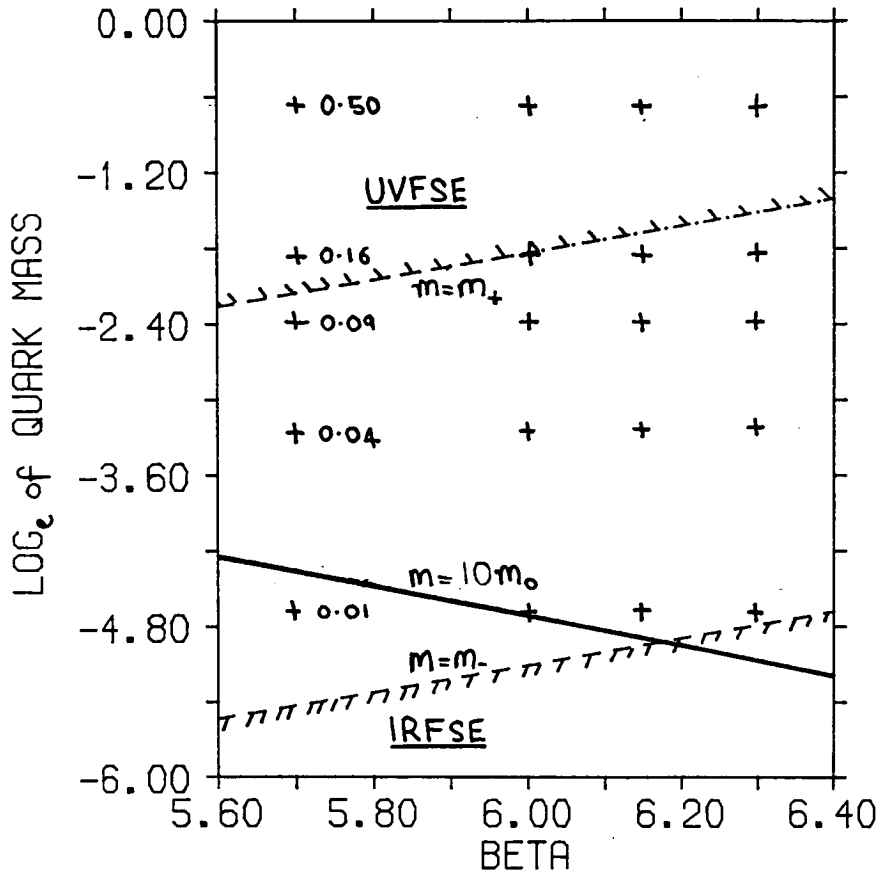

Figure 2.15: Criteria for FSE.

- The results look qualitatively correct. The mass-spectrum is in the correct order $M_\pi < M_\rho < M_N$. The SSB looks to be behaving well i.e. the PCAC relation holds, there exists a non-zero condensate, and f_π is at the correct scale. Flavour Symmetry Restoration is occurring for $\beta \geq 6$.

- Quantitatively the mass-ratios appear to be close to the heavy-quark regime. Simulations with smaller m are required with possibly the inclusion of dynamical fermions.

- Smaller m require the use of larger lattices and therefore necessitate the use of computers with large amounts of memory.

- Asymptotic scaling looks to be starting but runs at larger β are necessary to confirm this.

- The use of lower m and larger β will cause simulations to run much slower because of critical slowing down. MCRG techniques, more efficient algorithms and faster computers will have to be used.

Chapter 3

Yukawa Interactions.

I fellowed sleep who kissed me in the brain,
Let fall the tear of time; the sleeper's eye,
Shifting to light, turned on me like a moon.
So, planing-heeled, I flew along my man
And dropped on dreaming and the upward sky.
D. Thomas

The ElectroWeak (EW) model was proposed by [52,53,54] as a theory capable of describing the weak and electromagnetic forces. It became a serious candidate when it had been proved to be a renormalisable theory [55,56]. The low-energy limit of the EW model is the Fermi theory of weak interactions [57,58] which describes β-decay.

The 3-generation EW model has been very successful in predicting the existence of the charmed quark, in predicting the existence of the massive W and Z vector bosons and in describing lepton-lepton scattering. All the particles expected in the 3-generation EW model have been observed experimentally except for two. The EW model predicts the existence of a Higgs boson and the existence of the top quark. Neither of these particles have been observed yet and therefore their future observation will provide a crucial test of the EW model. Both the SSC and the LEP2 projects are attempting to search for these particles.

Masses and mixing-angles in the 3-generation EW model are determined by

17 parameters which are presumed to be the consequences of a unified theory acting at much smaller distance scales. How the model behaves for differing values of the bare couplings is not well understood beyond perturbation theory. Understanding of this can lead to relationships between observable quantities. For example, recent studies of Gauge-Higgs (GH) models predict that either the Higgs mass is less than 8.5 ± 0.3 times the mass of the W boson or that, if it is larger than this, new physics will occur [59,60,61]. Such predictions define regions of experimental interest and are therefore of value to experimentalists.

On a more fundamental note, the EW model is poorly understood and therefore deserves theoretical study. The origin of the *phenomenological* $\lambda\phi^4$ term, the ad hoc nature of the Yukawa couplings and the number of generations, are all questions that need answering. To answer such questions, two approaches are possible. One can develop more fundamental models such as GUTS, SUSY GUTS and string models in the hope that these will explain the EW model. Alternatively, one can attempt to understand the EW model by studying its dynamics; maybe the dynamics constrain the model to behave only in certain ways. A thorough study of this requires knowledge of the behaviour of the EW model for all values of bare couplings and not just a perturbative understanding in the region of small couplings. Such non-perturbative studies necessitate the use of lattice techniques.

In this chapter, I will present a preliminary study of a toy model that hopefully catches some of the features of the Fermion-Higgs sector of the EW model. The chapter is structured as follows:

- **Motivation** Reasons for studying Fermion-Higgs (FH) systems.
- **Toy Model** A description of our toy model.
- **Method** How we studied the model.
- **Results** The results that the model produced.
- **Conclusions** and extended models which should be investigated.
- **Speculations** A few open questions.

Only recently, have people been investigating Yukawa-coupled FH systems using lattice techniques [62,63,64,65]; in what follows I wish to convey some of the excitement that can be found in what is becoming an active field.

3.1 Motivation

Why should we study Yukawa-coupled FH systems ?

3.1.1 Effective Potential

In 1973, the effective potential formalism was developed for studying actions involving Higgs particles [66]. Consider the general action that describes a Fermion-Gauge-Higgs (FGH) system having a Lagrangian given by:

$$\mathcal{L} = -\frac{1}{2}(D_\mu\phi)^2 - \frac{m^2}{2}\phi^2 + \frac{\lambda}{4!}\phi^4 + \overline{\psi}\not{D}\psi + y\overline{\psi}M\psi + \frac{1}{g^2}F_{\mu\nu}F^{\mu\nu}$$

D denotes the covariant derivative $\partial + igA$. M is a generic Yukawa interaction and is a Hermitian matrix of the form $M = A + i\gamma_5 B$ where A and B are linear functions of ϕ. The gauge fields A and the fermions ψ and $\overline{\psi}$ can be integrated out to leave an *effective action* $\Gamma[\phi]$ that depends solely on the Higgs fields ϕ:

$$\exp(i\Gamma[\phi] + i\int_x J\phi) = \int d[A,\psi,\phi]\exp(i\mathcal{S} + i\int_x J\phi)$$

The effective action can be written as a momentum expansion about the space-time independent background field ϕ_0:

$$\Gamma[\phi] = -V_{eff}(\phi_0) + \int d^4x \frac{1}{2}(\partial_\mu\phi)^2 Z(\phi_0) + \ldots \tag{3.1}$$

V_{eff} is known as the *effective potential* and is obtained by an expansion in terms of n-loop Feynman diagrams. The minima of V_{eff} are believed to give the vacuum states of the theory. The 1-loop contribution to V_{eff} comes from diagrams such as those shown in Figure 3.1.

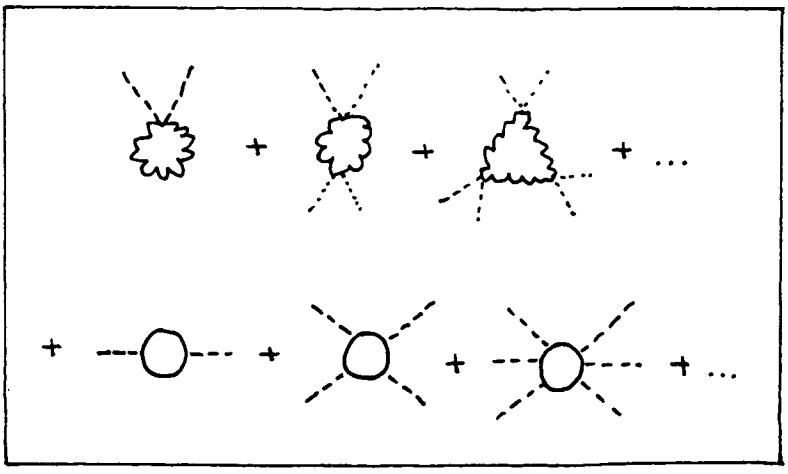

Figure 3.1: 1-loop contributions to $V_{eff}(\phi_0)$.

These can be summed into the following closed form [66]:

$$\begin{aligned} V_{eff}(\phi_0) &= \frac{m^2}{2}\phi^2 + \frac{\lambda}{4!}\phi^4 \\ &+ \frac{1}{64\pi^2}\left[(m^2 + \frac{\lambda}{2}\phi^2)^2 \log(1 + \frac{\lambda\phi^2}{2m^2}) + \frac{\lambda}{2}m^2\phi^2 - \frac{3\lambda^2}{8}\phi^4\right] \\ &- \frac{1}{64\pi^2}\mathrm{Tr}\left[(y^2 m m^\dagger)^2 \log(y^2 m m^\dagger)\right] \end{aligned} \tag{3.2}$$

This gives the *Mexican hat potentials* [1] shown in Figure 3.2.

This is what is known perturbatively about FGH systems and it is used to place upper-bounds on the mass of the top quark by requiring that V_{eff} be bounded from below. For measured fermion masses, the Yukawa part of Eqn. (3.2) is small; this is used as an argument that the effect of Yukawa couplings need only be considered for very massive fermions. What is not known, however, is the range of m, λ, g and y over which this technique works. Furthermore, there is very little understanding of the $Z(\phi_0)$ term and higher terms in the momentum expansion; they are basically neglected. Doubts such as these can only be answered by doing non-perturbative calculations involving sums over all the Feynman diagrams; to do this we require lattice techniques.

3.1.2 Triviality

The running-coupling constant λ, in pure $\lambda\phi^4$ theories and in GH theories, increases at increasing momentum scale. The renormalised λ defines the ratio of

[1] Sometimes bibulously referred to as wine bottle potentials.

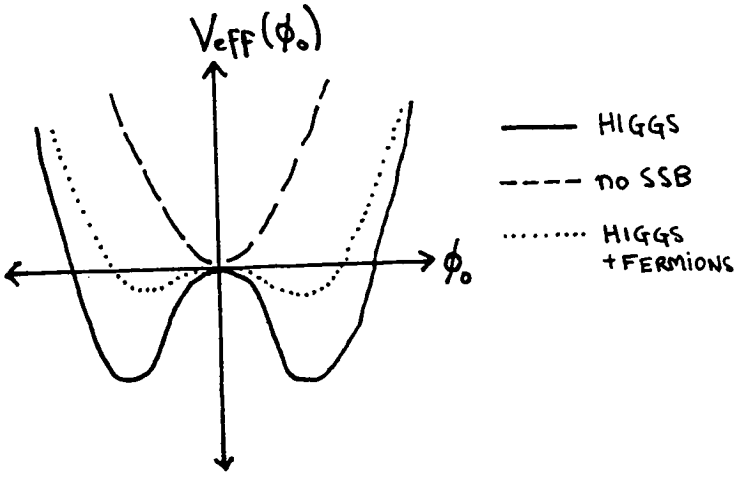

Figure 3.2: The Effective Potential.

the Higgs mass to the W-boson mass: $M_H/M_W \propto \sqrt{\lambda}$. As the momentum scale is increased, in a theory with a finite UV cut-off Λ, there will thus come a point when $M_H = \Lambda$. If the Higgs mass is above this scale, then it becomes no longer sensible to use the theory; the theory must be viewed as being only a low-energy effective theory [67]. This is the current view of the electroweak model.

This can be viewed another way by seeing that these theories become *trivial* when $\Lambda \rightarrow \infty$ and therefore, for them to be meaningful, they have to be viewed as effective theories with finite Λ [68]. *Trivial* theories are ones where the renormalised couplings vanish as the cut-off is removed.

The most compelling evidence for the effective nature of the EW model comes from the work of [59,60,61]. A simulation of an $O(4)$ ϕ^4 model was performed on a 12^4 lattice, with both the Higgs mass M_H and the Higgs VEV v been measured over a wide range of K and λ values. The ratio $R = M_H/v$ is shown in Figure 3.3 [2]. For any M_H value, R is bounded from above by the $\lambda = \infty$ result with the largest bound occuring when M_H is the largest. With the caveat

[2]With kind permission from Anna Hasenfratz

that the largest meaningful M_H is when $M_H = \Lambda$, one obtains the inequality $M_H/v \leq 2.7 \pm 0.1$; for larger M_H one expects to see *new physics*. Treating the gauge interaction perturbatively, one can find v in terms of the W boson mass M_W; $M_W^2 = g^2v^2/4$. Taking $g^2 = 0.4$, one obtains the bound $M_H/M_W \leq 8.5(3)$.

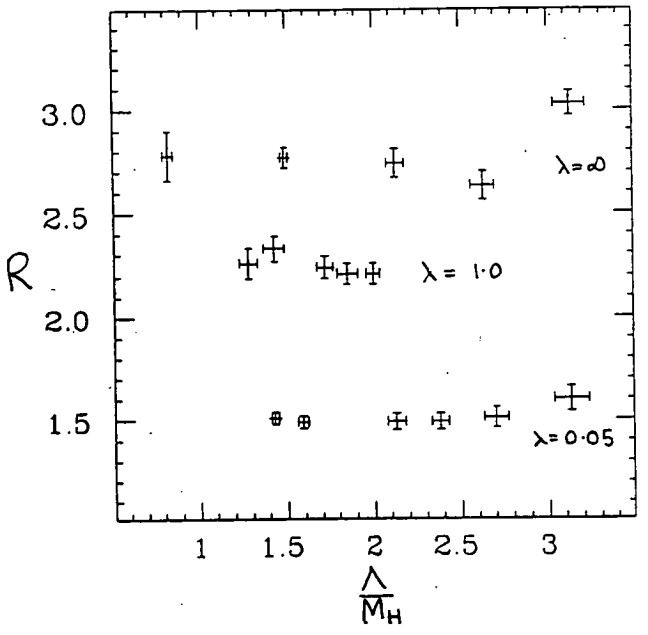

Figure 3.3: M_H/v ratios.

These arguments appear to work for ϕ^4 models and Gauge-Higgs models but do they work for Fermion-Gauge-Higgs models ? Might not the fermions rescue the model from triviality ? Even if triviality persists, the fermions may have a large effect on the mass bound of M_H/M_W and so should be included.

3.1.3 Fermion Doubling

In attempting to study fermions using lattices, one always has the problem of fermion doubling; transcription of the continuum Dirac operator into a discretized Dirac operator leads to more than one pole in the fermion propagator.

In *vector* theories, such as QCD, where the right and left components of the

fermion transform as the same representation of the gauge group, there are two ways commonly used to get rid of the extra poles. One can add the Wilson term $r\overline{\psi}D^2\psi$ which breaks chiral symmetry, becomes irrelevent in the continuum limit and gives the doubled species masses $O(r/a)$ where a is the lattice spacing. Or one can use the staggered formulation which diagonalizes M_{xy} [69] and projects out only one-quarter of the remaining fermions, thus leaving 4 poles which are intepreted as 4 degenerate flavours of fermions.

In *chiral* theories, such as the EW model, the right and left components transform as different representations of the gauge group and getting rid of doubles becomes a major problem. The Wilson term, if used in a chiral theory, explicitly breaks chiral symmetry which in turn explicitly breaks gauge symmetry. The Slavnov-Taylor identities will then no longer be valid and the renormalisability of the model becomes an open question; this is not a desirable feature of a theory. The staggered formulation also cannot be used for chiral theories because the Kawamoto-Smit projection no longer works on the gauged part of the derivative; the $\gamma_5\gamma_\mu A_\mu$ diagonalizes to a γ_5 matrix rather than to the required unit matrix.

Jan Smit has proposed a way that might work in decoupling the doubles in a chiral fermion gauge theory [70,71]. It amounts to adding *Yukawa* and *Yukawa-Wilson* terms to the naive fermionic action:

$$S \;\rightarrow\; S + Y\sum_x \overline{\psi}(x)\phi(x)\psi(x) + Y_W\sum_{x,y}\overline{\psi}(x)\phi(x)D^2\psi(y)$$

The ϕ is a Higgs field transforming as the adjoint of the gauge group and is intended to have a VEV that gives the fermion species mass in a chirally-invariant way. By varying the Yukawa Y and Yukawa-Wilson Y_W couplings it is hoped that one could be left with a low Higgs VEV, a low-mass single species of fermion and infinite-mass decoupled doubles [72].

To be able to implement this procedure it is necessary to understand how non-perturbative Yukawa couplings behave and in particular how large Y and Y_W feed back onto the Higgs sector; if at large Y the VEV vanishes, then the procedure could be destined to fail.

3.2 Toy Model

Having discussed the lofty motivation for studying FH systems, I will now describe the toy model that we studied. Even though there are no gauge fields in our model, I will use the language of Gauge-Higgs models; for example, strictly speaking, *coulomb phase* should be referred to as *symmetric phase.*

3.2.1 Action

Hybrid Monte-Carlo techniques [74] were used to simulate the action for a 2-component radially-fixed ϕ^4 model interacting with two species of naive fermions:

$$\begin{aligned} S &= -K\sum_{x,\hat{\mu}}\left(\phi_x^\dagger\phi_{x+\hat{\mu}}+\phi_x^\dagger\phi_{x-\hat{\mu}}\right) \\ &\quad +\sum_{x,y}\left(\overline{\psi}_x^{(1)}M_{xy}\psi_y^{(1)}+\overline{\psi}_x^{(2)}M_{xy}^\dagger\psi_y^{(2)}\right) \end{aligned} \tag{3.3}$$

with the fermion matrix M_{xy} defined as

$$\begin{aligned} M_{xy} &= \frac{Y}{2}\left(\phi_x\delta_{xy}(1+\gamma_5)+\phi_x^\dagger\delta_{xy}(1-\gamma_5)\right) \\ &\quad +\frac{1}{2}\sum_\mu\gamma_\mu(\delta_{y,x+\hat{\mu}}-\delta_{y,x-\hat{\mu}}) \end{aligned} \tag{3.4}$$

Both M and $M^\dagger$ were included in the action because of the possibility that $\det M$ may be complex.

Rather than use the radially non-fixed model containing a $\lambda(\phi^\dagger\phi-1)^2+\phi^\dagger\phi$ term, we have specialised to the $\lambda=\infty$ case where $\phi_x=e^{i\theta_x}$ and $\phi_x^\dagger=e^{-i\theta_x}$.

The model contains two bare-parameters: K the *hopping parameter* and Y the *Yukawa coupling.* We were interested in finding the phase-diagram in (K,Y) space. No gauge fields are included and no Yukawa-Wilson term has been added.

3.2.2 Symmetries

The action in (3.3), posesses the global continuous symmetry $SU(2)_V \otimes U(1)_V \otimes U(1)_A$.

The $SU(2)_V$ symmetry arises from the unitary transformations which mix the L and R components of fermion 1 into the R and L components of fermion 2. It is a relabelling symmetry which does not involve the Higgs fields.

The $U(1)_V$ symmetry is the usual number conservation symmetry for fermions:

$$\begin{aligned} \psi &\rightarrow e^{i\theta}\psi \\ \overline{\psi} &\rightarrow \overline{\psi}e^{-i\theta} \end{aligned}$$

where θ is the global phase angle.

The $U(1)_A$ symmetry is an axial symmetry involving the Higgs fields:

$$\begin{aligned} \phi &\rightarrow e^{-2i\alpha}\phi \\ \phi^\dagger &\rightarrow \phi^\dagger e^{+2i\alpha} \\ \psi^{(1)} &\rightarrow e^{i\alpha\gamma_5}\psi^{(1)} \\ \overline{\psi}^{(1)} &\rightarrow \overline{\psi}^{(1)}e^{i\alpha\gamma_5} \\ \psi^{(2)} &\rightarrow e^{-i\alpha\gamma_5}\psi^{(2)} \\ \overline{\psi}^{(2)} &\rightarrow \overline{\psi}^{(2)}e^{-i\alpha\gamma_5} \end{aligned} \tag{3.5}$$

The Higgs part has the symmetry of a 4-dimensional $O(2)$ spin-system and therefore the Higgs fields may have aligned, disordered or anti-aligned phases. In the ordered phases, the symmetry is spontaneously broken and hence in these phases there is spontaneously broken chiral symmetry. Spontaneous breaking of chiral symmetry can lead to mass generation for the fermions.

3.2.3 Observables

To look at the phase diagram, we took expectation values of the three observables:

$$\begin{aligned} P &= \frac{1}{N}\mathrm{Tr}(MM^{\dagger})^{-1} \\ Q &= \frac{1}{2} + \frac{1}{8N}\sum_{x,\mu}\cos(\theta_{x+\hat{\mu}} - \theta_x) \\ R^2 &= \frac{1}{N^2}\left(\sum_x \cos\theta_x\right)^2 + \frac{1}{N^2}\left(\sum_x \sin\theta_x\right)^2 \end{aligned} \tag{3.6}$$

The total number of lattice sites is denoted by N.

Q and R^2 are measures of the alignment of the angles θ_x and range over [0,1]. For perfectly aligned, disordered and anti-aligned phases, Q is 1.0, 0.5 and 0.0 and it has been used in previous simulations [73]; it corresponds to the scalar part of the action S. R^2 was used as an alternative to Q and takes the value of 1.0 for perfectly aligned phases and 0.0 for perfectly disordered and anti-aligned phases; it is the squared length of the vector sum of the $O(2)$ spins.

P was used to examine the fermion sector. It was chosen instead of the condensate $\mathrm{Tr}M$, because it has the advantage of being a real rather than a complex quantity.

In addition to these observables, we looked at the expectation of

$$CV = 16N(Q - < Q >)^2$$

where $< \ldots >$ means the expectation over the ensemble of configurations. CV is a specific heat for the Higgs fields and was useful in looking at phase transitions.

3.3 Method

The method was as follows:

1. Generate a configuration, at some (K, Y) value, with probability $\propto \exp(-\mathcal{S})$ using the Hybrid Monte-Carlo (HMC) algorithm.

2. Measure the observables P, Q, R^2 and Q^2 on this configuration.

3. Repeat steps **1** and **2** roughly 2000 times.

4. Average the observables over the configurations in order to find the expectation values $< P >, < Q >, < R^2 >$ and $< CV >$.

5. Perform steps **1-4** over a whole range of (K, Y) values in parallel.

6. Observe the variations in the expectations over the range of (K, Y).

3.3.1 Algorithm

The algorithm used to generate the configurations was Hybrid Monte-Carlo [74]. The fermions are replaced by bosonic pseudo-fermions χ having the pseudo-fermionic action S_{PF} defined as the bosonic part of $\mathcal{S}$ in Eqn. (3.3) plus the pseudo-fermionic part $\chi^\dagger (M^\dagger M)^{-1} \chi$. The algorithm is as follows:

1. **Initialisation** Make pseudo-fermions χ by multiplying gaussian noise by $M^\dagger$. Find $x = (M^\dagger M)^{-1}\chi$, used in S_{PF}, by least-norms conjugate gradient [75]. Measure observable $P = \|x\|^2$. Generate Higgs momenta π from gaussian noise. Calculate the old Hamiltonian $H_{old} = \pi^2 + S_{PF}$.

2. **Molecular Dynamics** Evolve the Higgs system through phase-space deterministically by using the equations of motion from the Hamiltonian $H_{PF} = \pi^2 + S_{PF}$. Use the leapfrog method to time step $\delta\tau$ upto a total time τ. Hold χ constant and update $x = (M^\dagger M)^{-1}\chi$ each timestep by using a conjugate gradient algorithm.

3. **Accept/Reject test** Measure and record the new observables. Calculate the new Hamiltonian and compare it with the old one; accept the new ϕ fields with probability $\min(1, \exp(H_{new} - H_{old}))$.

The fermion inversions were performed by the CG algorithm described in Chapter 1. The CG algorithm was terminated whenever the number of iterations reached 1000 or whenever the residual $\varepsilon = r^\dagger r/N$ dropped below a preset tolerance. The absolute error (i.e. ε calculated exactly from $r = b - Ax$) was then calculated and checked against the preset tolerance. If it was larger than the tolerance, the algorithm was restarted, otherwise the algorithm terminated. The preset tolerance was found by requiring constant results; as the tolerance is decreased there comes a point where the results become independent of the tolerance. Typically the tolerance that was used was about 10^{-12}. For each CG inversion in the molecular dynamics steps, the initial guess x was chosen by a predictor method using the x calculated in the previous steps. The order of the predictor could be varied and on each run was chosen to be optimal.

Periodic boundaries in all directions were used for the Higgs fields. For the pseudo-fermions, periodic boundaries were all also tried but it was found that periodic-in-space antiperiodic-in-time boundaries enabled fermion inversions to be performed in the region of small Y [3] and hence these were adopted for all the runs.

3.3.2 Implementation

The algorithm was implemented in OCCAM2 on a *Computing Surface* made of 103 T800 floating point transputer chips. Refer to Appendix B for hardware details. Identical copies of the algorithm were placed on 102 of the transputers and the 103rd transputer was used as a controller/data-logger. The transputers were connected as shown in Figure 3.4; we were using an OCCAM2 farm with asynchronous eggs. A calculating speed of roughly 100 Mflops was achieved.

[3] in this regime there appears to be a zero-mode !

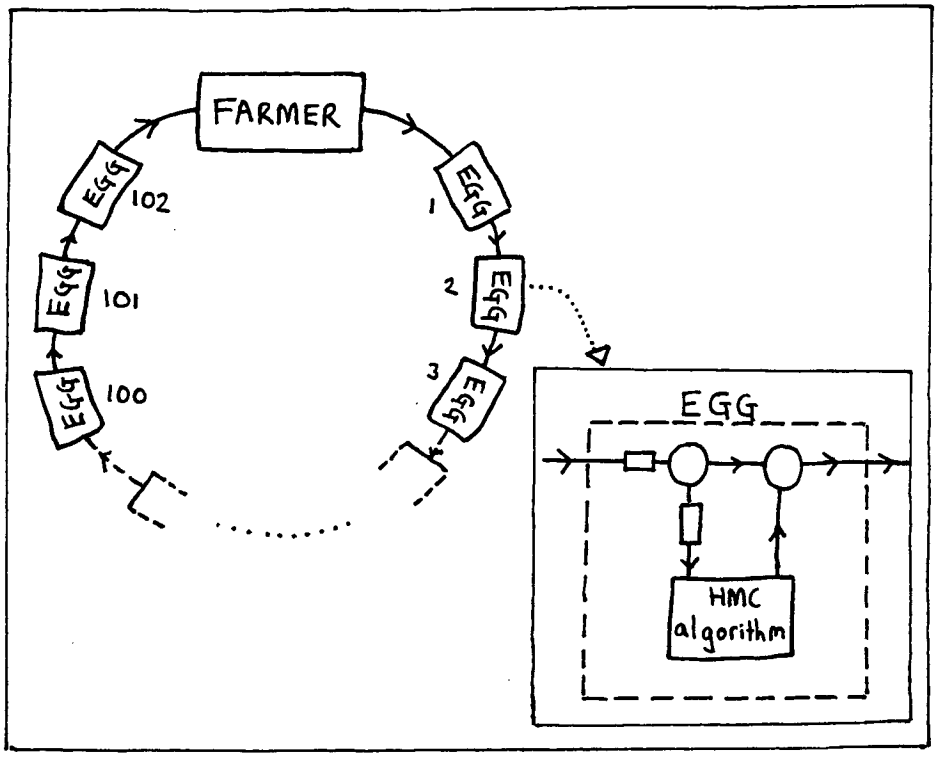

Figure 3.4: The Egg Farm.

3.3.3 Checks

In any lattice calculation, it is of utmost importance to check that the algorithm has been implemented correctly. This was even more imperative in our case because of the exploratory nature of our model. The checks that we performed were as follows:

1. **Symmetries of the Action** The action S_{PF} should be real and should be invariant under $U(1)_A$ transformations of the ϕ and χ. It was verified to be so up to 8 significant figures.

2. **Constant Hamiltonian** In the limit of $\delta\tau \to 0$ the Hamiltonian H in the molecular dynamics steps should be a constant of the motion. This was found to be happening.

3. **Insensitivity to $\delta\tau$ and τ** HMC is designed to give expectations and variances that are independent of the molecular dynamics parameters $\delta\tau$ and τ. Over a range of $0.5 \leq \tau \leq 2$ and $0.01 \leq \delta\tau \leq 0.5$ this was found to be so.

4. **$1/Y^2$ expansions** As shown in Appendix C, the fermionic determinant can be expanded in powers of $1/Y^2$. For $K = 0$, this predicts that at large Y, the expectation of Q should be $< Q >= 0.5 + 0.5Y^{-2}$. This was verified by using Y ranging from 5 up to 12.

5. **One-loop Y expansions** The fermionic determinant can be expanded in powers of Y as shown in Appendix C. The sums I_1, I_2, I_3 are infra-red divergent and therefore diverge on lattices where zero-momentum can occur. Hence, with periodic boundaries, it is necessary to add a mass term $m\overline{\psi}\psi$ to the action in order to be able to check the simulation against computer generated I_1, I_2, I_3 results. This was done for $K = 0$ and $0.1 \leq m \leq 1.0$ and it was found that values of $< Q >$ agreed for Y less than about 0.1. For the periodic in space but antiperiodic in time boundaries, no infra-red regulator is required in calculating the analytic expression. Results agreed for $K = 0$ and $Y < 0.1$.

6. **$d = 4$ XY model** For $Y = 0$ the model becomes a $d = 4$ XY model with non-interacting free fermions and hence the Higgs results can be checked against the known results for the $d = 4$ XY model [73,76]. As K increases this model goes from a Coulomb phase to a Higgs phase with a 2nd order transition at $K = 0.15(1)$. Our results agreed with this behaviour.

3.4 Results

Each of the runs went as follows. First, the algorithm ran for 100 HMC iterations with $\tau = 0.5$ and $\delta\tau = 0.1$ in order to allow the system to equilibrate with its value of (K,Y). From then on, τ was set to 1.0. The next 72 iterations were used for *autotuning*; the order for the inversion predictor and $\delta\tau$ were chosen so as to give the maximum *rate*. *Rate* is defined as the ratio of τ to *CPU time* multiplied by the *acceptance probability*; it is a measure of the speed at which

phase-space is being traversed. The system was then allowed to iterate up to a maximum of 2000 iterations with the minimum number of iterations being 800 and typical number of iterations being roughly 1500. Expectation values were taken after the 300th iteration; the value of 300 was chosen after noting the constancy of results obtained with differing numbers of starting iterations.

The above procedure required typically 8 hours of CPU time and 102 (K,Y) values were run simultaneously thus exploiting the parallelism available on the machine. This *machine gun* approach for scanning parameter space worked very well and enabled us to map out the phase diagram of the model easily.

Figures 3.5, 3.6, 3.7 and 3.8 show contour plots of the expectation values of the observables Q, R^2, P and CV, obtained on a 4^4 lattice from 420 (K,Y) points evenly distributed throughout the shown region. Closely-spaced contours indicate regions of rapid change in the observables and hence are expected to be seen in the region of phase transitions. Note the dashed lines marking the steep parts of the diagram; these are phase transition lines which separate (K,Y) space into regions of different phases.

Figure 3.5 has contours labelled in units of 0.01 and spaced in units of 0.05. Point A, is the 2nd order phase transition for the $d = 4$ XY-model [73,76]. The fermions appear to induce the Higgs fields into an aligned *Higgs phase.* For large Y, the fermions acquire a large mass and therefore they no longer affect the Higgs fields; the fermions decouple at $Y = \infty$. For values of K below that at point A, this causes the appearance of the two phase transition lines A-B and C-D. The line A-B looks to be the stronger transition but is hard to investigate because it lies in an area of the diagram that is heavily infra-red affected. Line C-D is the *decoupling transition* and is well described by the expression

$$K + \frac{1}{Y^2} \;=\; K_c$$

where K_c is the value of K at point A. This expression is what one expects from the $1/Y^2$ expansion if one drops terms of $O(1/Y^4)$ as shown in Appendix C. It is remarkable that the $1/Y^2$ expansion works so well down to the value of $Y = 2.44$ seen at point C.

Figure 3.6 has contours labelled in units of 0.01 and spaced in units of 0.10. The

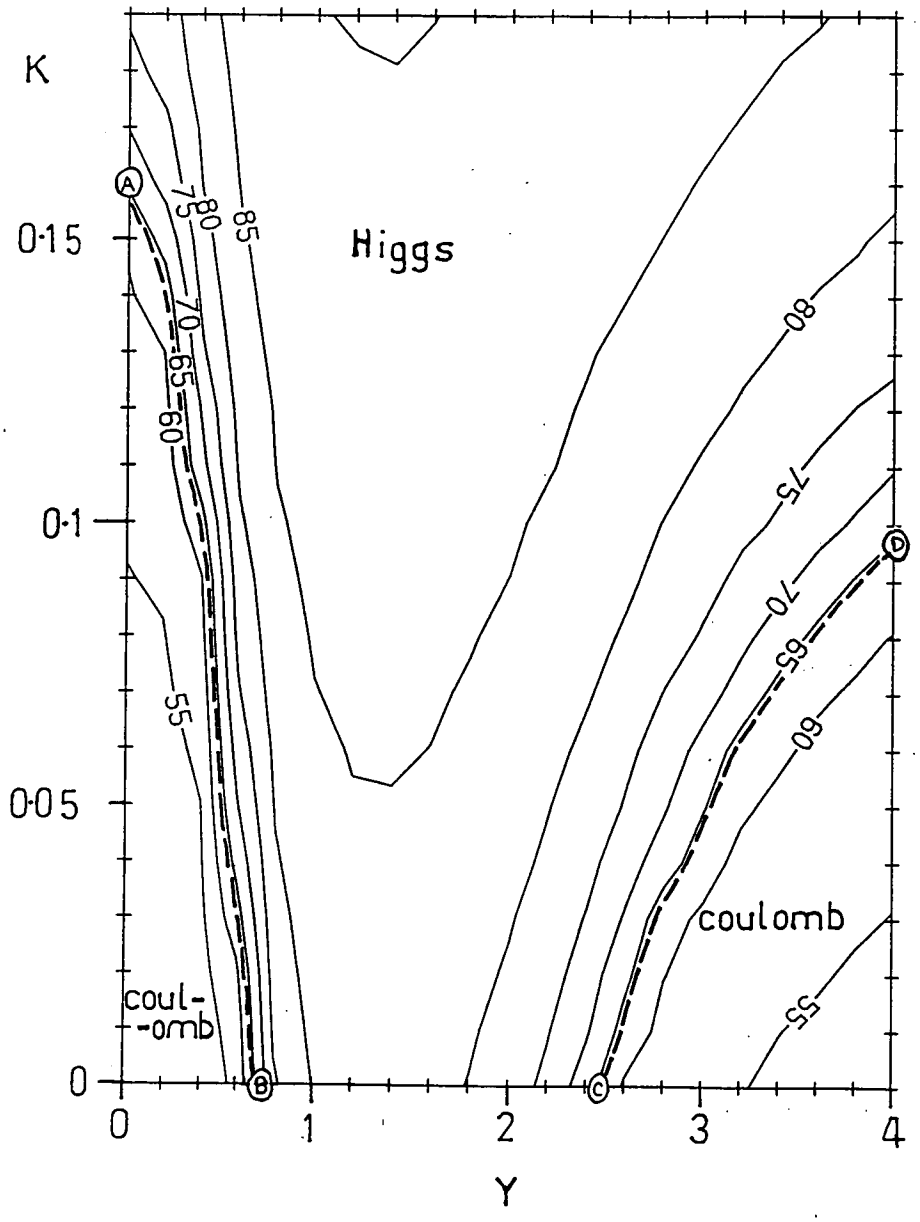

Figure 3.5: Contour plot of $< Q >$.

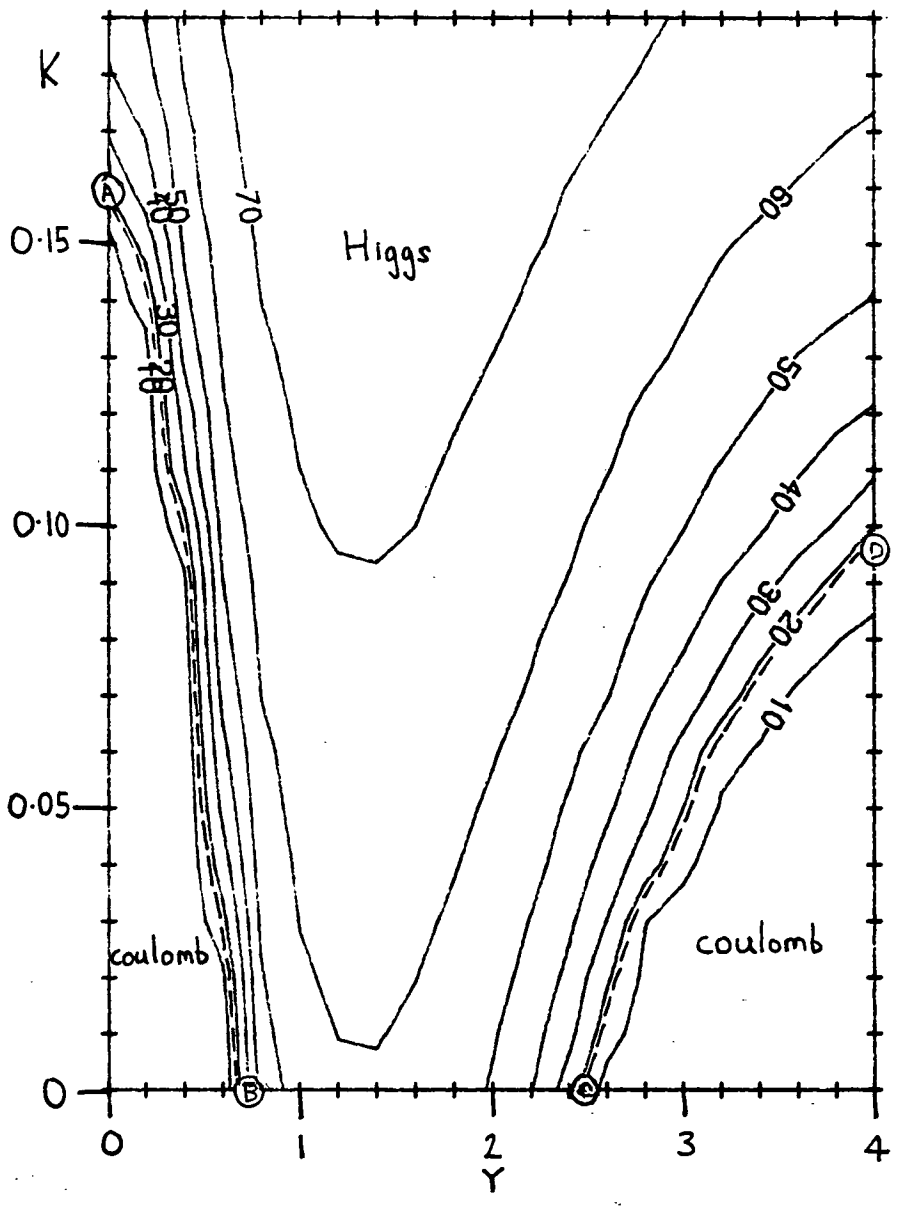

Figure 3.6: Contour plot of $< R^2 >$.

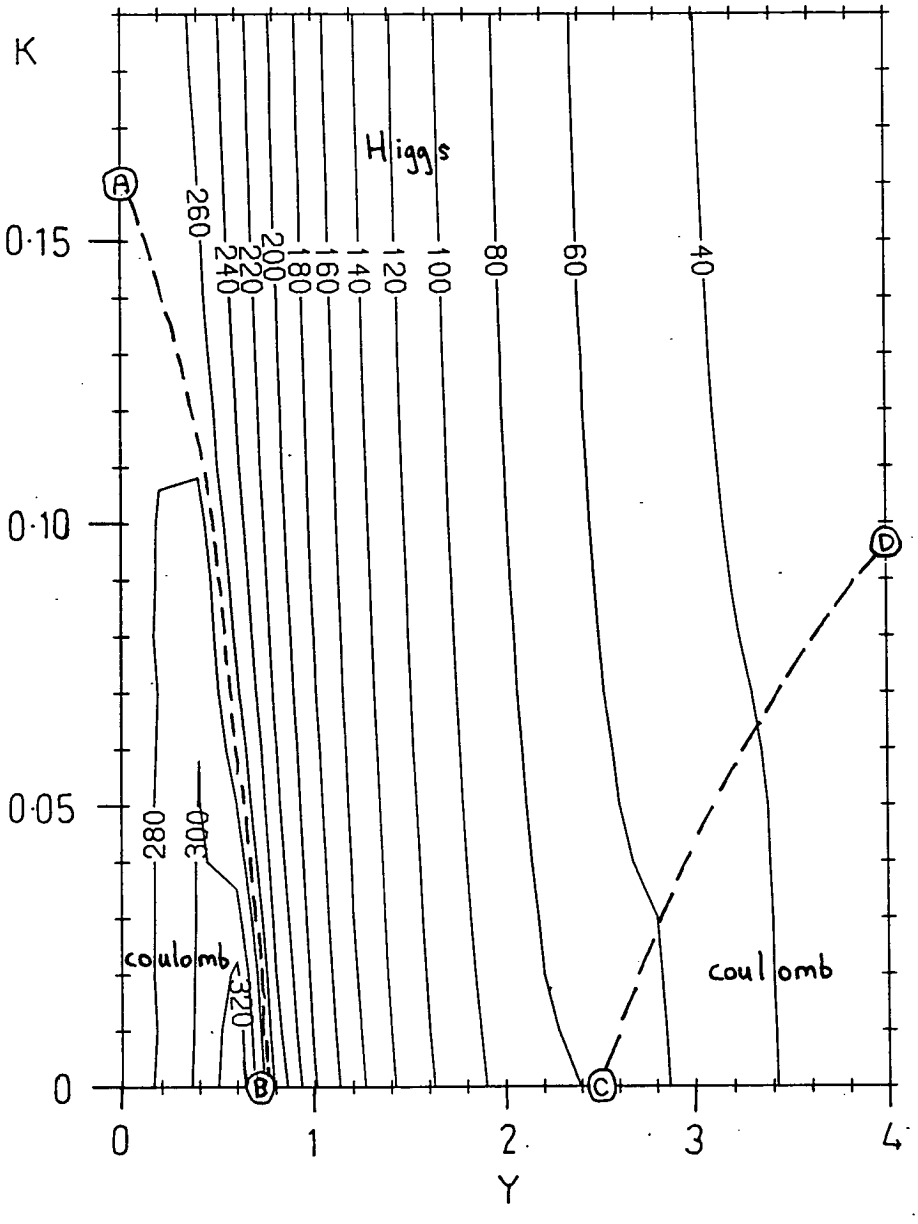

Figure 3.7: Contour plot of $< P >$.

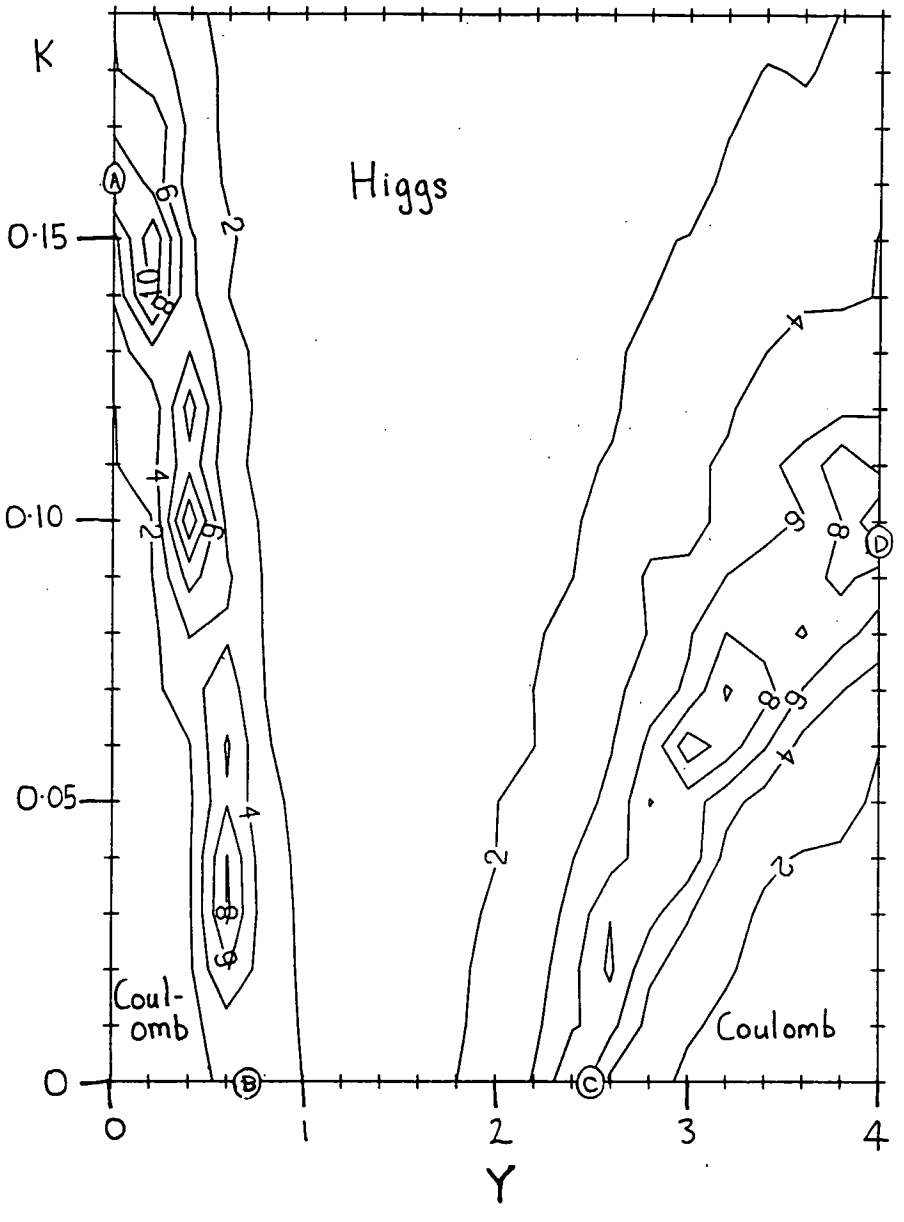

Figure 3.8: Contour plot of $< CV >$.

observable $< R^2 >$ behaves in a similar way to the observable $< Q >$.

Figure 3.7 has contours labelled in units of 0.01 and spaced in units of 0.20. $< P >$ is strongly affected in the region of line A-B and less so in the region of line C-D; the dashed lines have been marked on from those found in Figure 3.5.

Figure 3.8 has contours labelled in units of 0.0001 and spaced in units of 0.0002. The specific heat capacity $< CV >$ takes its largest values in the region of the phase-transition lines A-B and C-D. By estimating the positions of maxima in $< CV >$, we find (K, Y) values of $(0.15 \pm 0.01, 0)$, $(0, 0.64 \pm 0.1)$ and $(0, 2.44 \pm 0.1)$ for points A,B and C.

To find points A,B and C more accurately and to determine the order of the phase-transitions we performed two runs on a 6^4 lattice. The results for the $Y = 0$ and the $K = 0$ runs are shown in Figures 3.9 and 3.10. On the 6^4 lattice, A was at $(0.16 \pm 0.01, 0)$, B was at $(0, 0.68 \pm 0.1)$ and C was at $(0, 2.48 \pm 0.1)$. Within errors, these are the same as the values found on the 4^4 lattice.

Figure 3.11 shows the evolution of Q, R^2 and P with the number of iterations. By looking at similar plots, and not observing a 2-state behaviour, we conclude that there is no evidence for points B and C being strongly first-order transitions.

3.5 Conclusions

A toy model with a scalar hopping parameter K and a Yukawa coupling Y, has regions in (K, Y) space where the Higgs fields are aligned and regions where the Higgs fields are not aligned. The model posseses a U_1 global chiral symmetry associated with the alignment of the Higgs fields. Separating the regions are phase-transition lines; the phase transitions do not appear to be strongly first-order transitions. The fermions have the effect of aligning the Higgs fields when Y is large enough but at too large a Y the fermions appear to decouple giving rise to a decoupling transition. The decoupling transition is well described by the $O(1/Y^2)$ expansion. At small Y the fermions are heavily infra-red affected.

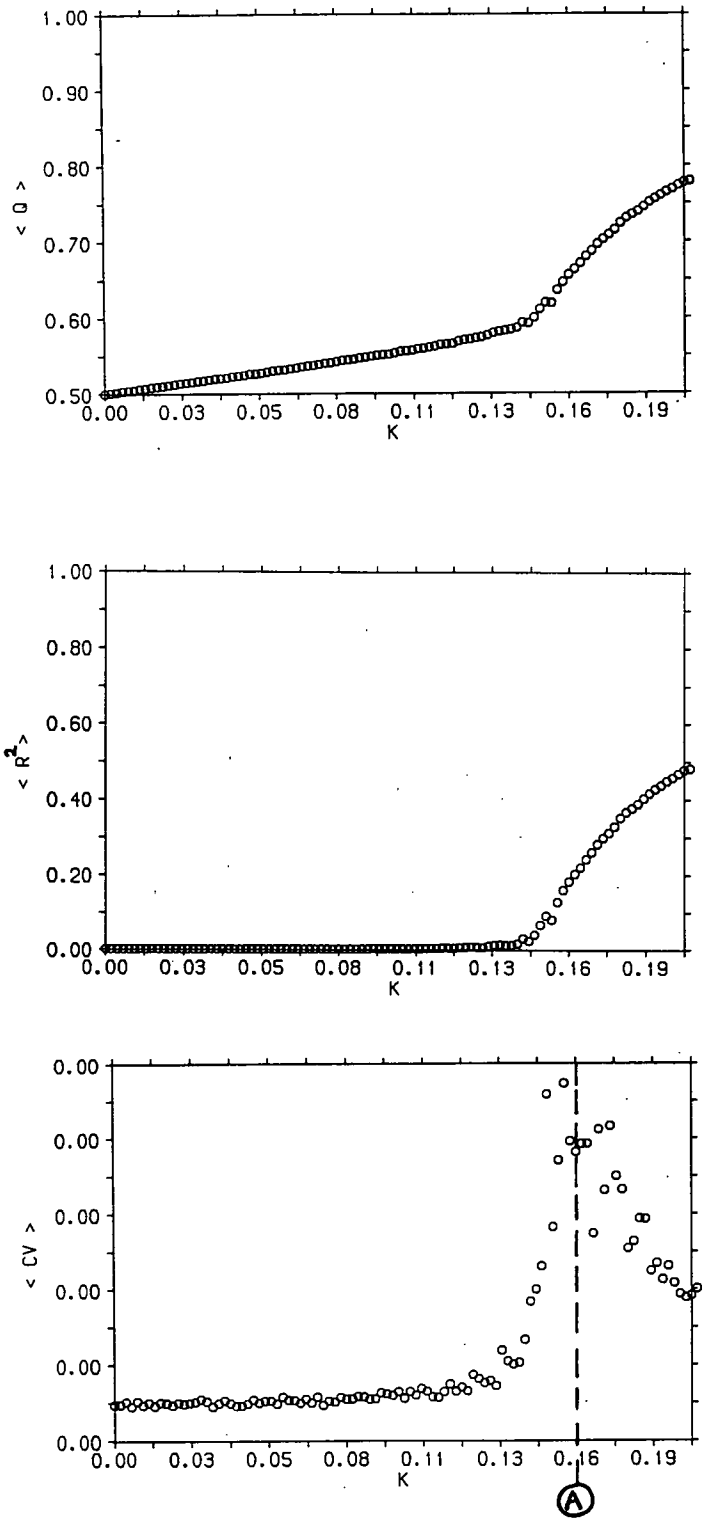

Figure 3.9: $Y = 0$ results on a 6^4 lattice.

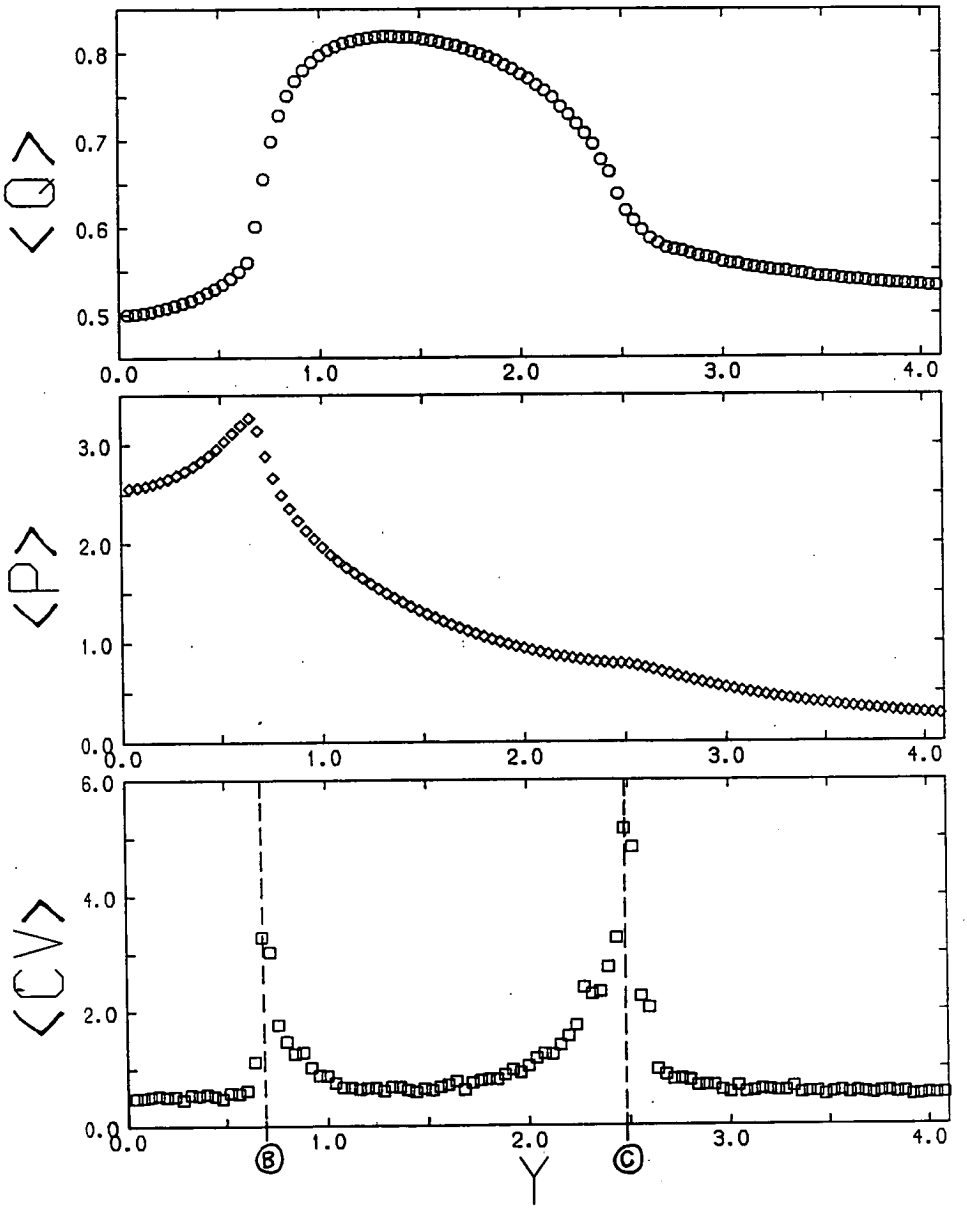

Figure 3.10: $K = 0$ results on a 6^4 lattice.

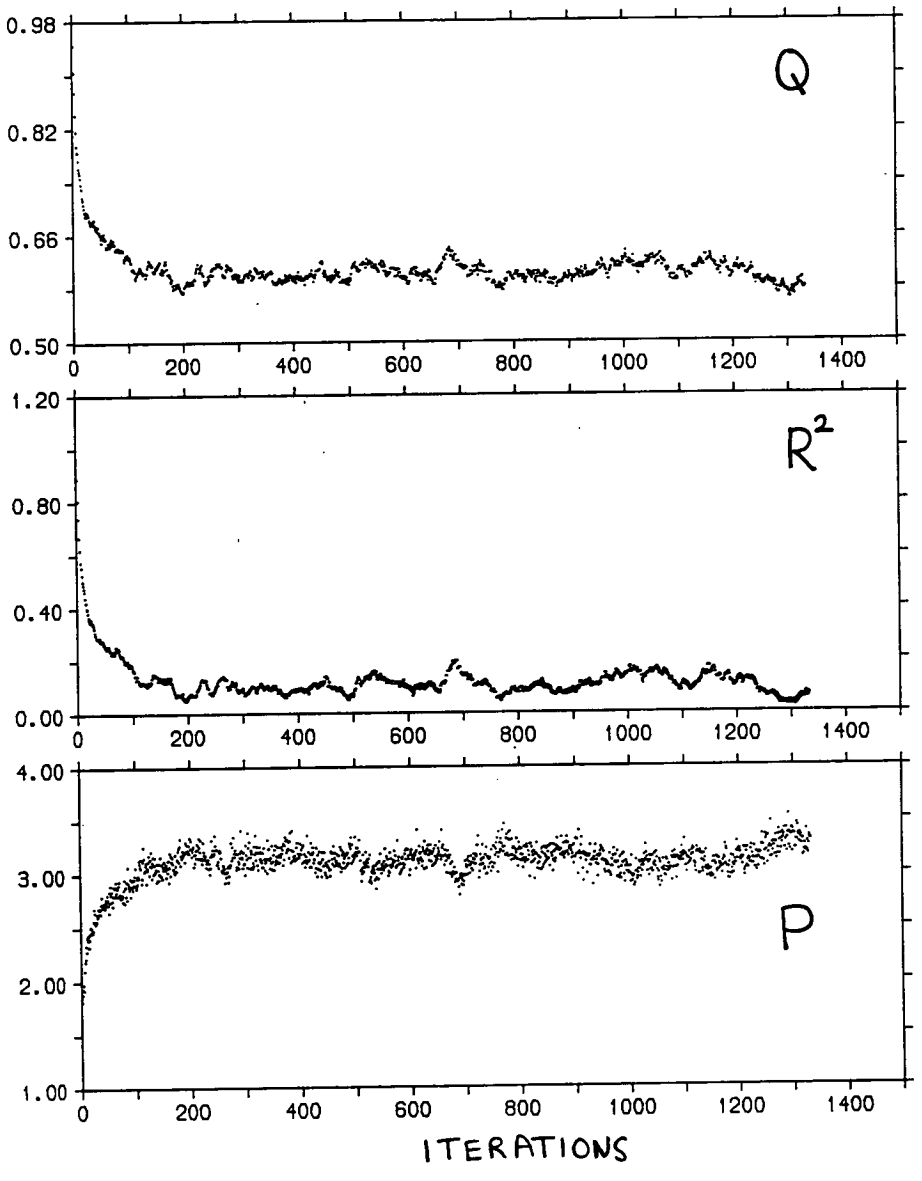

Figure 3.11: History at point B on a 6^4 lattice.

Open questions relating to this toy model are:

1. Are there ϕ such that $\det M$ is complex ?
2. Are phase-transition lines A-B and C-D part of the same line ?
3. What happens to A-B and C-D on much larger lattices ?

In addition to answering these questions, more extended models should be investigated. For example:

- Models that are not radially-fixed.
- Models which include the Yukawa-Wilson term.
- Fermion-Gauge-Higgs models.

In studying all these models, one would develop a far better understanding of the Electroweak model and of how it behaved dynamically. The toy model study used about 300 hours of run-time on 103 T800 boards and in so doing, performed an estimated number of about 10^{14} floating-point calculations.

3.6 Speculations

In this section, I wish to present a few personal speculations inspired by studying the toy model. The speculations raise some interesting questions for which I know no answers.

3.6.1 Complex Determinant

Conjecture 1 *There exist some ϕ for which* $\det M$ *is complex, where M is defined as the fermion matrix occuring in Eqn. (3.3).*

It is this conjecture that necessitated the use of M *and* $M^\dagger$ in the toy model.

The conventional proof of the reality of the fermionic determinant fails in the case of Yukawa couplings to complex Higgs fields. For $M = \not{D} + m$, where m is the fermion mass, the conventional proof goes as follows:

$$\begin{aligned}
(\det M)^* &= \det(\not{D}^\dagger + m^\dagger) \\
&= \det(-\not{D} + m) \\
&= \det\gamma_5(-\not{D} + m)\gamma_5 \\
&= \det(\not{D} + m) \\
&= \det M
\end{aligned}$$

For Yukawa couplings, m is replaced by $Y\phi$ and the property that $m^\dagger = m$ no longer works in general. This property is needed in going from line 1 to line 2 in the above proof and hence the reality proof fails in the case of Yukawa couplings.

Using the $1/Y^2$ expansion, one can show that $\det M$ is real up to $O(1/Y^6)$ for all ϕ and that it is real to all orders in $1/Y^2$ for $\phi = e^{i\theta_x}$ with $\theta_x = a.x + b$ and $a, b \in \Re$.

Complex measures are not easy to generate using Monte-Carlo techniques and so, if $\det M$ is complex, simulation of single-species Yukawa models may be difficult.

3.6.2 Singular fermions

Conjecture 2 *In the infinite-volume limit, the phase-transition line A-B will move in towards the* $Y = 0$ *line.*

This conjecture is not supported by comparing the results for point B on the 4^4 and 6^4 lattices. For such small lattices, however, infra-red effects may be very dominant; work on much larger lattices needs to be performed.

Perturbation theory in Y provides a hint that something very singular may be occuring at $Y = 0$. As shown in Appendix C, the fermion determinant can be

written in terms of a sum over 2n-legged fermion bubble diagrams where n = $1, 2, \ldots, \infty$ is the number of ϕ and $\phi^\dagger$ legs connected to the bubble. The 2n-legged bubble is the $O(Y^{2n})$ term in the expansion and has 2n fermion momenta in its denominator. The fermion momenta can be zero and this leads to infra-red divergences. Note how the higher-order terms in the Y expansion have stronger infra-red divergences. This doesnt look like a feature one would expect to see in a convergent series.

Problems with convergence also can be seen in the effective potential formalism. The fermion bubbles summed to give V_{eff} produce a logarithmic singularity in the coupling constant. However, the singularity can be shown to be illusory; it is eaten by the renormalization counterterms. The Z term also has infra-red divergences all be it, less severe than those in V_{eff}. Unlike V_{eff} however, it is not obvious how to construct counterterms that will make Z both infra-red and ultra-violet convergent [4]. Hence a singularity at $Y = 0$ may appear in the effective potential formalism.

3.6.3 A New Mexican Hat

In this subsection, I will discuss recent results found by my collaborator using the code that we wrote for the toy model [77]. Recent work has been focussed upon understanding the radially-free model. The action for this model is given by:

$$\begin{aligned} S &= -K \sum_{x,\hat{\mu}} \left(\phi_x^\dagger \phi_{x+\hat{\mu}} + \phi_x^\dagger \phi_{x-\hat{\mu}} \right) \\ &\quad + \sum_x \phi_x^\dagger \phi_x \\ &\quad + \sum_{x,y} \left(\overline{\psi}_x^{(1)} M_{xy} \psi_y^{(1)} + \overline{\psi}_x^{(2)} M_{xy}^\dagger \psi_y^{(2)} \right) \end{aligned} \tag{3.7}$$

with M defined as previously. The ϕ are no longer constrained to unit radius but are of the form $\phi = re^{i\theta}$. The effective fermion action S_{eff} for this model has an extra term arising from the radial degrees of freedom:

$$V_{RM} = -\sum_x 4 \log(Y \phi_x^\dagger \phi_x)$$

[4] Private communication with S. Coleman

This has been named the Ring-Mould potential [5]. Together with only a conventional mass term $m^2\phi^\dagger\phi$ this potential can produce a minimum in the potential away from $\phi^\dagger\phi = 0$; a $\lambda(\phi^\dagger\phi)^2$ term is no longer needed in order to produce a non-zero VEV !

Figure 3.12 shows the results obtained on the line $K = 0$ for this model. Note how $< \sum \phi^\dagger\phi/N >$ increases with Y and how at large Y, it approaches the value of 5. This is what one expects from the VEV being caused by the Ring-Mould potential. Neglecting space-time variations in ϕ gives:

$$\begin{aligned} < \frac{1}{N}\sum_x \phi_x^\dagger\phi_x > &= \frac{\int dr r^2 \exp(-r^2 + 4\log r^2)}{\int dr \exp(-r^2 + 4\log r^2)} \\ &= \frac{5!}{4!} = 5 \end{aligned} \tag{3.8}$$

Because of the existence of the RM-potential in Yukawa-coupled FH systems, it could be that the $\lambda\phi^4$ term is no longer a necessary part of the electroweak model. Furthermore, the Higgs VEV would no longer be arbitrary but would be related to the number of fermionic species in the model.

[5] Named not after a tropical disease but after an instrument used to make cakes.

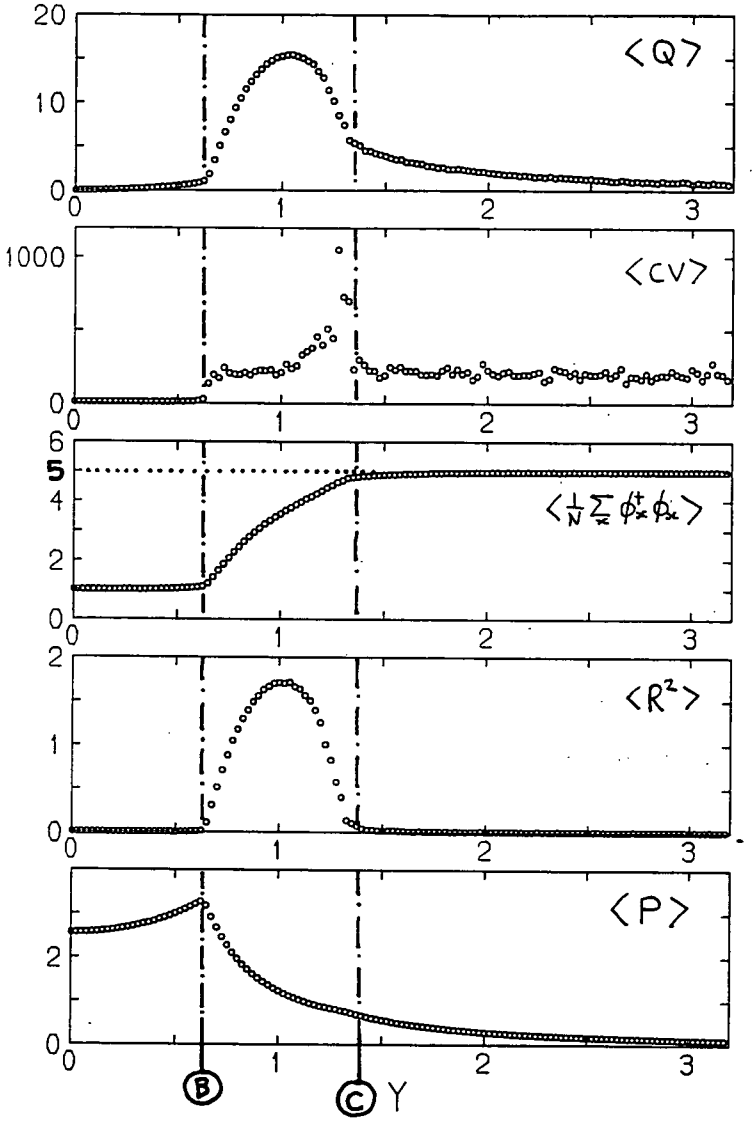

Figure 3.12: Radially-free results on a 6^4 lattice.

Chapter 4

Finer Threads.

The myriad confusion of thin waves
and the fine partings of the foam
became in desperation an infinity of lines
spewed out over the sea as from silkworms.
Y. Mishima

What is the fabric of space-time ? The usual assumption is that space-time is a smooth manifold. However, might not space-time be a more fundamental topological structure of which the smooth manifold is only a low-energy limit ?

Both the theory of quantum gravity and string theory require sums to be performed over all possible topologies of manifolds. In quantum gravity, the unboundedness of the Einstein curvature term in the continuum Euclidean action signals violent fluctuations in the manifold at distances close to the Planck scale of 1.7×10^{-37} metres; space-time is expected to be a foam at these scales [78]. In summing over all possible topologies, why should there be a restriction to only those structures that are smooth manifolds ?

Lattices can be used to generate the topologies of smooth manifolds by acting as discrete approximations to smooth surfaces. In quantum gravity, the technique of Regge calculus uses simplicial lattices in order to perform the sum over all topologies of manifold. However, lattices can include richer topological structures than those found in smooth manifolds. For example, consider the lattice

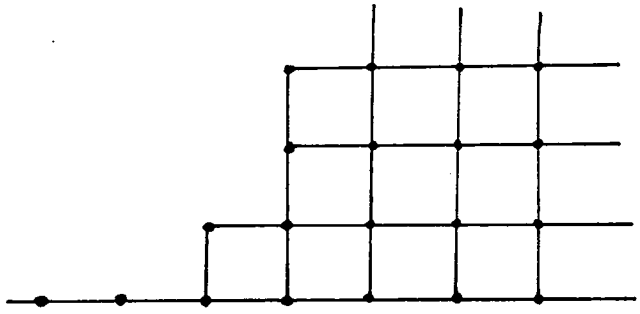

Figure 4.1: A Lattice Topology.

shown in Figure 4.1; it changes from a 1-dimensional structure on the left into a 2-dimensional structure on the right. The lattice may play a more fundamental role than just being a type of ultra-violet regulator.

In using lattices rather than smooth manifolds, one loses the ability to use the tools of differential calculus; discrete structures are hard to study mathematically. For this reason, I have only looked at a class of lattices known as regular fractals [81,82]. Fractals have the virtue that they are self-similar under dilatations which therefore allows *decimation* to be performed exactly [83]. Decimation is the technique whereby sites on smaller scales are removed leaving only sites on a lattice with larger spacing; in the case of regular fractals, the lattice with a larger spacing has the same topology as the original lattice and so the procedure can be repeated ad infinitum.

The structure of this chapter is as follows:

1. **Discrete Language** A physicists view of the mathematical techniques that can be used to describe lattice structures.

2. **Scalar Propagation** Using the techniques of the previous section, the propagator for the Klein-Gordon equation is examined on a 1-dimensional

chain and on a Sierpinski gasket.

3. **Fermion Propagation** Staggered fermions are investigated on 2-dimensional truncated fractals with a view to eliminating fermion doubling.

4.1 Discrete Language.

Functions defined on lattices can be described by an area of mathematics known as *cell-complex cohomology* [84]. Cell-complex cohomology is analogous to *de Rham cohomology* which decribes the behaviour of *differential forms* [85]. Differential forms are antisymmetric tensor fields defined on smooth compact manifolds. The field equations of physics are defined on smooth manifolds and can be rewritten into equations containing differential forms [86,87]. These can then be mapped into the analogous equations in cell-complex cohomology and hence the field equations of physics can be transcribed onto lattice structures.

This section describes the language of cell-complex cohomology which will then be used in the next section. No attempt is given to review the more familiar de Rham cohomology. The approach in this section is that of a pragmatic physicist rather than that of an algebraic topologist; more detailed mathematics is to be found in [84,88,80].

4.1.1 Cell-complex

Definition 1 *A finite cell-complex K, of dimension D, is the set of oriented p-cells $\{c_0, c_1, \ldots, c_D\}$ such that $c_p \in K$ implies that its boundary $\partial c_p \in K$ and such that $c_p = c'_p$ implies that $\partial c_p = \partial c'_p$.*

For an example consider a two-dimensional square lattice. This is a cell-complex with D=2 and with c_0, c_1 and c_2 being the sites, unit links and unit squares respectively; it is referred to as a cubic cell-complex. The two-dimensional triangular lattice is another example and is referred to as a simplicial cell-complex;

the triangular plaquettes are known as simplices. Cell-complexes K approximate manifolds M in the limit that the plaquettes become vanishingly small providing that they have the same topology as the manifolds.

4.1.2 Incidence functions

The topological structure of a cell-complex is contained in its *incidence functions*. The incidence function $I(c_p, c_{p+1})$ is defined as:

$$I(c_p, c_{p+1}) = \begin{cases} \pm 1 & \text{if } c_p \in \partial c_{p+1} \\ 0 & \text{otherwise} \end{cases}$$

The sign is ± 1 depending upon the orientation in which c_p is included in c_{p+1}. Examples of incidence functions are shown in Figure 4.2.

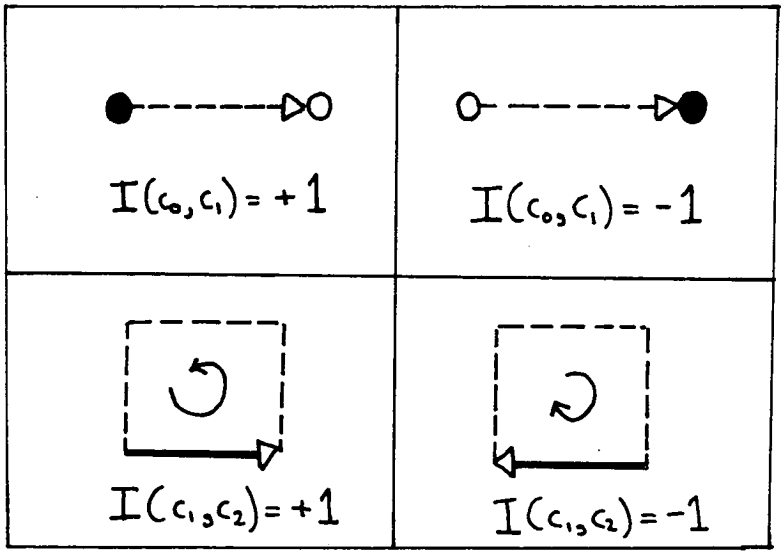

Figure 4.2: Examples of Incidence functions.

Incidence functions satisfy the following identity

$$\sum_{c_p} I(c_{p-1}, c_p) I(c_p, c_{p+1}) \;=\; 0 \qquad (4.1)$$

which is true for all cell-complexes.

4.1.3 Cochains

Functions can be defined on p-cells and are called *p-cochains* $f(c_p)$. For example, in lattice gauge theory, functions of fields on the sites, links and plaquettes are respectively 0-cochains, 1-cochains and 2-cochains. Operators which act on cochains can be defined.

The *boundary operator* d is defined as:

$$df(c_p) = \sum_{c_{p+1}} I(c_p, c_{p+1}) f(c_{p+1})$$

It converts a p-cochain into a (p+1)-cochain and is local in the sense that only the c_{p+1} which include c_p in their boundaries contribute. Note that $df(c_D) = 0$ because there are no (D+1)-cells.

The *coboundary operator* $\hat{d}$ is defined as:

$$\hat{d}f(c_p) = \sum_{c_{p-1}} I(c_{p-1}, c_p) f(c_{p-1})$$

It converts a p-cochain into a (p–1)-cochain and is local in the sense that only the c_{p-1} which are included in the boundary of c_p contribute. Note that $\hat{d}f(c_0) = 0$ because there are no (–1)-cells.

Both the boundary and coboundary operators satisfy the *cocycle conditions* that $d^2 = 0$ and $\hat{d}^2 = 0$; these are consequences of identity (4.1).

4.1.4 Transcription

Cell-complex cohomology is analogous to de Rham cohomology [80,89]. The complex K is analogous to the manifold M, the p-cochain is analogous to the p-form, the boundary operator d is analogous to the exterior derivative $\mathbf{d}$ and the coboundary operator $\hat{d}$ is analogous to the derivative $\delta = *\mathbf{d}*$. The cocycle conditions are equivalent to the statements that $\nabla.(\nabla \times A) = 0$ and $\nabla \times \nabla\phi = 0$. In the limit that the cell-complex approximates the manifold, the analogous quantities become identical as can be shown using the Whitney mapping [80].

Using these analogies we can transcribe equations written in terms of de Rham cohomology into equations written in terms of cell-complex cohomology and hence we can start to investigate the equations on cell-complexes. This is not the only possible transcription but it has the merit that it is geometrically appealing.

The Laplacian ∂^2 becomes $\mathrm{d}\delta + \delta\mathrm{d}$ in the language of forms and maps p-forms into p-forms. The *Hodge-de Rham* equation is defined as:

$$(\mathrm{d}\delta + \delta\mathrm{d})\omega \;=\; 0$$

It is a rewriting of Laplace's equation in a way which is independent of the particular metric on the manifold. Similarly, the Klein-Gordon equation $(-\partial^2 + m^2)\phi = 0$ can be written as

$$(\mathrm{d}\delta + \delta\mathrm{d} - m^2)\omega \;=\; 0$$

and transcribes to the cell-complex equation

$$(d\hat{d} + \hat{d}d - m^2)\omega \;=\; 0$$

This can be expressed in terms of the incidence functions as

$$\sum_{c'_p, c_{p-1}} I(c_{p-1}, c_p) I(c_{p-1}, c'_p)\omega(c'_p) + \sum_{c'_p, c_{p+1}} I(c_p, c_{p+1}) I(c'_p, c_{p+1})\omega(c'_p) \;=\; m^2\omega(c_p) \qquad (4.2)$$

and hence the Klein-Gordon equation can be transcribed onto cell-complexes once the incidence functions are known.

Fermions are described in a metric-independent way by the use of the Dirac-Kahler equation [90,91]. The Dirac equation $(\gamma_\mu\partial_\mu + m)\psi = 0$ can be thought of as being one column in the matrix equation

$$(\gamma_\mu\partial_\mu + m)\Psi \;=\; 0$$

In 4 dimensions, Ψ is a 4×4 matrix and it can be expanded as the sum over 5 antisymmetric tensor fields ω as

$$\Psi \;=\; \omega\, 1 + \omega_\mu\gamma_\mu + \omega_{\mu\nu}\gamma_{\mu\nu} + \omega_{\mu\nu\lambda}\gamma_{\mu\nu\lambda} + \omega_{\mu\nu\lambda\sigma}\gamma_{\mu\nu\lambda\sigma}$$

Viewing the ω as 0,1,2,3 and 4-forms, the Dirac equation becomes an equation that mixes forms:

$$(\mathrm{d} + \delta + m)\omega = 0$$

This is the Dirac-Kahler equation. Notice how left-multiplying by $(\mathrm{d} + \delta - m)$ gives the Klein-Gordon equation previously discussed; this is what one expects of a Dirac operator. The Dirac-Kahler equation transcribes to the cell-complex equation:

$$(d + \hat{d} + m)\omega = 0 \tag{4.3}$$

The ω is the sum of $0, 1, \ldots, D$-cochains which become mixed when the Dirac-Kahler operator is applied. On cubic complexes, if the p-cochains are thought of as functions living on the sites in the centre of the p-cells, one finds that the Dirac-Kahler equation is equivalent to the staggered formulation of free fermions [89].

4.2 Scalar Propagation

The propagators of classical field equations were first investigated on fractal lattices in 1986 by [92,93,94]. The massless Klein-Gordon equation on an arbritary metric was found to give Euclidean and Minkowskian fixed-point metrics. In this section, we will examine the massive Klein-Gordon equation on two types of cell-complex K_C and K_S. K_C is the 1-dimensional lattice chain shown in Figure 4.3 and K_S is the Sierpinski gasket shown in Figure 4.4. The chain was looked at for the sake of comparison purposes.

4.2.1 Klein-Gordon equation

We are interested in looking at the Klein-Gordon propagator G and how it behaves on K_C and K_S. The propagator equation is similar to Eqn. (4.2) but involves a source term $\delta(c_p)$:

$$\begin{aligned} \sum_{c'_p, c_{p-1}} I(c_{p-1}, c_p) I(c_{p-1}, c'_p) G(c'_p) \; + \\ \sum_{c'_p, c_{p+1}} I(c_p, c_{p+1}) I(c'_p, c_{p+1}) G(c'_p) \; - \\ m^2 \omega(c_p) = \delta(c_p) \end{aligned} \tag{4.4}$$

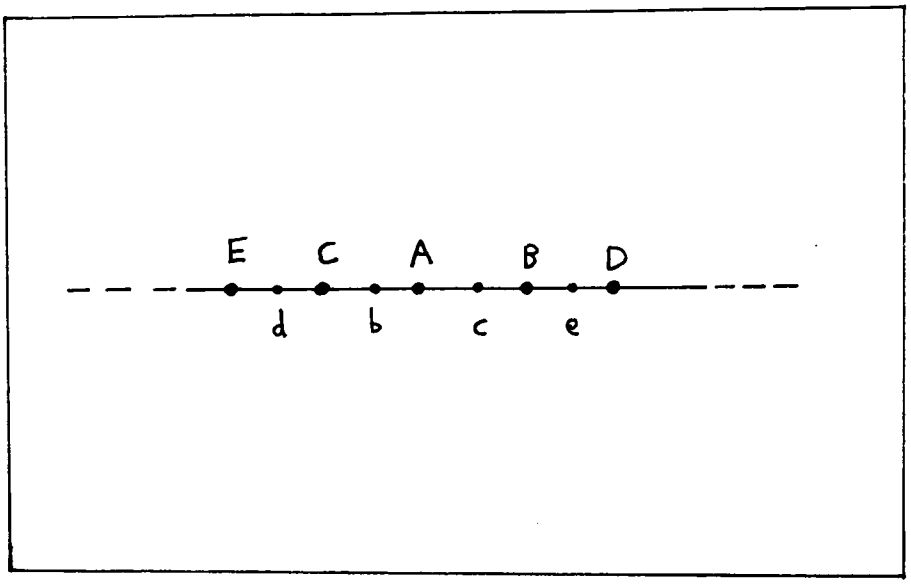

Figure 4.3: The chain K_C.

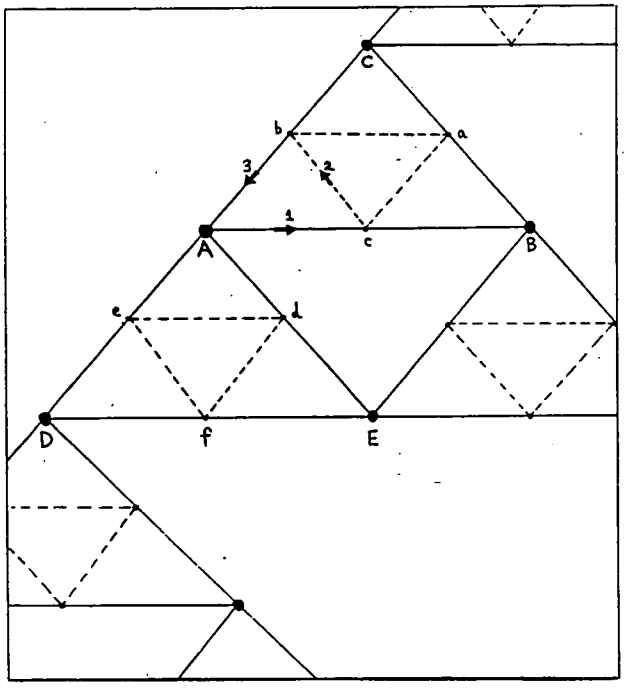

Figure 4.4: The Sierpinski Gasket K_S.

In what follows, I will specialize to the case $p = 0$ with the observation that the $p > 0$ cases can be obtained from the $p = 0$ equation by repeated left-multiplications with the boundary operator. The source term is equal to 1 on the source site and zero on all other sites.

On K_C, Eqn. (4.4) gives the expressions:

$$\begin{aligned} G_b + G_c + (m^2 - 2)G_A &= 1 \\ G_C + G_A + (m^2 - 2)G_b &= 0 \\ G_A + G_B + (m^2 - 2)G_c &= 0 \\ &\vdots \end{aligned} \tag{4.5}$$

The source has been placed on site A (refer to Fig. 4.3) and G_x denotes the propagator from the source site A to the site x.

Likewise, on K_S, Eqn. (4.4) gives the expressions:

$$\begin{aligned} G_b + G_c + G_d + G_e + (m^2 - 4)G_A &= 1 \\ G_b + G_e + G_B + G_C + (m^2 - 4)G_a &= 0 \\ G_a + G_c + G_A + G_C + (m^2 - 4)G_b &= 0 \\ G_a + G_b + G_A + G_B + (m^2 - 4)G_c &= 0 \\ G_f + G_e + G_A + G_E + (m^2 - 4)G_d &= 0 \\ G_f + G_d + G_A + G_D + (m^2 - 4)G_e &= 0 \\ G_e + G_d + G_E + G_D + (m^2 - 4)G_f &= 0 \\ &\vdots \end{aligned} \tag{4.6}$$

The source has been placed on site A (refer to Fig. 4.4).

4.2.2 Decimation

Referring to Figures 4.3 and 4.4, the propagators to the sites labelled by lowercase letters may be eliminated by using the equations (4.5) and (4.6). The resulting equations describe propagators on lattices of twice the original spacing. On both K_C and K_S, the new propagator equations happen to be of the

same form as the propagator equations on the smaller lattices and so the procedure can be repeated indefinitely. This decimation technique can be used to study the propagators.

On K_C, the new equations become:

$$\begin{aligned} G_B + G_C + (f(m^2) - 2)G_A &= g(m^2) \\ G_E + G_A + (f(m^2) - 2)G_C &= 0 \\ G_A + G_D + (f(m^2) - 2)G_B &= 0 \\ &\vdots \end{aligned} \tag{4.7}$$

And the functions f and g are found to be

$$\begin{aligned} f(z) &= z(4+z) \\ g(z) &= 2+z \end{aligned} \tag{4.8}$$

The new equations are of the same form as the original equations (4.5) but have a new mass $m^2 \rightarrow f(m^2)$ and a new source term $\delta \rightarrow g(m^2)\delta$.

Exactly the same behaviour occurs for K_S except that one finds f and g to be

$$\begin{aligned} f(z) &= z(5+z) \\ g(z) &= (2+z)\left(\frac{z+5}{z+6}\right) \end{aligned} \tag{4.9}$$

Note how the functions in (4.8) and (4.9) are quite similar.

4.2.3 Exact RG

The decimation procedure has resulted in performing an exact Renormalisation Group (RG) transformation. We have transformed equations describing physics on length scale L into equations describing physics on length scale $2L$. The procedure is exact; no truncations or approximations have been used. Renormalisation group transformations are associated with Ward identities, resulting from symmetries under dilatations, known as the Callan-Symanzik RG equations [95,96].

With our discrete transformation, we obtain the discrete RG equation:

$$G_{2x}(m^2) = g(m^2)G_x(f(m^2)) \tag{4.10}$$

The $G_{rx}(z)$ denote propagators to a lattice site distance rx away from the source for the Klein-Gordon equation (4.4) defined on a lattice with spacing 1 and having a mass of $m = \sqrt{z}$. The RG equation is obtained by mapping the new propagator equations describing propagation to sites $2x$ into the old equations. Function f is a mass renormalisation and function g is a wavefunction renormalisation. Equation (4.10) relates the behaviour of the propagator on different length scales and so provides information about the overall form of the propagator.

By applying the identity in (4.10) repeatedly, it is possible to relate propagators on scales of $1 \rightarrow 2 \rightarrow 2^2 \ldots$ with masses evolving as $m^2 \rightarrow f^{-1}(m^2) \rightarrow f^{-2}(m^2) \ldots$ and thus it becomes interesting to find where the masses evolve to under the repeated mapping $m^2 \rightarrow f^{-1}(m^2)$. The masses will evolve to the fixed-point $z = z^*$ given by $z^* = f(z^*)$ [97]. Figure 4.5 shows $f(z)$ for K_C. The intersections of the dashed and solid lines are at the points $z = f(z)$. The only non-negative fixed-point is at $z^* = 0$. Figure 4.6 shows $f(z)$ for K_S and once again the only non-negative fixed-point is at $z^* = 0$. Hence the fractal gasket has no fixed-points in addition to that of the trivial fixed-point found for the chain.

4.2.4 Propagator

The RG equation gives information about the propagator. If we assume that the propagator has the exponential form

$$G_x(z) = a(z)\exp(b(z)x)$$

we can use the RG equation over all x values in order to try to find $a(z)$ and $b(z)$.

For K_C, this gives

$$a(z) = \frac{1}{\sqrt{z(z+4)}}$$

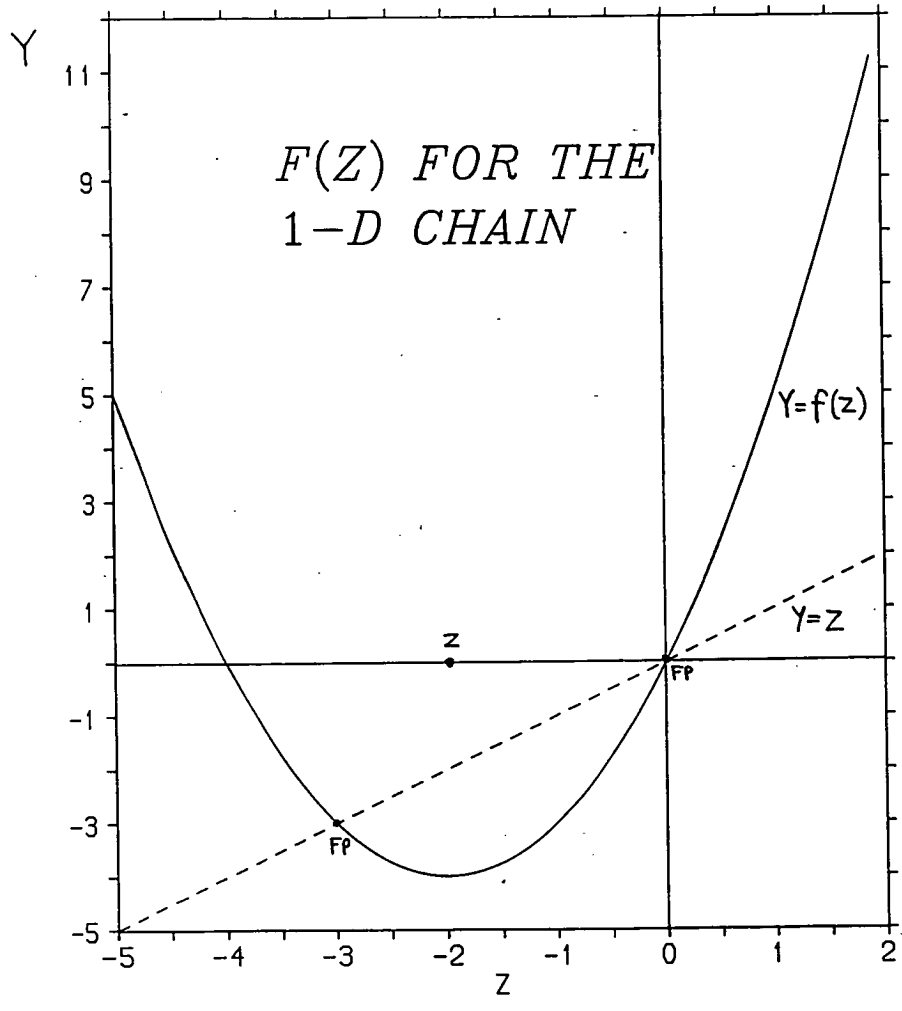

Figure 4.5: Mass-renormalization for the chain K_C.

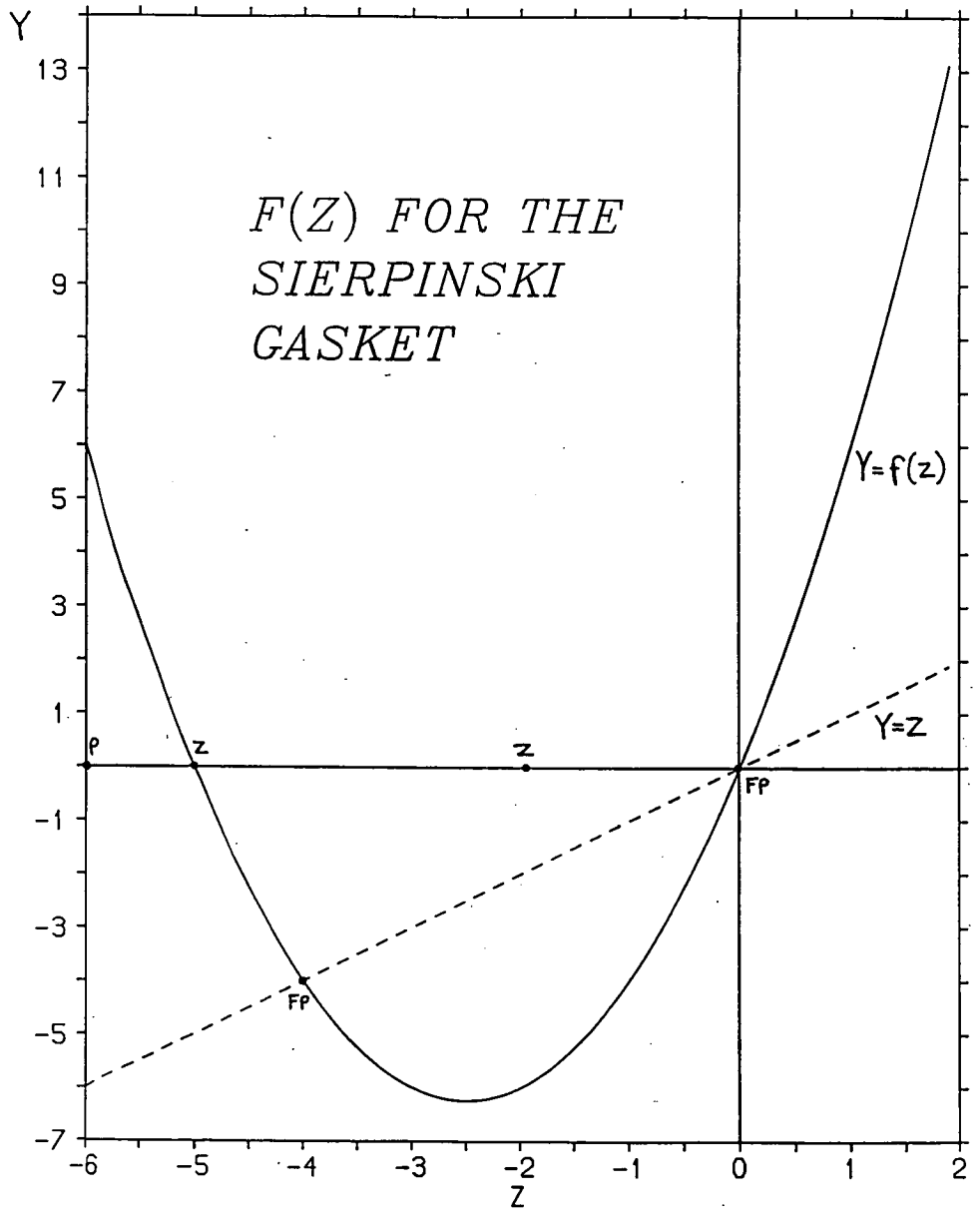

Figure 4.6: Mass-renormalization for the Sierpinski carpet K_S.

$$b(z) = \sinh^{-1}\left(\frac{\sqrt{z}}{2}\right)$$

These give the complete solution to the Klein-Gordon propagator on a 1-dimensional chain as can be shown by Fourier-expanding G and looking at poles in momentum space in the conventional manner. It is interesting to see that two quite different approaches can be used to find the propagator on the chain.

Unfortunately, finding $a(z)$ and $b(z)$ for the K_S seems very difficult. No closed form solutions, such as those found for K_C, appear to exist. If it were possible to find a and b, then one would know the behaviour of a propagator on a fractal structure. Such knowledge would be of use in the study of *fractons* which are believed to be special excitations occurring in amorphous materials [98,99].

4.2.5 Conclusions

In studying the Klein-Gordon propagator on K_C and K_S, I conclude that:

- Decimation is a powerful tool on fractal lattices and can give exact RG transformations.
- The Sierpinski gasket has no additional mass fixed-points to those seen on the chain.
- In principle, decimation results can be used to find the propagator but in practice, this involves the difficult task of finding closed forms that satisfy the RG equation and hence it has not been possible to find the explicit form for the propagator on the Sierpinski gasket.

4.3 Fermion Propagation

This section examines the behaviour of fermions moving over fractal space-times. Study of the Dirac-Kahler equation, using the decimation techniques of the last section, proved to be much harder than the study of the Klein-Gordon

equation. Rather than pursue this, an attempt was made to use truncated fractals as alternative ultra-violet regulators, with the hope that the notorious fermion doubling problem might not occur on such structures. This resulted in a numerical study of free staggered fermion propagation on a set of 2-dimensional Sierpinski carpets. This section is structured as follows:

1. **DK fermions** The problems with decimating DK fermions.
2. **Motivation** The motivation behind using truncated fractals as regulators.
3. **Weaving Carpets** Construction of Sierpinski carpets.
4. **Propagators** Finding propagators on the carpets.
5. **Doubling** Is there fermion doubling on the carpets ?
6. **Conclusions** Should we use Sierpinski carpets in lattice simulations.

4.3.1 DK fermions

The Dirac-Kahler equation (4.3) acts on a sum over all cochains and mixes them together. Writing $\omega = \omega_0 + \omega_1 + \omega_2$ with ω_p denoting the p-cochain, one can rewrite the DK equation (4.3) in 2-dimensions as

$$\begin{aligned} \hat{d}\omega_1 + m\omega_0 &= 0 \\ d\omega_0 + \hat{d}\omega_2 + m\omega_1 &= 0 \\ d\omega_1 + m\omega_2 &= 0 \end{aligned} \tag{4.11}$$

Hence it can be seen that the DK equation mixes functions of sites, links and plaquettes. Decimation removes a subset of the cell-complex and removes sites, links and plaquettes [1] with the result that the p-cochains on the larger lattice are sums over the $p = 0$, 1, and 2-cochains on the smaller lattice. The mixing of cochains, results in the decimated DK equation being not of the same form as the DK equation; it involves terms such as $\hat{d}d$ and $d\hat{d}$. The failure of the equation to map onto itself under decimations,

[1] Known in fractal jargon as a *trema*

stops one from being able to decimate repeatedly as is possible with the Klein-Gordon equation.

By eliminating the ω_0 and ω_2 in Eqn. (4.11), the equation can be rewritten as

$$\begin{aligned}(-d\hat{d} - \hat{d}d + m^2)\omega_1 &= 0 \\ \omega_0 &= -\frac{\hat{d}\omega_1}{m} \\ \omega_2 &= -\frac{d\omega_1}{m}\end{aligned}$$

This bears more than a passing resemblence to Eqn. (2.11) in Chapter 2; as mentioned previously DK fermions are equivalent to free staggered fermions. This has reduced the problem to that of finding the ω_1; once these are known, the ω_0 and ω_2 can be found from them. As can be seen, the ω_1 are the solutions of the Klein-Gordon equation investigated in the previous section. Unfortunately, the explicit solution to the KG propagator equation could not be found on K_C as mentioned in the last section.

These problems make the study of fermions on fractals very difficult. In what follows, we will turn our attention instead, to looking at the use of fractals as regulators rather than as fundamental models of space-time.

4.3.2 Motivation

Consider an amorphous solid such as an epoxy resin [99]. The molecules inside it are clustered randomly with big clusters having smaller clusters inside them. The self-similarity of such amorphous solids has led people to use fractal models to describe them [98]. Fractals appear to capture some of the features of random structures. In lattice gauge theory, there have been proposals that the use of random lattices rather than cubic lattices can eliminate the problem of fermion doubling [100,101,102,103,104,105,106,107]. In what follows, I attempt to use a class of regular fractals as controllable approximations to random lattices and will address the question of fermion doubling on such structures.

Fractals have the advantage over random lattices in that they can be tuned

to have different Hausdorff-Besicovitch (HB) dimensions, lacunarity [2], homogeneity etc. [108]. Numerical studies of Ising models on Sierpinski carpets give critical exponents that suggest that fractals may be used as extrapolations to non-integer dimensions [108,109,110,111,112,113].

I have generated 36 types of Sierpinski carpet, embedded in a 64×64 lattice, with HB dimensions ranging from values of 1.602 to 1.995. On each of these, I have then numerically calculated 3 types of staggered fermion propagator for a range of bare fermion masses. The existence of fermion doubling is then investigated by looking at the chiral condensate and at the degeneracy in different momentum channels. The hope behind this work, was that doubling might not exist on fractals in the same way that it might not exist on random lattices, in which case one might be able to tune the dimension of the fractal to 2 and obtain a translationally-invariant lattice regulator on which there was no doubling.

4.3.3 Weaving Carpets

The Sierpinski carpet is a square version of the more familiar Sierpinski gasket shown in Figure 4.4. To construct an n-level truncated carpet, the following procedure was used:

(a) Take a square and divide it into a grid of b^2 smaller squares.

(b) Divide each smaller square into a grid of c^2 smaller sub-squares.

(c) Remove tremas consisting of the central l^2 sub-squares from each small square.

(d) Taking the new square as each of the sub-squares, repeat steps **1**, **2** and **3** n–1 times.

The b, c and l are integers which are varied to give different types of carpet denoted by (b, c, l). The HB dimension of the carpet (b, c, l) is given by

$$d_{HB} = \frac{\log(b^2(c^2 - l^2))}{\log(bc)}$$

To achieve almost translationally-invariant lattices with $d_{HB} = 2 - \epsilon$, one can keep c and l constant and let $b \rightarrow \infty$.

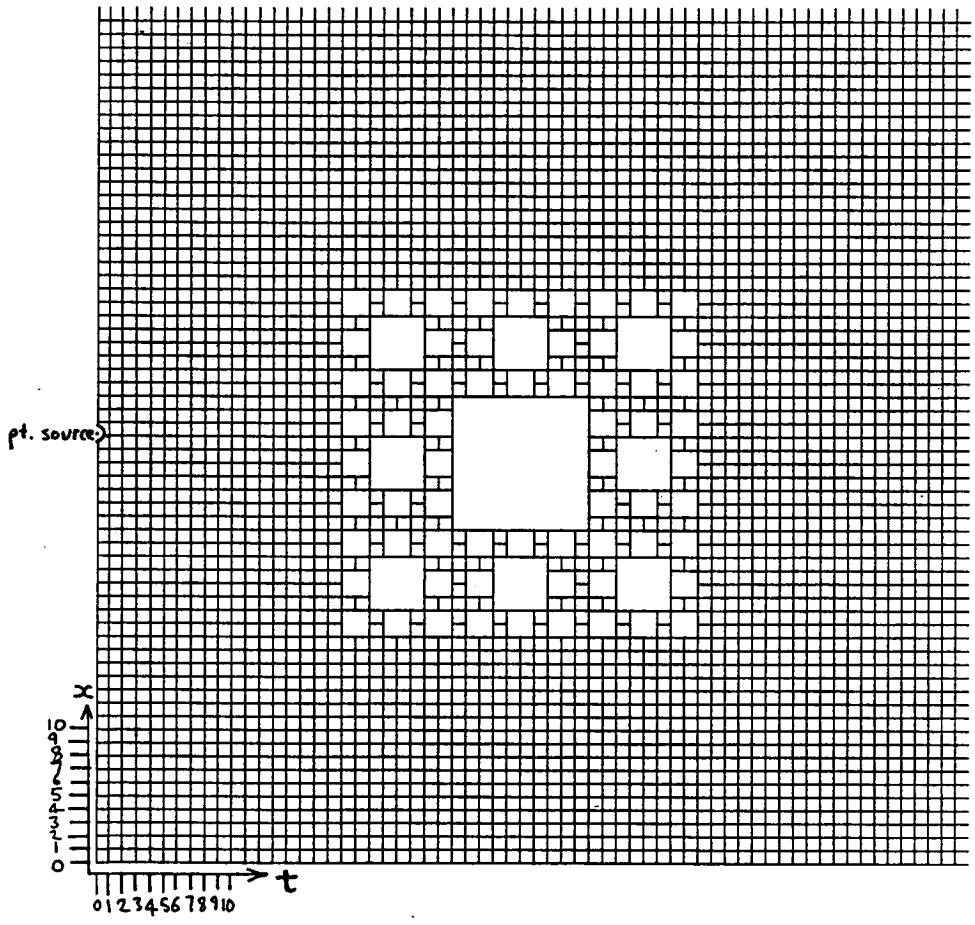

Figure 4.7: The $(1, 3, 1)$ Sierpinski lattice.

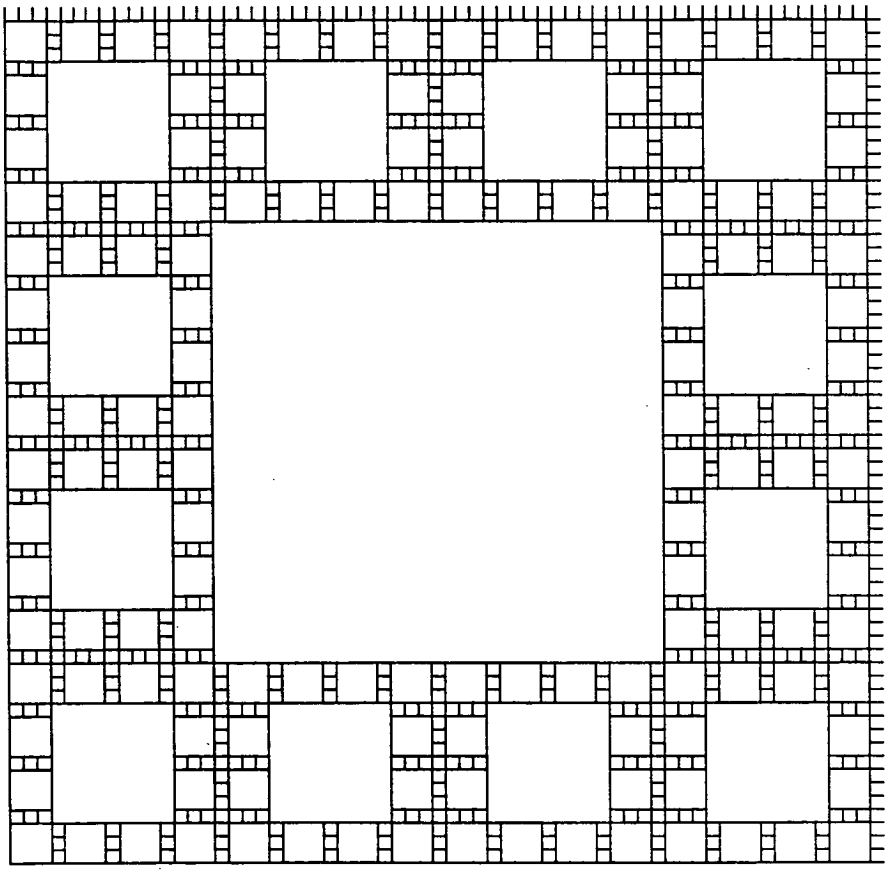

Figure 4.8: The $(1, 4, 2)$ Sierpinski lattice.

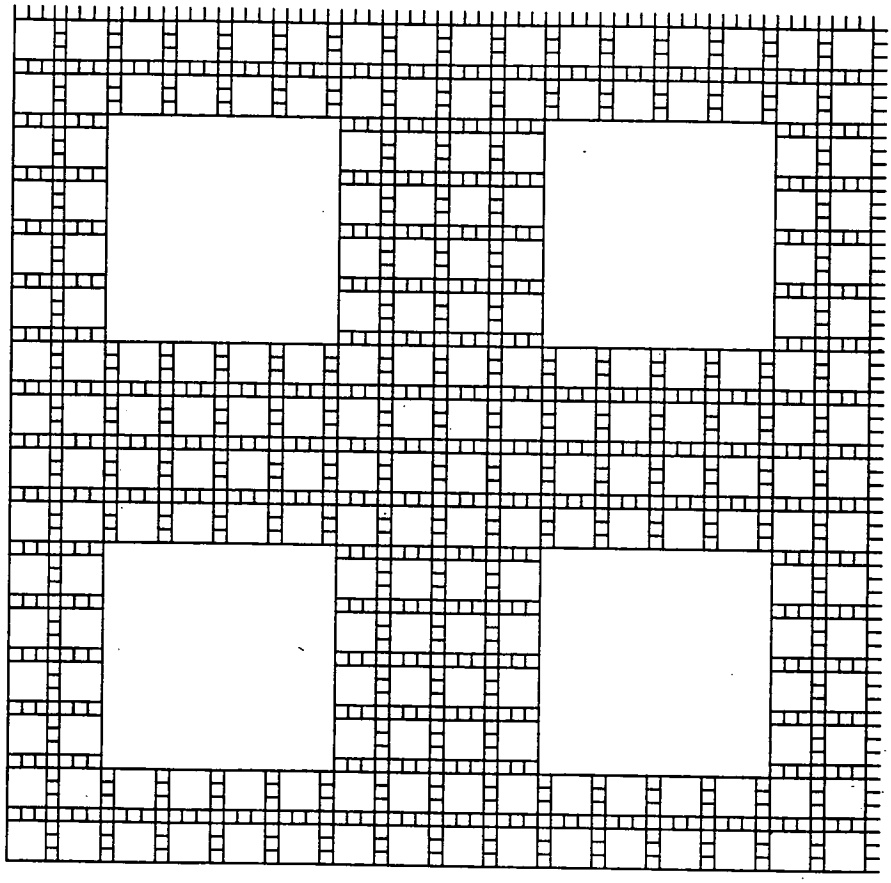

Figure 4.9: The $(2, 4, 2)$ Sierpinski lattice.

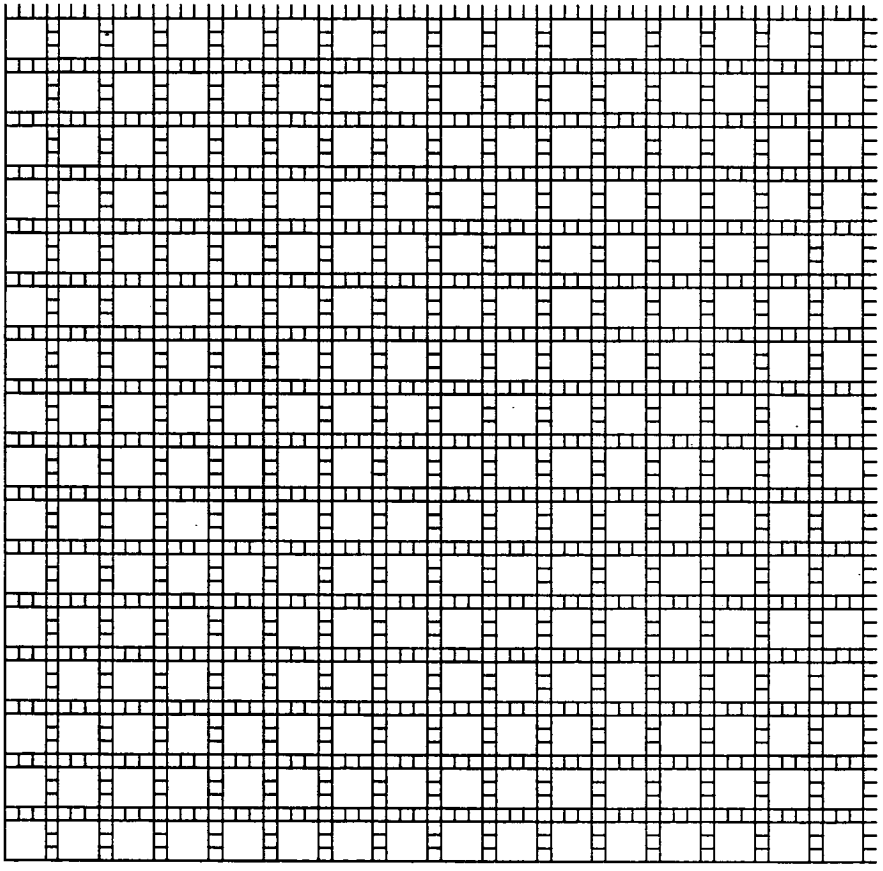

Figure 4.10: The $(16, 4, 2)$ Sierpinski lattice.

To make a lattice out of a truncated carpet, lattice sites were placed in the centres of the smallest squares and were then joined to neighbouring sites by lattice links. The lattices were embedded in a lattice of size 64×64 with the truncation level n taken to be as large as possible for each choice of (b, c, l).

b	c	l	d_{HB}	b	c	l	d_{HB}
5	11	3	1.981	1	3	1	1.893
1	4	2	1.792	2	4	2	1.862
1	5	3	1.723	1	6	2	1.934
1	6	4	1.672	1	7	3	1.896
1	7	5	1.633	1	8	2	1.969
1	8	4	1.862	1	8	6	1.602
2	3	1	1.934	21	3	1	1.972
16	4	2	1.931	12	5	3	1.891
12	5	1	1.990	10	6	4	1.856
10	6	2	1.971	9	7	5	1.828
9	7	3	1.951	9	7	1	1.995
8	8	6	1.801	8	8	4	1.931
8	8	2	1.984	7	9	7	1.776
7	9	5	1.911	7	9	3	1.972
7	9	1	1.997	6	10	8	1.750
6	10	6	1.891	6	10	4	1.957
6	10	2	1.990	5	11	9	1.724
5	11	7	1.870	5	11	5	1.942

Table 4.1: Sierpinski carpets that were used.

Table 4.1 shows the carpets that were generated along with their associated HB dimensions. Figures 4.7, 4.8, 4.9 and 4.10 show some of the lattices; they can be regarded as regular square lattices that have had holes cut into them.

[2]The number of big holes, roughly speaking!

4.3.4 Propagators

How do free fermions behave on these bizarre types of lattice ? To answer this question, the 2-point Greens function for free staggered fermions was calculated numerically using a conjugate gradient algorithm. The fermion matrix M can be written as

$$M_{xy} = m\delta_{xy} + \frac{1}{2}\sum_{\mu=1}^{4}\eta_\mu(x)\left(B_\mu(x)\delta_{y,x+\hat{\mu}} - B_\mu(y)\delta_{y,x-\hat{\mu}}\right)$$

with the B_μ being binary "gauge" links; they are 0 or 1 depending on whether a link is present at that point on the lattice. The matrix has chirality $\gamma_5 M = -M\gamma_5$ when $m = 0$, hermiticity $M = \gamma_5 M^\dagger \gamma_5$ and a remnant of translational invariance $TM = MT$ with T being a translation operator. For example, the $(16, 4, 2)$ carpet shown in Figure 4.10 has a remnant translational symmetry under shifts of 4 lattice units. Because full translational symmetry is no longer present on the carpets, momentum eigenstates are no longer Hamiltonian eigenstates and hence the concept of a dispersion relation becomes meaningless. The dispersion relation is a key ingredient in the no-go theorem for putting fermions on the lattice [8,9,12,13,14,7] and therefore fermions on fractal carpets may be able to avoid doubling.

In finding the propagators G from the equations $MG = b$, three types of source b were used:

$$\begin{aligned} b_{pt} &= \delta_{x=32}\delta_{t=0} \\ b_0 &= \sum_x \delta_x \delta_{t=0} \\ b_\pi &= \sum_x e^{i\pi x}\delta_x\delta_{t=0} \end{aligned}$$

The x and t refer to the *space* and *time* directions shown in Figure 4.7. The first type of source b_{pt} is the usual point source. The other two sources b_0 and b_π are sources which project only 0 and π momentum states. The equations were solved using a conjugate gradient algorithm implemented on the ICL DAP; periodic boundary conditions were adopted in both the space and time directions.

Table 4.2 shows the number of iterations required for convergence for some of the carpets using source b_{pt}; the squared residual was required to be less

mass	carpet			
m	- cub	(1,4,2)	(2,4,2)	(16,4,2)
0.500	106	98	96	84
0.100	275	336	249	129
0.080	295	389	265	131
0.050	337	502	304	131
0.040	346	545	324	134
0.030	369	608	334	132
0.020	380	696	363	133
0.010	424	735	390	134
0.005	454	809	412	134
0.001	543	869	380	132

Table 4.2: Convergence of CG algorithm.

than 10^{-70}. Runs were also performed on regular cubic lattices both with periodic and antiperiodic boundaries and are denoted by *+ cub* and *- cub*. On average, 3 minutes of DAP time was required for a run at one mass value for all 3 sources on one carpet.

The resulting G were summed over final sites to give the following timeslice propagators:

$$\begin{aligned} M_{00}(t) &= \sum_x (M^{-1}b_0)_{(x,t)} \\ M_{\pi\pi}(t) &= \sum_x e^{i\pi x}(M^{-1}b_\pi)_{(x,t)} \\ M_{0\pi}(t) &= \sum_x e^{i\pi x}(M^{-1}b_0)_{(x,t)} \\ M_{\pi 0}(t) &= \sum_x (M^{-1}b_\pi)_{(x,t)} \end{aligned}$$

The (x,t) denote the position of the final sites. The propagator $M_{pp'}(t)$ represents the propagation of a momentum p state from the source to a momentum p' state at time t. In addition to these propagators, there was the site-to-site propagator $G(x,t) = (M^{-1}b_{pt})_{(x,t)}$.

4.3.5 Doubling

Following the work with naive fermions on random lattices [104], two tests were used to look for the absence of doubling. In the 2-dimensional random lattice work it is claimed that the random lattice dynamically induces the spontaneous breakdown of chiral symmetry [104]. The three doubled species acquire masses of $O(1/a)$, where a is the lattice spacing, and decouple from the model. Associated with the chiral SSB is the existence of a pseudo-Goldstone boson with mass $\approx \sqrt{m/a}$ and this also decouples leaving a model containing just a single species of fermion. Evidence for this claim comes from noticing an enhancement in the chiral condensate at small masses and from noticing the suppression of momentum π/a propagators. Does the same behaviour manifest itself on fractal carpets ?

mass	carpet				
m	− cub	+ cub	(1,4,2)	(2,4,2)	(16,4,2)
0.500	0.508	0.508	0.518	0.518	0.518
0.100	0.212	0.212	0.178	0.172	0.172
0.080	0.180	0.182	0.146	0.139	0.139
0.050	0.126	0.133	0.096	0.088	0.088
0.040	0.104	0.117	0.079	0.071	0.071
0.030	0.081	0.103	0.061	0.053	0.053
0.020	0.055	0.096	0.042	0.036	0.036
0.010	0.028	0.122	0.024	0.018	0.018
0.005	0.014	0.207	0.016	0.009	0.009
0.001	0.003	0.979	0.005	0.002	0.002

Table 4.3: Chiral Condensates.

Table 4.3 shows the chiral condensates $< \overline{\psi}\psi >$ found on some of the carpets. It is obtained by using the expression $< \overline{\psi}\psi >= G(32,0)$ where $(32,0)$ is the position of the source site. Notice the way in which the condensates on the fractals all decrease with decreasing m. This implies that the zero-mode which exists on the periodic regular cubic lattice is absent on the carpets. The condensates are shown in Figures 4.11, 4.12 and 4.13.

There appears to be no enhancement of the condensates on the carpets compared to the condensates on the regular cubic lattice. Furthermore, no enhancement was seen on any of the 36 fractal carpets.

If the non-zero momentum fermion species were to become heavier than the zero-momentum species then one would expect the $M_{\pi\pi}$ timeslice propagator to decay faster in time than the M_{00} propagator; the two propagators would not be identical. On all 36 fractal carpets at all m values and for all times t, we found that M_{00} and $M_{\pi\pi}$ agreed to 7 significant figures accuracy. The M_{00} and $M_{\pi 0}$ propagators for the (1,4,2) carpet with $m = 0.080$ are shown in Figures 4.14 and 4.15. The dashed line is that obtained for M_{00} at $m = 0.080$ on the regular cubic lattice with antiperiodic boundary conditions.

4.3.6 Conclusions

The study of Dirac-Kahler fermions on non-truncated fractals looks to be far more difficult than the study of bosons on such structures. The decimation procedure does not map the DK equation back into itself and hence cannot be used iteratively to study the fermions.

The behaviour of fermions observed on random lattices does not occur on truncated Sierpinski carpets; doubling still seems to occur on truncated fractals. Because of this, truncated fractals appear to be of no use as regulators in lattice gauge theory.

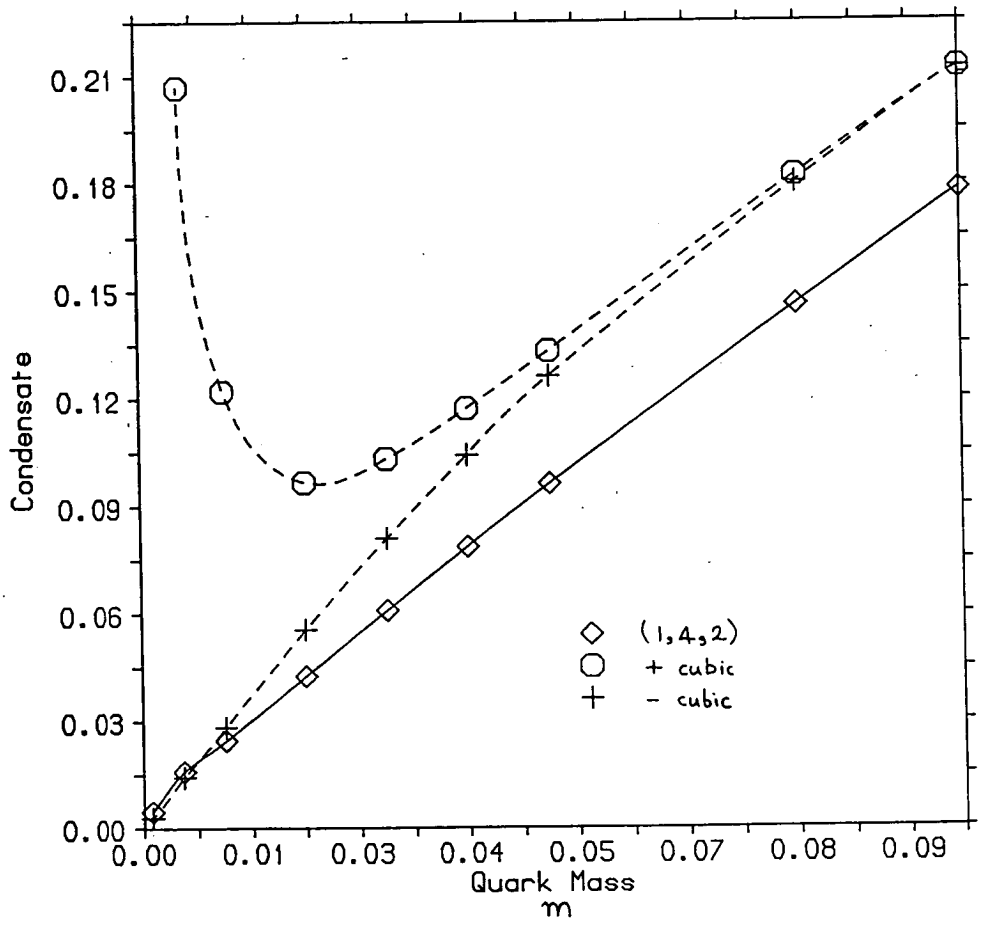

Figure 4.11: Chiral condensate on a (1,4,2) carpet and regular lattices.

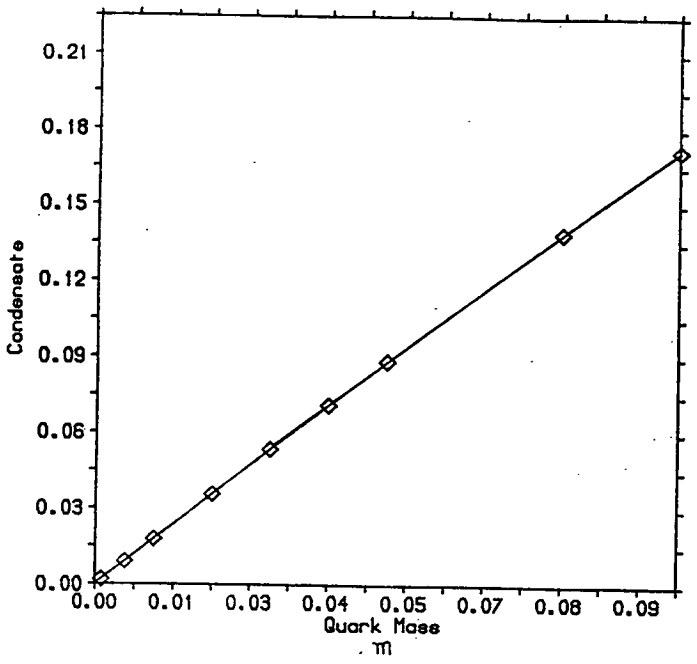

Figure 4.12: Chiral condensate on a (2,4,2) carpet.

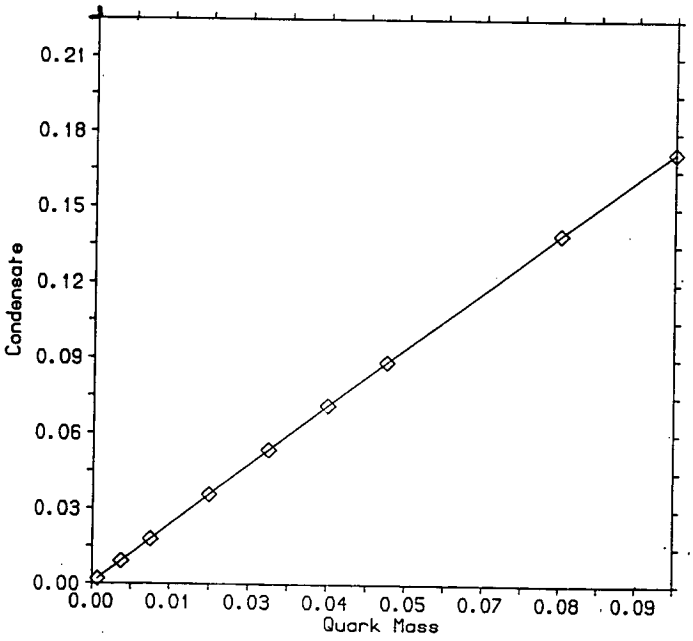

Figure 4.13: Chiral condensate on a (16,4,2) carpet.

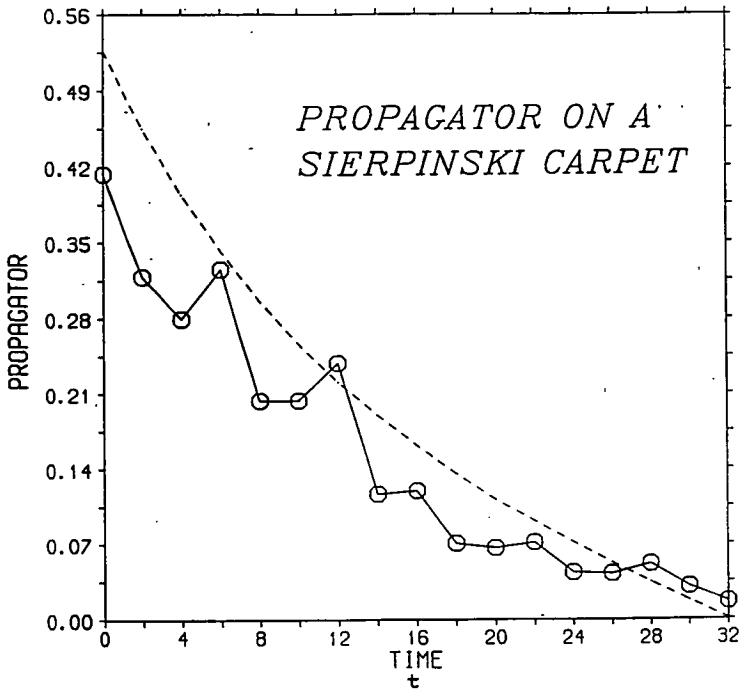

Figure 4.14: M_{00} propagator on a (2,4,2) carpet.

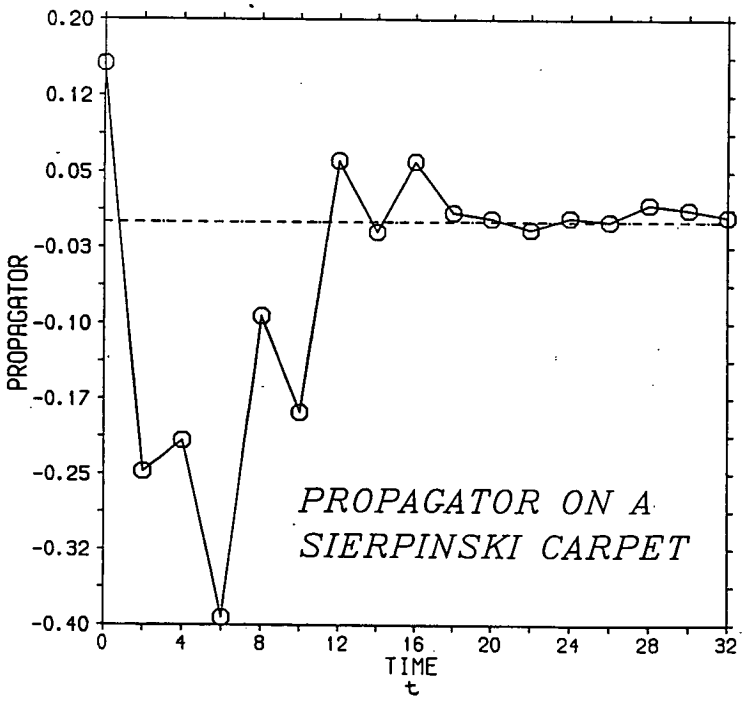

Figure 4.15: $M_{\pi 0}$ propagator on a (16,4,2) carpet.

Appendix A

Notation.

A.1 Indices

(a) Repeated indices are contracted.

(b) Unmentioned indices are often suppressed.

A.2 Lattice Derivatives

$$
\begin{aligned}
[D_\mu]_{xy} &= \frac{1}{2}\left(U_\mu(x)\delta_{y,x+\hat{\mu}} - U_\mu^{-1}(y)\delta_{y,x-\hat{\mu}}\right) \\
\left[D_\mu^2\right]_{xy} &= \frac{1}{4}\left(U_\mu(x)U_\mu(x+\hat{\mu})\delta_{y,x+2\hat{\mu}} + U_\mu^{-1}(x-\hat{\mu})U_{\hat{\mu}}^{-1}(y)\delta_{y,x-2\hat{\mu}} - 2\delta_{xy}\right) \\
D^2 &= \sum_{\mu=1}^{4} D_\mu^2
\end{aligned}
$$

The free fermion derivative ∂ is defined as D with all gauge links $U_\mu = 1$.

A.3 Gamma Matrices

The gamma matrices used in lattice simulations satisfy the anti-commutation relation $\{\gamma_\mu, \gamma_\nu\} = 2\delta_{\mu\nu}$ and are defined to be hermitian $\gamma_\mu = \gamma_\mu^\dagger$. The matrix γ_5 is defined as $\gamma_5 = \gamma_1\gamma_2\gamma_3\gamma_4$ and is also hermitian $\gamma_5 = \gamma_5^\dagger$.

A.4 Miscellaneous

Hermitian conjugation † is the product of the operations of complex conjugation $*$ and the transposition of indices. Unless otherwise stated, *all* indices are transposed including space-time ones.

The symbols x and y will frequently be used to label the space-time 4-tuples (x_1, x_2, x_3, x_4) and (y_1, y_2, y_3, y_4) and Greek indices will often be used to label the directions 1, 2, 3 and 4.

$| x |$ denotes the absolute value of x and $\| x \|^2$ denotes $x^\dagger x$.

Appendix B

Array Processors.

The test of a first-rate intelligence
is the ability to hold two opposite ideas
in mind at the same time and still retain
the ability to function.

F. Scott Fitzgerald

To perform numerical simulations of field theory systems one needs to use computers with *first-rate intelligence*. Conventional single processor systems are not fast enough to solve such computationally-intensive problems. In the development of multi-processor systems, two approaches have been taken. The first involves *pipelining* the problem and then using vector processors to solve the problem. The second approach relies on having an array of connected processing elements (PE) over which the problem can be distributed. Two types of array processor have been used at Edinburgh for solving field theory problems. In this appendix, I will briefly describe both types of computer.

B.1 Distributed Array Processor.

The I.C.L. Distributed Array Processor (ICL DAP) consists of a 64 $\times$ 64 array of bit-serial PEs each having 4096 bits of memory as shown in Figure A.1. Each PE performs the same task but on a seperate piece of data [1] where the data are bits in the 4096 bit planes. The machine

[1]Single Instruction Multiple Data (SIMD)

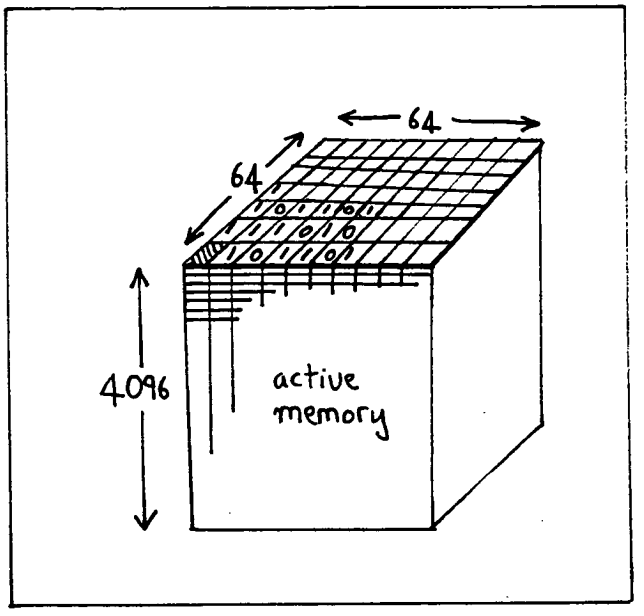

Figure B.1: ICL Distributed Array Processor.

acts like an active memory unit and is hosted by an ICL 2976 mainframe. Data is normally paged to and from the DAP by the use of COMMON blocks. However at Edinburgh, the ERCC [2] developed fast asynchronous paging software at the request of the physics department. Maximum data transfer rates of 250 Kbaud could be achieved. The DAP is programmed in a language known as DAP FORTRAN which has commands for operating on 64×64 arrays. Typical speeds for the DAP are around 20 Mflops.

B.2 Transputer Array.

With the advent of VLSI technology it became possible to put a whole computer on one integrated circuit; such an object is known as a *transputer* and the INMOS T800 floating-point transputer is shown in Figure A.2.

[2]Edinburgh Regional Computing Centre

The T800 has a 64 bit floating-point unit capable of 1.2 million floating-

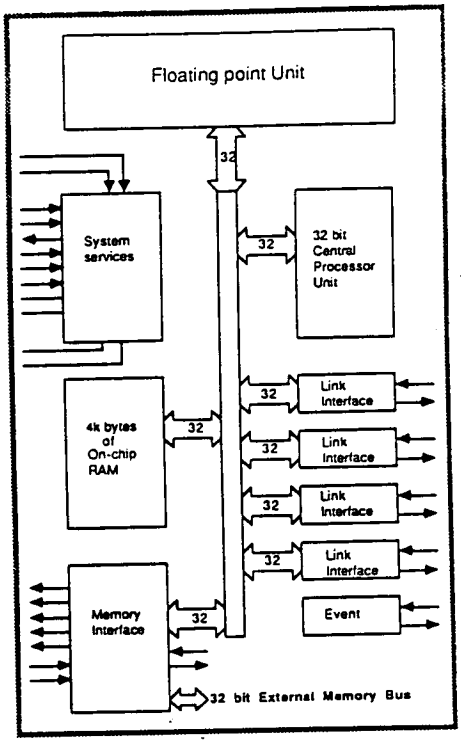

Figure B.2: The INMOS T800 transputer.

point multiplies per second. In addition, it has four hard links capable of transferring data at a rate of 20 Mbaud.

Taking a T800 and 4 Mbytes of memory makes the powerful PE used in the Meiko Computing Surface. Computing Surfaces are reconfigurable arrays of such PEs and are therefore flexible MIMD [3] array processors. Each PE in the surface performs its own instructions on its own data. The speed of just one PE is about 1.5 Mflop. The Edinburgh Concurrent Supercomputer is a Computing Surface which contains over 100 PEs connected in user domains. The largest domain, that was used in Chapter 3 of this thesis, contained 103 PEs. A concurrent program language called OCCAM2 is used to program the transputers.

[3]Multiple Instruction Multiple Data

Appendix C

Fermion Determinant.

C.1 Definitions.

Consider the action $S = S_b + S_f$ with S_b being a purely bosonic part and S_f having the form $\overline{\psi} M \psi$ with the fermion matrix M being, in general, a function of the boson fields. Integrating out the ψ and $\overline{\psi}$ in the path-integral, introduces the factor $\det M$ which is, in general, a non-linear non-local functional of the bosonic fields. This can be rewritten as an *effective* action S_{eff} defined by:

$$\det M = e^{-S_{eff}}$$

Applying the matrix identity $\ln\det A = \mathrm{Tr}\ln A$ allows one to write:

$$S_{eff} = -\mathrm{Tr}\ln M$$

The $\ln M$ can be expanded in a perturbation series in order to give explicit terms in the effective action.

In the next sections, we will apply this procedure to the action defined by:

$$\begin{aligned} S_b &= -2K \sum_{x,\mu} \cos(\theta_{x+\hat{\mu}} - \theta_x) \\ S_f &= \overline{\psi}^{(1)} M \psi^{(1)} + \overline{\psi}^{(2)} M^{\dagger} \psi^{(2)} \\ M &= \not{\partial} + m + Y \exp(i\theta\gamma_5) \end{aligned}$$

For $m = 0$, this is the action of the toy model discussed in Chapter 3. Note that M has been written symbolically; the derivative is a lattice derivative. In this 2-species model, the effective action $S^{(2)}_{eff}$ is the sum of S_{eff} and S^{*}_{eff} where $S_{eff} = -\ln\det M$.

C.2 Large Y

For the $m = 0$ case, an expansion of S_{eff} in powers of $1/Y$ can be obtained as follows:

$$\begin{aligned} S_{eff} &= -\mathrm{Trln}(\not{\phi} + Y e^{i\theta\gamma_5}) \\ &= -\mathrm{Trln}\left(Y e^{i\theta\gamma_5}\left(1 + \frac{e^{i\theta\gamma_5}}{Y}\not{\phi}\right)\right) \\ &= -\mathrm{Trln}Y - \mathrm{Trln}(1 + \frac{e^{i\theta\gamma_5}}{Y}\not{\phi}) \end{aligned} \tag{C.1}$$

The expansion $\ln(1+x) = x - x^2/2 + \ldots$ can now be applied and gives:

$$\begin{aligned} S^{(2)}_{eff} &= -8N \ln Y + \frac{2N}{Y^2} \\ &\quad -\frac{2}{Y^2}\sum_{x,\mu}\cos(\theta_{x+\hat{\mu}} - \theta_x) + O(1/Y^4) \end{aligned}$$

The first line in this expression is a constant and therefore has no effect on the boson dynamics. The second line is of the same form as the K term in S_b and, so to $O(1/Y^2)$, one can think of the fermions as causing the bosons to have an effective K equal to $K + 1/Y^2$.

C.3 Small Y

Denoting the free fermion matrix by $M_0 = \not{\phi} + m$, one obtains:

$$\begin{aligned} S_{eff} &= -\mathrm{Trln}(\not{\phi} + m + Y e^{i\theta\gamma_5}) \\ &= -\mathrm{Trln}M_0(1 + M_0^{-1} Y e^{i\theta\gamma_5}) \end{aligned}$$

The log can now be expanded in powers of Y which corresponds to the Feynman diagram expansion shown in Figure A.1. Summing 1- and 2-legged diagrams gives the expression:

$$\begin{aligned} S^{(2)}_{eff} &= -8mY I_1 \sum_x \cos\theta_x \\ &\quad +4Y^2 \sum_{x,y} 16m^2 I_2(x+y)\cos(\theta_x + \theta_y) \\ &\quad +4Y^2 \sum_{x,y} I_3(x-y)\cos(\theta_x - \theta_y) + O(Y^3) \end{aligned}$$

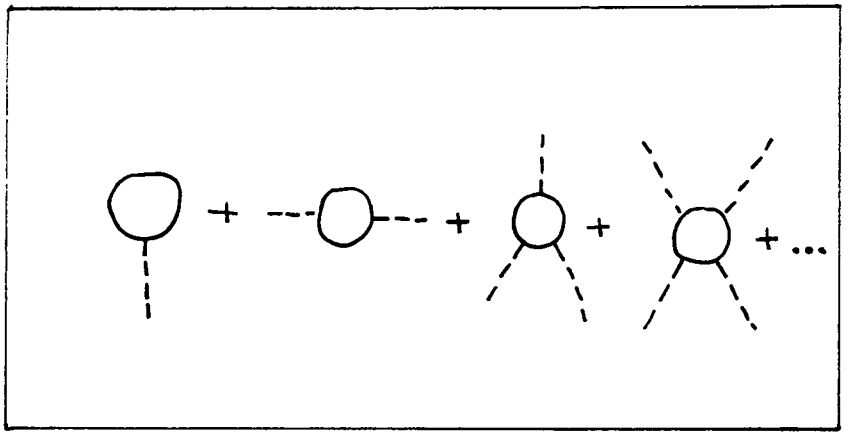

Figure C.1: Small Y expansion.

where the loop integrals I are defined as:

$$\begin{aligned} I_1 &= \frac{1}{N}\sum_p \frac{1}{T(p)} \\ I_2(z) &= \frac{1}{N^2}\sum_{p,q} \frac{\cos(q.z)}{T(p)T(p-q)} \\ I_3(z) &= \frac{1}{N^2}\sum_{p,q,\mu} \frac{\cos(q.z)\sin(p_\mu)\sin(p-q)_\mu}{T(p)T(p-q)} \\ T(p) &= m^2 + \sum_\mu \sin^2 p_\mu \end{aligned}$$

The integrals can be performed numerically and depend on the choice of boundary condition. With periodic boundary conditions I_1, I_2, I_3 diverge at $m = 0$.

The effect of S_{eff} on the observables has now to be calculated. It is convenient to consider the partition function

$$Z = \int d[\theta] \mathrm{e}^{-S_b - S^{(2)}_{eff}}$$

Once this is known, expectation values can then be obtained from it. For example,

$$< Q > \;=\; \frac{1}{2} + \frac{1}{16N}\frac{\partial \ln Z}{\partial K} \tag{C.2}$$

To find Z, one must perform summations over the angle variables θ. This is possible when either the angles are small or when the parameters in the action are small. In the small angle case one uses the fact that

$$e^{K\cos\theta} \;\approx\; e^{K}e^{-K\theta^2/2}$$

and then one can carry out the gaussian integrals in θ. For the small parameter case, the exponential is expanded as $e^{-S} = 1 - S + S^2/2! - S^3/3! + \ldots$ and then integrals are performed over the resulting products of sine and cosine functions. Upto $O(K^3)$ and $O(Y^3)$ terms, and omitting the KY^2 and K^2Y^2 terms, one obtains after expanding to S^3:

$$\begin{aligned}\frac{Z}{(2\pi)^N} \;=\;& 1 - 2Y^2 I_3(0) + 16Nm^2Y^2I_1^2 \\ & +128Nm^2KY^2I_1^2 - 2NKY^2\sum_{\mu} I_3(\hat{\mu}) \\ & +4NK^2\end{aligned}$$

For $K = 0$, this gives the expression:

$$< Q > \;=\; \frac{1}{2} + 8m^2Y^2I_1^2 + \frac{Y^2}{8}\sum_{\mu} I_3(\hat{\mu}) + O(Y^3)$$

As explained in Chapter 3, this expression is of use in checking the algorithm.

Bibliography

"I have been so seedy that I could not read anything however profound without going to sleep over it."

James Clerk Maxwell (1879)

[1] S.L Glashow, Rev. Mod. Phys. 52 (1980) 539.

[2] A. Salam, Rev. Mod. Phys. 52 (1980) 525.

[3] S. Weinberg, Rev. Mod. Phys. 52 (1980) 515.

[4] J.C. Maxwell, *A Dynamical theory of the electromagnetic field*, (Ed. T. Torrance, Scottish Academic Press, Edinburgh 1982).

[5] K.G. Wilson, Phys. Rev. D10 (1974) 2445.

[6] R.P. Feynman, Rev. Mod. Phys. 20 (1948) 367.

[7] M. Ninomiya, Phys. Rev. Lett. 53 (1984) 1611.

[8] L. Karsten and J. Smit, Nucl. Phys. B183 (1981) 108.

[9] L. Karsten and J. Smit, Phys. Lett. 104B (1981) 315.

[10] K.G. Wilson, *New phenomena in subnuclear physics*, (Ed. A. Zichichis, Plenum, New York 1977).

[11] L. Susskind, Phys. Rev. D16 (1977) 3031.

[12] H. Nielsen and M. Ninomiya, Nucl. Phys. B185 (1981) 20.

[13] H. Nielsen and M. Ninomiya, Nucl. Phys. B193 (1981) 173.

[14] H. Nielsen and M. Ninomiya, Nucl. Phys. B195 (1981) 541.

[15] D. Gross and F. Wilczek, Phys. Rev. Lett. 30 (1973) 1343.

[16] D. Gross, Phys. Rev. D8 (1973) 3633.

[17] S. Weinberg, Phys. Rev. D5 (1973) 1412.

[18] H. Fritsch, M. Gell-Mann and H. Leutwyler, Phys. Lett. 47B (1973) 365.

[19] H.D. Politzer, Phys. Rev. Lett. 30 (1973) 1346.

[20] H.D. Politzer, Phys. Rep. 14C (1973) 129.

[21] H. Hamber and G. Parisi, Phys. Rev. Lett. 47 (1981) 1792.

[22] K.C. Bowler, E. Marinari, G.S. Pawley, F. Rapuano, and D.J. Wallace, Nucl. Phys. B220 [FS8] (1983) 137.

[23] K.C. Bowler, R.D. Kenway, G.S. Pawley and D.J. Wallace, Phys. Lett. 145B (1984) 88.

[24] K.C. Bowler, D.L. Chalmers, A. Kenway, R.D. Kenway, G.S. Pawley and D.J. Wallace, Nucl. Phys. B240 [FS12] (1984) 213.

[25] K.C. Bowler, D.L. Chalmers, A. Kenway, R.D. Kenway, G.S. Pawley and D.J. Wallace, Phys. Lett. 162B (1985) 354.

[26] R.D. Kenway, Phys. Lett. 158B (1985) 327.

[27] C.B. Chalmers, R.D. Kenway and D. Roweth, J. Comp. Phys. 70 (1987) 500.

[28] K.C. Bowler, C.B. Chalmers, R.D. Kenway, G.S. Pawley and D. Roweth, Nucl. Phys. B284 (1987) 299.

[29] K.C. Bowler, C.B. Chalmers, R.D. Kenway, D. Roweth and D. Stephenson, Nucl. Phys. B296 (1988) 723.

[30] K.C. Bowler, R.D. Kenway, D. Roweth and D.B. Stephenson, Nucl. Phys. B301 (1988) 304.

[31] L. Susskind, Phys. Rev. D16 (1977) 3031.

[32] H. Kluberg-Stern, A. Morel, O. Napoly and B. Petersson, Nucl. Phys. B220 [FS8] (1983) 447.

[33] D.J. Daniel and T.D. Kieu, Phys. Lett. 175B (1986) 73.

[34] J. Gasser and H. Leutwyler, Phys. Rep. 87 (1982) 77.

[35] A. Hasenfratz and P. Hasenfratz, Phys. Lett. 93B (1980) 165.

[36] D. Barkai, K.J.M. Moriarty and C. Rebbi, Phys. Lett. 156B (1985) 385.

[37] K.C. Bowler, F. Gutbrod, P. Hasenfratz, U. Heller, F. Karsch, R.D. Kenway, I. Montvay, G.S. Pawley, J. Smit and D.J. Wallace, Phys. Lett. 163B (1985) 367.

[38] D. Roweth, Edinburgh PhD thesis 1987.

[39] N.A. Metropolis, M.N. Rosenbluth, A.H. Rosenbluth, E. Teller and J. Teller, J. Chem. Phys. 21 (1953) 1087.

[40] M. Creutz, Phys. Rev. Lett. 43 (1979) 553.

[41] M. Creutz, Phys. Rev. D21 (1980) 2308.

[42] S.L. Adler, Phys. Rev. D37 (1988) 458.

[43] N. Cabibbo and E. Marinari, Phys. Lett. 119B (1982) 387.

[44] M.R. Hestenes and E. Stiefel, J. Res. Nat. Bur. Standards 49 (1952) 409.

[45] M.F.L Golterman, Nucl. Phys. B273 (1986) 663.

[46] R. Gupta, G. Guralnik, G.W. Kilcup, A. Patel, S.R. Sharpe and T. Warnock, Los Alamos preprint LAUR-87-1545.

[47] A. Morel and J.P. Rodrigues, Nucl. Phys. B247 (1984) 44.

[48] M.Fukugita, S. Ohta, S. Oyanagi, A. Ukawa, Phys. Lett. 191B (1987) 164.

[49] I. Barbour, P. Gibbs, J.P. Gilchrist, H. Schneider, G. Schierholz and M. Teper, Phys. Lett. 136B (1984) 80.

[50] J. Kogut, M. Stone, H.W. Wyld, S.H. Shenker, J. Shigemitsu and D.K. Saclair, Nucl. Phys. B225 [FS9] (1983) 326.

[51] G. Martinelli and Z. Yi-Cheng, Phys. Lett. 123B (1983) 433.

[52] S.L. Glashow, Nucl. Phys 22 (1961) 579.

[53] A. Salam and J.C. Ward, Phys. Lett. 13 (1964) 168.

[54] S. Weinberg, Phys. Rev. Lett. 19 (1967) 1264.

[55] G. 't Hooft, Nucl. Phys. B33 (1971) 173.

[56] G. 't Hooft, Nucl. Phys. B35 (1971) 167.

[57] E. Fermi, Nuovo Cimento 11 (1934) 1.

[58] E. Fermi, Z. Phys. 88 (1934) 161.

[59] P. Hasenfratz and J. Nager, Z. Phys. C37 (1988) 477.

[60] A. Hasenfratz and T. Neuhaus, Nucl. Phys. B297 (1988) 205.

[61] A. Hasenfratz, K. Jansen, C.B. Lang, T. Neuhaus and H. Yoneyama, Florida preprint FSU-SCRI-87-52.

[62] J. Shigemitsu, Phys. Lett. 189B (1987) 164.

[63] J. Shigemitsu, OSU preprint DOE/ER/01545-397 Oct 1987.

[64] J. Shigemitsu and J. Polonyi, OSU preprint DOE/ER/01545-403 June 1988.

[65] A. Hasenfratz and T. Neuhaus, Florida preprint FSU-SCRI-88-55.

[66] S. Coleman and E. Weinberg, Phys. Rev. D7 (1973) 1888.

[67] R. Dashen and H. Neuberger, Phys. Rev. Lett. 50 (1983) 1897.

[68] D.J.E. Callaway, Rockefeller preprint RU/87/B1/20 Mar 1988.

[69] M. Kawamoto and J. Smit, Nucl. Phys. B192 (1981) 100.

[70] J. Smit, Acta. Phys. Polon. B17 (1986) 53.

[71] J. Smit, Amsterdam preprint ITFA-87-21.

[72] P.V.D. Swift, Phys. Lett. 145B (1984) 256.

[73] K.C. Bowler, G.S. Pawley, B.J. Pendleton, D.J. Wallace and G.W. Thomas, Phys. Lett. 104B (1981) 481.

[74] S. Duane, A.D. Kennedy, B.J. Pendleton and D. Roweth, Phys. Lett. 195B (1987) 216.

[75] Y. Oyanagi, Comp. Phys. Comm 42 (1986) 333.

[76] K. Jansen, J. Jersak, C.B. Lang, T. Neuhaus and G. Vones, Phys. Lett. 155B (1985) 268.

[77] A. Thornton, Edinburgh preprint 88/444, July 1988.

[78] S.W. Hawking, Nucl. Phys. B144 (1978) 349.

[79] T. Regge, Nuovo Cimento 19 (1961) 558.

[80] A. Jourjine, Wisconsin preprint MAD/TH/86-9.

[81] B.B. Mandelbrot, *Fractals: Form, Chance and Dimension* (Freeman, San Francisco 1977).

[82] B.B. Mandelbrot, *The Fractal Geometry of Nature* (Freeman, San Fransisco 1982).

[83] E. Domany, S. Alexander, D. Bensmon and L.P. Kadanoff, Phys. Rev. B28 (1981) 3110.

[84] G.E. Cooke and R. Finney, *Homology of Cell Complexes* (Princeton University Press, Princeton 1967).

[85] H.M. Flanders, *Differential forms* (Academic press, 1965).

[86] C.W. Misner, K.S. Thorne and J.A. Wheeler *Gravitation* (Freeman, 1973).

[87] C. von Westenholz, *Differential forms in mathematical physics* (North-Holland, 1981).

[88] I.M. Singer and J.A. Thorpe *Lecture notes on elementary topology and geometry* (Springer-Verlag, 1967).

[89] J.M. Rabin, Nucl. Phys. B201 (1982) 315.

[90] E. Kahler, Rendiconti di Matematica 21 (1962) 425.

[91] W. Graf, Ann. Inst. Henri Poincare A29 (1978) 85.

[92] F. Englert, J.M. Frere, M. Rooman and Ph. Spindel, Nucl. Phys. B280 [FS18] (1987) 147.

[93] M. Rooman, Phys. Lett. 169B (1986) 253.

[94] M. Rooman, Phys. Lett. 182B (1986) 358.

[95] C.G. Callan, Phys. Rev. D2 (1970) 1541.

[96] K. Symanzik, *Fundamental Interactions at high energies*, ed. A. Perlmutter, (Gordon and Breach, NY 1970).

[97] M. Feigenbaum, J. Stat. Phys. 19 (1978) 25.

[98] R. Orbach, Science 231 (1986) 814.

[99] H.M. Rosenberg, Phys. Rev. Lett. 54 (1985) 704.

[100] N.H. Christ, R. Friedberg and T.D. Lee, Nucl. Phys. B202 (1982) 89.

[101] N.H. Christ, R. Friedberg and T.D. Lee, Nucl. Phys. B210 [FS6] (1982) 310.

[102] N.H. Christ, R. Friedberg and T.D. Lee, Nucl. Phys. B210 [FS6] (1982) 337.

[103] D. Espriu, M. Gross, P.E.L. Rakow and J.F. Wheater, Nucl. Phys. B265 [FS15] (1986) 92.

[104] D. Espriu, M. Gross, P.E.L. Rakow and J.F. Wheater, Nucl. Phys. B275 (1986) 39.

[105] D. Espriu, M. Gross, P.E.L. Rakow and J.F. Wheater, Prog. Theor. Phys. 86 (1986) 304.

[106] S.J. Perantonis and J.F. Wheater, Nucl. Phys. B295 (1988) 443.

[107] Y. Pang and Hai-cang Ren, Phys. Lett. 195B (1987) 223.

[108] Y. Gefen, B.B. Mandelbrot and A. Aharony, Phys. Rev. Lett. 45 (1980) 855.

[109] Y. Gefen, Y. Meir, B.B. Mandelbrot and A. Aharony, Phys. Rev. Lett. 50 (1983) 145.

[110] G. Bhanot, H. Neuberger and J.A. Shapiro, Phys. Rev. Lett. 53 (1984) 2277.

[111] G. Bhanot, D. Duke and R. Salvador, Phys. Lett. B165 (1985) 355.

[112] G. Bhanot and R. Salvador, Florida preprint FSU-SCRI-85-9.

[113] J.C. LeGuillou and J. Zinn-Justin, Saclay preprint SPhT/86-092.